Long-range repulsive charged colloids in and out of equilibrium

Marjolein van der Linden

Long-range repulsive charged colloids Marjolein van der Linden 2013

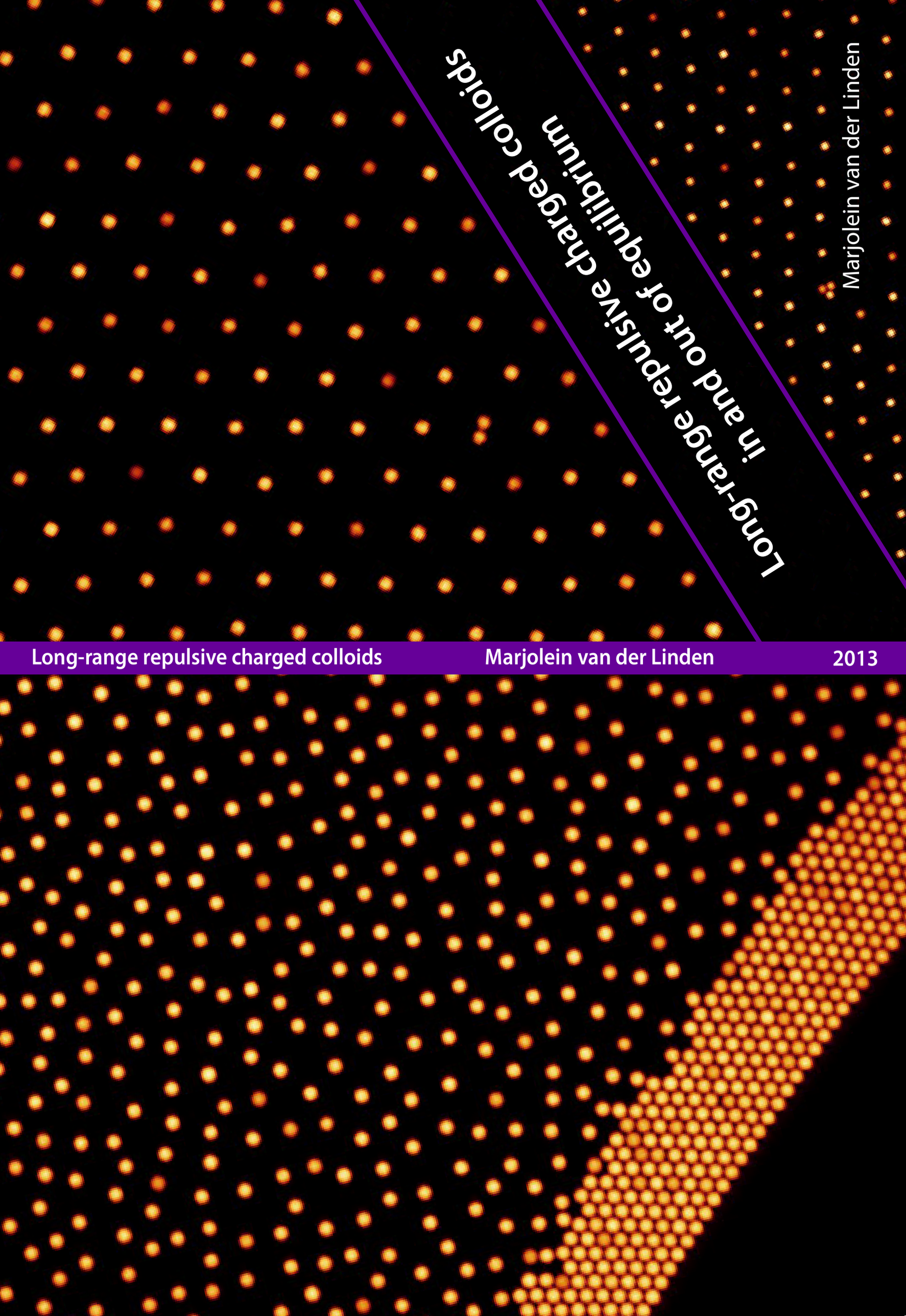

Long-range repulsive charged colloids in and out of equilibrium

Marjolein van der Linden

Cover: (front) Long-range colloidal crystal consisting of charged poly(methyl methacrylate) (PMMA) spheres suspended in cyclohexyl bromide (CHB). The diameter of the particles is 2.87 µm. (back) The same particles adsorbed to the wall of the glass capillary near the CHB-air interface.

Marjolein van der Linden
Long-range repulsive charged colloids in and out of equilibrium

PhD thesis, Utrecht University, the Netherlands, April 2013
A digital version of this thesis is available at http://www.colloid.nl.

Printed by: Proefschriftmaken.nl || Uitgeverij BOXPress, 's-Hertogenbosch

ISBN: 978-90-393-5935-8

Long-range repulsive charged colloids in and out of equilibrium

---

Geladen colloïden met repulsieve langedrachtsinteracties in en uit evenwicht

(met een samenvatting in het Nederlands)

Proefschrift

ter verkrijging van de graad van doctor aan de Universiteit Utrecht op gezag van de rector magnificus, prof. dr. G. J. van der Zwaan, ingevolge het besluit van het college voor promoties in het openbaar te verdedigen op maandag 22 april 2013 des ochtends te 10.30 uur door

Marjolein Neeltje van der Linden

geboren op 30 januari 1985 te Sliedrecht

Promotoren: Prof. dr. A. van Blaaderen
Prof. dr. ir. M. Dijkstra

This research was financially supported by the Netherlands Organisation for Scientific Research (NWO).

‘When I see equations, I see the letters
in colors – I don’t know why.
As I’m talking, I see vague pictures of
Bessel functions from Jahnke and Emde’s book,
with light-tan j’s, slightly violet-bluish n’s,
and dark brown x’s flying around.’

Richard P. Feynman
What do you care what other people think?
(1988)

Contents

1

General introduction

In this general introduction we explain what colloids are and what makes them interesting systems. We discuss the nature of the long-range repulsive interactions underlying the phase behaviour of the colloidal systems that are the main topic of this thesis. We also describe some of the phases that such long-range repulsive systems are able to form, either in equilibrium or out of equilibrium, which are a recurring aspect in each of the following chapters. We end this general introduction with an outline of the thesis.

1.1 Colloids

Colloidal dispersions [1–3] are heterogeneous systems that contain at least one component with dimensions in the range between a few nanometres and several micrometres. They consist of a disperse phase (solid particles, liquid droplets or gas bubbles) with dimensions in the colloidal size range and a dispersing medium (a solid, a liquid or a gas) which is considered as a continuum. An example is paint, which consists of solid particles (forming the disperse phase) dispersed in a liquid (the dispersing medium); other examples include fog (liquid in gas), smoke (solid in gas), foam (gas in liquid or solid) and milk (liquid in liquid). Depending on the context, the term 'colloid' either refers to the colloidal dispersion as a whole or to one of the dispersed particles (in this terminology the disperse phase is said to consist of 'colloids'). The colloidal dispersions (also called 'colloidal suspensions') that are the topic of this thesis consist of spherical solid particles dispersed (or 'suspended') in a molecular liquid (solvent).

Colloidal particles in a dispersion undergo Brownian motion. Due to thermal motion, the molecules in the solvent continuously collide with the colloidal particles. The resulting random motion of the colloids is called 'Brownian motion', after the botanist Robert Brown, who first observed this phenomenon in 1827 when studying a sample of plant pollen in water under a microscope [4]. Albert Einstein later provided a theoretical explanation for the Brownian motion [5], which was verified experimentally by Jean-Baptiste Perrin [6, 7].

When colloidal particles encounter each other, the combination of attractive and repulsive forces determines whether or not they aggregate. When no aggregation takes place, the dispersion is said to be (kinetically) stable. In many colloidal systems, Van der Waals interactions are responsible for attractions between the colloids. They arise from interactions between fluctuating dipoles in atoms. Van der Waals interactions can be reduced by dispersing the colloids in a solvent or solvent mixture with a refractive index that is close to that of the particles. Due to the small size of colloidal particles (compared to macroscopic objects), the surface-to-volume ratio is large and surface effects are important in colloidal systems. For solid particles dispersed in a liquid, the surface chemistry has a significant influence on the interparticle interactions. The colloids can be stabilised (against aggregation) by surface charge (charge stabilisation) or adsorbed polymers on the surface of the particles (steric stabilisation), which result in repulsions between the colloids.

Colloids are of interest from a fundamental point of view, because they can be used as model systems for atomic and molecular systems [8]. They can form crystalline, fluid and glassy phases, depending on, e.g. the volume fraction and interparticle interactions [9]. In case of charged colloids, for example, these inter-

actions are controlled by the ionic strength of the solvent [10]. Also, colloids have many industrial and technological applications, ranging from traditional examples as paint and toothpaste, to more advanced applications such as electrophoretic displays and photonic crystals.

Colloidal systems are relatively easy to investigate experimentally, due to their larger length and time scales compared to molecular systems. Experimental techniques to investigate colloidal systems include microscopy (electron microscopy, confocal microscopy), scattering techniques (static and dynamic light scattering) and electrophoresis. Confocal microscopy, the main experimental technique used in this thesis, makes it possible to study colloidal systems in three dimensions, in real-time and real-space and at a single-particle level [11]. In electrophoresis measurements the velocity of a particle in an electric field is measured from which the electrostatic surface potential and charge can be calculated [12]. In addition, a lot of insight can be gained from computer simulations [13] and theory [1], especially in combination with experiments.

1.2 Interactions

The pair interaction between uncharged colloidal particles is often described by a hard-sphere interaction potential. The hard-sphere potential is infinite for centre-to-centre distances smaller than the particle diameter and zero for all other distances.

Colloids in a suspension may acquire a net surface charge due to dissociation of surface groups or by adsorption of ions from the solvent onto the surface of the colloid. Charged colloids in a suspension are surrounded by an ionic atmosphere ('cloud') of co-ions and counterions around the colloidal particle. Close to the particle the concentration of counterions is high, due to strong electrostatic interactions between the ions and the charge on the particle surface. As a function of distance from the surface the cloud of counterions becomes more diffuse. A so-called electrical double layer is formed: the charge on the particle is the first layer; the other layer is the counterion-dominated cloud adjacent to the particle surface.

The ion concentrations as a function of the electrostatic potential are given by Boltzmann distributions. The Poisson equation relates the second spatial derivative of the electrostatic potential to the net charge density. Combined they yield the Poisson-Boltzmann (PB) equation, which can be solved with appropriate boundary conditions to yield an expression for the electrostatic potential as a function of distance from the particle surface. From this, an expression for the interaction potential resulting from the overlap of two double layers can be derived, which is repulsive for colloidal charges of the same sign.

Interactions between charged colloids are often described by the Derjaguin-Landau-Verwey-Overbeek (DLVO) theory [14, 15]. In this theory the interaction potential is written as a sum of the attractive Van der Waals potential energy and the repulsive free energy due to electrical-double-layer overlap. When the refractive index of the solvent closely matches that of the particles, as is the case in the experimental systems studied in this thesis, the Van der Waals interactions are much smaller than $k_{\mathrm{B}}T$ and can be neglected. For hard colloids an additional repulsive hard-sphere contribution results from interactions of the cores. The pair potential between two charged hard-core colloids i and j with diameters σ_i and σ_j and charge numbers Z_i and Z_j is then given by the hard-core screened Coulomb or Yukawa potential:

$$\beta u_{ij}(r) = \begin{cases} \beta\epsilon_{ij} \dfrac{\exp\left[-\kappa(r-\sigma_{ij})\right]}{r/\sigma_{ij}} & r \geq \sigma_{ij} \\ \\ \infty & r < \sigma_{ij} \end{cases} , \tag{1.1}$$

with $\sigma_{ij} = (\sigma_i + \sigma_j)/2$ and the contact value of the potential between two colloids i and j:

$$\beta\epsilon_{ij} = \frac{Z_i Z_j}{(1+\kappa\sigma_i/2)(1+\kappa\sigma_j/2)} \frac{\lambda_{\mathrm{B}}}{\sigma_{ij}} , \tag{1.2}$$

where r is the centre-to-centre distance between particles i and j, $\beta = 1/(k_{\mathrm{B}}T)$, with k_{B} the Boltzmann constant, and T the absolute temperature. The Bjerrum length is given by

$$\lambda_{\mathrm{B}} = \frac{e^2}{4\pi\epsilon_{\mathrm{r}}\epsilon_0 k_{\mathrm{B}}T} , \tag{1.3}$$

with e the elementary charge, ϵ_{r} the relative dielectric constant of the solvent and ϵ_0 the dielectric permittivity of vacuum. The Bjerrum length represents the distance at which the electrostatic interaction energy between two monovalent ions is equal to the thermal energy $k_{\mathrm{B}}T$. The inverse Debye screening length is given by

$$\kappa = \sqrt{8\pi\lambda_{\mathrm{B}} c_{\mathrm{s}}} , \tag{1.4}$$

with c_{s} the concentration of the monovalent salt. The Debye screening length κ^{-1} indicates the thickness of the electrical double layer surrounding a colloidal particle and is a measure for the interaction range between two colloids.

From Eq. 1.4 it is clear that the interaction range can be changed by adjusting the salt concentration: a high salt concentration corresponds to a small screening length, while a low salt concentration yields a large screening length. Eq. 1.4 is valid for the case of a monovalent electrolyte and follows from the more general expression $\kappa = \sqrt{4\pi\lambda_{\mathrm{B}} \sum c_i z_i^2}$ with the sum running over all ionic species i, the

concentrations of positive and negative ions ($c_+ = c_- = c_s$) and the square ionic charges ($z_+^2 = z_-^2 = 1$). For a monovalent salt the ionic strength I equals the salt concentration c_s ($I \equiv \frac{1}{2}\sum c_i z_i^2 = c_s$); note that the total concentration of monovalent ions is $2c_s$ and that non-dissociated ion pairs are not included in the salt concentration c_s.

The screened Coulomb part of the pair potential in Eq. 1.1 results from the solution of the linearised version of the PB equation, which is only valid for low electrostatic surface potentials ($\psi_0 < k_B T/e$) and limited double-layer overlap (small double layers and/or dilute systems). However, it was found a good approximation of the effective pair interaction in case of higher surface potentials provided the centre-to-centre distance is not too small. The corresponding effective surface potential, effective (or 'renormalised') charge and effective Debye screening length follow from matching the tail of the linearised PB solution to the full PB solution and extrapolating this to the surface of the particle [16, 17]. Because of its simplicity, Eq. 1.1 is also used to describe interactions in strongly interacting systems with high volume fractions and/or large double layers. However, it is doubtful whether the assumption of pairwise additivity is still valid in these systems, i.e. whether many-body interactions can be neglected.

In this thesis we used colloidal dispersions of micrometre-sized poly(methyl methacrylate) (PMMA) colloids dispersed in cyclohexyl bromide (CHB). The solvent slowly decomposes in time, a process which generates the ions H^+ and Br^-. Both ionic species are thought to adsorb on the colloidal particles, which, due to preferential adsorption of H^+ ions, acquire a net positive charge [18]. CHB is much less polar than water and can be purified before use, resulting in a much lower ionic strength (typically 0.1–1 nM) than would be possible in water. Due to the low ionic strength, the Debye screening length (Eq. 1.4) can become very large (several times the particle diameter), yielding long-range repulsive interactions, despite the relatively large size of the particles [19].

1.3 Crystals, fluids and glasses

Colloidal systems can form various phases [9]: crystals, in which the particles are ordered on a crystal lattice with a given symmetry; fluids, which have a disordered structure of diffusing particles; and glasses, which have a disordered structure like fluids, but diffusion is so slow that the structure barely changes on experimental timescales (this can be minutes, days, or even months) as is also the case for crystals. To form a glass, crystallisation needs to be avoided, which can be done by sufficiently fast compression, leaving no time for the particles to crystallise [11], or by using a polydisperse system [20].

For hard-sphere systems a fluid is stable below a volume fraction $\eta = 0.494$ and a face-centred-cubic (fcc) crystal is stable for $\eta > 0.545$ [9, 21]. Sufficiently fast compression of the fluid yields a glass for $\eta \gtrsim 0.58$ [22]. Phase diagrams for repulsive Yukawa particles have been calculated for a fixed contact value of the interaction potential [23–28] and recently also under conditions where the electrostatic potential at the particle surface was kept constant and conditions where the surface charge was regulated by an association-dissociation equilibrium of ions [29]. Phase diagrams have been obtained in experiments as well [10, 30]. Crystallisation takes place at a lower volume fraction than for hard spheres. A fluid is stable at low η, followed by an fcc crystal at higher η for small screening length $(\kappa\sigma)^{-1}$. For larger $(\kappa\sigma)^{-1}$ a region appears in the phase diagram in between the fluid and fcc regions, where a body-centred-cubic (bcc) crystal is stable. In the constant-potential and charge-regulation phase diagrams the regions where the crystals are stable are much smaller than in the fixed-contact-value phase diagrams. Furthermore, the constant-potential and charge-regulation phase diagrams show re-entrant melting at large $(\kappa\sigma)^{-1}$, i.e. a transition from crystal to fluid with increasing volume fraction. Fascinating phase behaviour was found in mixtures of particles with long-range interactions, for instance, the formation of binary crystals in mixtures of oppositely charged particles [31, 32]. Two other examples can be found in this thesis: the observation of the colloidal Brazil-nut effect [33] and the formation of strings consisting of alternating particles, both in binary mixtures of similarly charged particles.

1.4 Bond order parameters

An important tool for distinguishing different structures or phases are the so-called bond-orientational order parameters (or bond order parameters) [34, 35], which we will briefly discuss here. These parameters are based on the spherical harmonics and take different values depending on the spatial distribution of 'bonds' around a particle (here, a bond is a vector connecting the centres of the central particle and a neighbour). First, it is necessary to define a particle's neighbours. This can be done by a distance criterion (all particles within a certain distance are neighbours) or by using a Voronoi construction (a Voronoi cell contains all points in space closer to the particle contained in the cell than to any other particle; particles sharing a Voronoi face are neighbours). Next, for each particle i a set of $2l + 1$ bond order parameters can be defined:

$$q_{lm}(i) = \frac{1}{N_\mathrm{b}(i)} \sum_{j=1}^{N_\mathrm{b}(i)} Y_{lm}(\theta_{ij}, \phi_{ij}), \tag{1.5}$$

where $N_\mathrm{b}(i)$ is the number of neighbours of particle i, θ_{ij} and ϕ_{ij} are the inclination and azimuth angles of the bond $\mathbf{r}_{ij} = \mathbf{r}_i - \mathbf{r}_j$ (where $\mathbf{r}_i$ ($\mathbf{r}_j$) denotes the position of particle i (j)) connecting the centres of particle i and its neighbour j, and $Y_{lm}(\theta_{ij}, \phi_{ij})$ are the spherical harmonics (with $m = -l, -l+1, \ldots, l-1, l$). The sum runs over all neighbours of particle i. They can be combined to yield rotational invariants, which are independent of the choice of coordinate system, such as

$$q_l(i) = \sqrt{\frac{4\pi}{2l+1} \sum_{m=-l}^{l} |q_{lm}(i)|^2} \,. \tag{1.6}$$

These rotational invariants, which are also called bond order parameters, take a different value depending on the local spatial arrangement of bonds. For example, a particle in an ideal fcc environment has $q_6 \approx 0.57$, while a particle in an ideal bcc environment has $q_6 \approx 0.51$. In practice, Brownian motion of the particles causes deviation from these ideal values, such that particles in an fcc crystal would have q_6 values distributed around 0.57. The bond order parameters are an indication for the symmetry of the local environment of the particles.

A second important use for the bond-orientational order parameters is to discretely distinguish between crystalline and non-crystalline particles, regardless of the crystal symmetry [36]. This can be done by using the correlation between the sets of bond-orientational order parameters for each pair of neighbouring particles, given by

$$c_l(ij) = \frac{\sum_{m=-l}^{l} q_{lm}(i) q_{lm}^*(j)}{\left(\sum_{m=-l}^{l} |q_{lm}(i)|^2 \right)^{1/2} \left(\sum_{m=-l}^{l} |q_{lm}(j)|^2 \right)^{1/2}} \,, \tag{1.7}$$

where $q_{lm}^*(j)$ is the complex conjugate of $q_{lm}(j)$, and $q_{lm}(i)$ and $q_{lm}(j)$ are defined in Eq. 1.5. A neighbour j to particle i is defined as a connected neighbour, if $c_l(ij)$ exceeds a threshold value c_c. Particles with more than a certain number n_c of connected neighbours are defined as crystalline particles [36].

1.5 Scope of this thesis

In this thesis we describe our investigations of the properties and behaviour of long-range repulsive colloidal systems, using experiments and computer simulations. In **Chapter 2** we describe electrophoresis measurements performed on suspensions containing one of a variety of particle species, some of which were used in subsequent chapters. From the measured electrophoretic mobilities we obtained a

surface potential and surface charge for each of the particle species. We studied the dependence of the surface potential and charge on the diameter of the particles. We also discuss the formation of intriguing alternating strings in a binary mixture, for which from electrophoresis measurements both species were found to be positively charged. In **Chapter 3** we used computer simulations to study the effect of polydispersity on the crystal-fluid and crystal-glass transition in hard-core repulsive Yukawa systems. In **Chapter 4** we investigated the slow dynamics in these systems and a possible relation between the fragility and the range of the potential, again with computer simulations. In **Chapter 5** we studied the long-range repulsive glasses that were formed in experiments by means of centrifugation and were found to expand and crystallise after 2–3 months. In **Chapter 6** we report on the so-called colloidal Brazil-nut effect, i.e. the phenomenon that heavier particles stay further from the wall onto which the particles sedimented than lighter particles, which we observed experimentally in a binary mixture for certain parameter combinations. We analysed the sedimentation profiles and compared our results with predictions from theory and simulations.

2

Electrophoresis of PMMA colloids in cyclohexyl bromide: particle size dependence and particle mixtures

We studied suspensions of sterically stabilised poly(methyl methacrylate) (PMMA) particles in the solvent cyclohexyl bromide (CHB; $\epsilon_r = 7.92$). We performed microelectrophoresis measurements, using confocal microscopy to measure the velocity profiles of the particles. For differently sized particles we obtained the surface potential and charge from the electrophoretic mobility of the particles. We found that the surface potential was roughly constant for all particle diameters we investigated (1.9 µm $< \sigma <$ 4.4 µm), and that the particle charge was proportional to the square of the diameter. In addition, we report the observation of spontaneous formation of alternating strings in a binary suspension of two charged particle species, with charges of the same sign, but different magnitude, and discuss a possible mechanism of formation.

2.1 Introduction

Suspensions of charged colloids are widely used as model systems to study the phase behaviour of atomic and molecular systems [1]. They are also of interest for many technological and industrial applications (see, e.g. Refs. [37] and [38] for reviews of older work on suspensions in nonaqueous media). More recently, interest in interactions between charged particles in low- and apolar solvents and the origins of their charges has been rekindled because of new model studies exploring very long-range and soft potentials [19, 31, 32, 39–41] as well as applications in several areas of advanced materials, such as electrophoretic displays [42], toner for printing and copying [43] and electrorheological fluids [44]. Unfortunately, the charging mechanisms are still quite unclear, despite an increasing number of efforts to understand these mechanisms [18, 43, 45–65], and may differ for different particle systems. For a recent review on the charging mechanisms involving charge control agents see Ref. [66].

In this work, we used electrophoresis measurements to investigate the surface potential and charge in systems of sterically stabilised charged colloids (poly(methyl methacrylate); PMMA) in a low-polar solvent (cyclohexyl bromide; CHB). Below we discuss in more detail the significance of low-polar (relative dielectric constant $5 < \epsilon_r < 10$) versus apolar ($\epsilon_r \approx 2$) solvents in these systems. We determined the surface potential and charge as a function of the particle diameter. The measurements were inspired by our efforts to achieve the so-called colloidal Brazil-nut effect [33] for our model systems (Chapter 6). For these experiments we needed to make mixtures of colloids with charges of the same sign, but different magnitude. In one of such mixtures of unequally charged PMMA particles we observed intriguing flexible string formation, with the two different particles alternating in the strings despite the fact that both particles had net charges of the same sign. The electrophoresis measurements were also motivated by the fact that in a previous paper of our group on the electrophoresis in similar systems as a function of volume fraction [46] the effect of the particle size was not investigated.

The pair interaction in a system of charged colloidal particles is commonly described by a hard-core repulsive Yukawa (screened Coulomb) potential [15, 16, 31, 39]:

$$\beta u_{ij}(r) = \begin{cases} \beta\epsilon_{ij} \dfrac{\exp\left[-\kappa(r-\sigma_{ij})\right]}{r/\sigma_{ij}} & r \geq \sigma_{ij} \\ \infty & r < \sigma_{ij} \end{cases}, \tag{2.1}$$

with $\sigma_{ij} = (\sigma_i + \sigma_j)/2$ and the contact value of the potential between two colloids i and j:

$$\beta\epsilon_{ij} = \frac{Z_i Z_j}{(1+\kappa\sigma_i/2)(1+\kappa\sigma_j/2)} \frac{\lambda_B}{\sigma_{ij}}, \tag{2.2}$$

where r is the centre-to-centre distance between particles i and j, Z_i (Z_j) and σ_i (σ_j) are the charge number and diameter of colloid i (j), $\beta = 1/(k_B T)$, with k_B the Boltzmann constant, and T the absolute temperature. The Bjerrum length is given by

$$\lambda_B = \frac{e^2}{4\pi\epsilon_r\epsilon_0 k_B T}, \tag{2.3}$$

with e the elementary charge, ϵ_r the relative dielectric constant of the solvent and ϵ_0 the dielectric permittivity of vacuum. The Bjerrum length represents the distance at which the electrostatic interaction energy between two monovalent ions is equal to the thermal energy $k_B T$. The inverse Debye screening length is given by

$$\kappa = \sqrt{8\pi\lambda_B c_s}, \tag{2.4}$$

with c_s the concentration of the monovalent salt. The Debye screening length κ^{-1} indicates the thickness of the electrical double layer surrounding a colloidal particle and is a measure for the interaction range between two colloids. When the refractive index of the solvent closely matches that of the particles, as is the case in our experimental system, the Van der Waals interactions are much smaller than $k_B T$ and can be neglected.

It is easy to understand the reason why in solvents with a relative dielectric constant ϵ_r close to 2 (apolar solvents), such as alkanes, screening of electrostatic interactions is usually negligible and the creation of ions is energetically very unfavourable. If we consider the dissociation of a monovalent salt:

$$AB \rightleftarrows A^+ + B^-, \tag{2.5}$$

then the law of mass action applied to this equilibrium yields the following expression for the dissociation constant:

$$K_D \approx \frac{[A^+][B^-]}{[AB]} = \frac{(\alpha c_0)^2}{(1-\alpha)c_0}, \tag{2.6}$$

with K_D the dissociation constant, α the degree of dissociation, $[A^+]$ and $[B^-]$ the concentrations of free ions (A^+ and B^-), [AB] the concentration of undissociated ion pairs (AB) and c_0 the total concentration of electrolyte ($c_0 = [A^+] + [AB]$). For simplicity we took the ionic activity coefficients to be close to 1, which is a reasonable approximation for low concentrations of free ions. The dissociation

constant may be approximated by [37, 67]

$$K_{\mathrm{D}} = \frac{3}{4\pi a^3}\ \exp\left(-\frac{\lambda_{\mathrm{B}}}{a}\right), \tag{2.7}$$

with a the centre-to-centre distance of the dissociating ion pair and λ_{B} the Bjerrum length (Eq. 2.3). For small K_{D} ($\alpha \ll 1$), combining Eqs. 2.6 and 2.7 yields for the concentration of free ions

$$[\mathrm{A}^+] + [\mathrm{B}^-] = 2\alpha c_0 \approx \sqrt{\frac{3c_0}{\pi a^3}}\ \exp\left(-\frac{\lambda_{\mathrm{B}}}{2a}\right), \tag{2.8}$$

where we used $[\mathrm{A}^+] = [\mathrm{B}^-] = \alpha c_0$ and $[\mathrm{AB}] = (1-\alpha)c_0 \approx c_0$. The derivation of Eq. 2.7 for the dissociation constant was given by Fuoss [67] and was used later by Van der Hoeven and Lyklema [37]. Roberts et al. [45] used an expression similar to Eq. 2.8 for the concentration of free ions; we note, however, that the prefactor in Ref. [45] differs by a factor $\sqrt{8}$ from the prefactor in Eq. 2.8, because the ionic radius instead of the ion pair centre-to-centre distance was used. For a solvent such as dodecane with $\epsilon_{\mathrm{r}} = 2$ the Bjerrum length λ_{B} is 28.3 nm at $T = 295$ K, compared to $\epsilon_{\mathrm{r}} = 80$ and $\lambda_{\mathrm{B}} = 0.7$ nm for water. For typical salts which easily dissociate in water, such as NaCl which has an ion pair centre-to-centre distance $a \approx 0.28$ nm [68], the concentration of free ions in dodecane would be $\sim 10^{-22}$ mol L^{-1} for $c_0 = 0.01$ mol L^{-1} (from Eq. 2.8). This means that so-called charge control agents are needed to arrive at sufficiently high ion concentrations to start modifying interparticle interactions. Usually, these charge control agents consist of a sizeable alkyl chain and a more polar section to provide binding sites to the ions. This configuration makes these compounds in almost all cases (strongly) surface-active and the particle interactions strongly sensitive to (trace amounts of) water [66]. For solvents with a relative dielectric constant $5 < \epsilon_{\mathrm{r}} < 10$ (low-polar solvents), of which the solvent we use (cyclohexyl bromide; $\epsilon_{\mathrm{r}} = 7.92$ at $T = 298$ K [18, 19, 46, 69]) is an example, the dissociation of somewhat larger ions which are not yet surfactants, like tetrabutylammonium bromide (TBAB), is already appreciably larger. For this case with an ion pair centre-to-centre distance of roughly $a \approx 0.55$ nm [70] and $\lambda_{\mathrm{B}} = 7.1$ nm, Eq. 2.8 yields for the total concentration of free ions $\sim 5\times10^{-4}$ mol L^{-1} for $c_0 = 0.01$ mol L^{-1}. The double layers can still be quite large in these low-polar solvent systems ($\sim$ tens of microns) or made quite small by addition of salts like TBAB [19, 31, 39, 46]. In addition, the charge and double-layer thickness in these model systems are not very sensitive to water; water can even be used as ion exchange agent to remove salt. In short, the use of low-polar solvents (with $5 < \epsilon_{\mathrm{r}} < 10$) rather than apolar solvents (with $\epsilon_{\mathrm{r}} \approx 2$) retains many of the desirable properties of apolar solvents (immiscibility with water, low

conductivities, very large double layers), while ions are more easily created without surfactants and the system is less sensitive to small amounts of water.

Motivated by the recently increased interest in charged particles in low- and apolar solvents there have been improvements on microelectrophoresis techniques compared to the more conventional electrophoresis techniques like phase analysis light scattering [71] and electroacoustic phoresis [64] that were commonly used to study these systems, which are usually characterised by a very small amount of charges and thus low mobilities compared to particles in polar solvents like water. Almost all techniques literally focus in on measurements of single-particle motions [46, 48, 49, 57, 72]. Several make use of optical tweezers to confine the particle motions when the particles are driven by an electric field [45, 48, 52, 57]. In the (re)new(ed) techniques position determination at the single-particle level is done either using a photoquadrant detection scheme or by image processing. Our approach makes use of confocal microscopy, which also allows measurements on individual particles in more concentrated, even crystallised, systems [46]. Of course, for more concentrated systems it is harder to convert a measured mobility to a surface charge or potential than for dilute systems. The approach taken in this chapter is the same as in earlier work by our group, in which a cell model was used to obtain these quantities [46]. For completeness it should be mentioned that improvements have been made on other techniques as well, for instance, on the light scattering approach. An example is the use of laser Doppler velocimetry by the Palberg group, which also allows measurements at higher volume fractions, but for polar systems in which large relative screening lengths $(\kappa\sigma)^{-1}$ were achieved by using small particles [73–75].

Despite significant progress, a lot is still unknown about the exact charging mechanisms, which is reflected in different approaches to explain them. There are groups trying to relate the particle charge to the acid/base properties of the particles and thus relate the charging mechanism to behaviour in water (see e.g. Refs. [60, 61, 63, 76] and references cited therein), while others look at hydrophilic/hydrophobic effects (see Ref. [59] and references cited therein). It is quite clear that most of the surfactant-like charge control agents enlarge the effective size of ions by micelle formation and thus enhance dissociation of ion pairs. However, details on how this enhanced ion pair dissociation in solution exactly charges the particles are less clear [45, 49, 53, 54, 58, 62, 66] and it is important to mention that surfactants with non-ionisable groups are just as effective in increasing conductivity and charging the particles in low-polar solvents as are ionic surfactants [58, 59, 62]. It was already mentioned as well that all systems with charge control agents are sensitive to trace amounts of water [59, 63, 66], while the screening length of our PMMA particles in CHB is not sensitive to water; these suspensions can even be deionised effectively with water [18, 40, 77].

Only in the case of strongly dissociating salts or acids/bases in water one expects a constant surface charge density. In all other cases where some kind of association-dissociation equilibrium is operative at the surface of the particles one expects a more complex boundary condition for the surface potential of the particles as function of size, volume fraction and ionic strength. The simplest models developed still predict over a large parameter space a particle charge which scales with the particle surface area [2]. For several systems with added surfactant-like charge control agents it was found that the surface potential was independent of particle size [45, 56]. This required some more complicated charge regulation mechanisms [45, 53, 56]. As mentioned, in our sterically stabilised PMMA system in CHB no charge control agents are used and it is therefore interesting to find out if the dependence of the surface potential on particle size is different than the examples from Refs. [45, 53, 56]. The hypothesis for the origin of the positive charge in the PMMA system in 'pure' CHB is that decomposition of CHB generates HBr and that apparently more protons adsorb onto/in the particles than bromide ions (see chapter 2 of Ref. [18]). When a salt with large ions such as TBAB is added to a solvent like CHB, significant dissociation takes place and the conductivity increases appreciably. In addition the sign of the particle charge changes from plus to minus, which is thought to be due to an increased adsorption of bromide ions [19, 31]. In the course of our investigation, we also noticed that so-called 'locked' particles had a significantly higher particle charge than those for which the locking procedure, which chemically links the PHSA-g-PMMA-stabiliser chains to other PMMA chains in the particle, was not performed. We speculate about a possible reason for the difference.

For particles with a high charge the interactions between two particles at some distance from each other can still be described by the Yukawa potential, but with the bare charge in Eq. 2.1 replaced by a (smaller) renormalised charge [10, 16]. At low bare charge the renormalised charge is equal to the bare charge, but as the bare charge increases the renormalised charge increases less and eventually, in the saturated charge regime, levels off to a plateau value. The saturated charge number Z_{sat} is proportional to the particle diameter. The relation proposed by Alexander et al. was $Z_{\mathrm{sat}} = A\sigma/\lambda_{\mathrm{B}}$ (with σ the particle diameter, λ_{B} the Bjerrum length and A a proportionality constant) [16]. In experiments [10, 78], simulations [79] and theoretical approaches without [16, 80] or including [81, 82] charge regulation, the proportionality constant A was found to depend on the volume fraction η and the salt concentration c_{s}, but in general to be of order $A \approx 5$.

This chapter is organised as follows. In Section 2.2 we provide details on the model system and describe the electrophoresis measurements. In Section 2.3 we give and discuss the results: the system parameters (Debye screening length, surface potential and charge) that we obtained, the shape of the mobility profiles,

the electrophoresis measurements in the binary mixture, the size dependence of the surface potential and charge and the observation of alternating strings. In Section 2.4 we present the conclusions.

2.2 Experimental methods

2.2.1 Model system

We used poly(methyl methacrylate) spheres (PMMA; density $d_{\mathrm{PMMA}} = 1.19$ g cm^{-3}; dielectric constant $\epsilon_{\mathrm{r}} = 2.6$; refractive index $n_{\mathrm{D}}^{25} = 1.492$ [18]), synthesised by dispersion polymerisation and sterically stabilised by a so-called comb-graft steric stabilising layer formed by poly(12-hydroxystearic acid) (PHSA) grafted onto a backbone of PMMA (PHSA-*g*-PMMA) [83, 84]. We used several batches of particles, of different mean diameter σ and labelled with either the fluorescent dye rhodamine isothiocyanate (RITC) or the fluorescent dye 7-nitrobenzo-2-oxa-1,3-diazol (NBD). The mean diameters and polydispersities s were determined by static light scattering (SLS) or scanning electron microscopy (SEM). To determine the average diameter and size polydispersity from the SEM images we measured ~ 100 particles from each batch using the program iTEM (Olympus Soft Imaging Solutions GmbH). Some batches of particles underwent a so-called 'locking' procedure [85], in which the PHSA-*g*-PMMA stabiliser became covalently bonded to the particle surface; in the remainder of this chapter, these particles are referred to as 'locked'. In the case of 'unlocked' particles, the PHSA-*g*-PMMA stabiliser is adsorbed to the particle surface, but not covalently bonded to it. The locking procedure was as follows [83]. The particles were transferred to dodecane (~ 1.3 g / g PMMA) saturated with PHSA-*g*-PMMA stabiliser. A small amount (~ 4.2 µL / g PMMA) of 2-dimethylaminoethanol (DMAE) was added as a catalyst and the mixture was stirred for two hours at 130°C. Finally, the particles were washed 3× with hexane.

The particles were suspended in cyclohexyl bromide (CHB; Sigma-Aldrich; density $d_{\mathrm{CHB}} = 1.336$ g cm^{-3} [18]; dielectric constant $\epsilon_{\mathrm{r}} = 7.92$ [69]; refractive index $n_{\mathrm{D}}^{25} = 1.4935$ [18, 69]), which nearly matched the refractive index of the PMMA particles ($n_{\mathrm{D}}^{25} = 1.492$). This solvent is known to decompose in time, a process which generates H^+ and Br^- ions (see Ref. [86] and chapter 2 of Ref. [18]). However, it is good to remark here that a similar decomposition of water into H^+ and OH^- is not generally considered a 'decomposition'. It is at this point unknown whether the reaction of CHB is as reversible as it is for water. To reduce the ionic strength, we cleaned the solvent before use [87], by bringing it into contact first with activated alumina ($\mathrm{Al_2O_3}$; 58 Å, ~ 150 mesh, Sigma-Aldrich) and then with molecular sieves (4 Å, 10–18 mesh, Acros Organics). The conductivity of

CHB after the cleaning steps was on the order of 10 pS cm^{-1} (Scientifica 627 conductivity meter).

2.2.2 Electrophoresis measurements

To measure the electrophoretic mobility of the particles in real space, we constructed electrophoresis sample cells in the following way (see also Ref. [46]). A borosilicate glass capillary with inner dimensions length × width × depth = 5 cm × 2.0 mm × 0.10 mm ($x \times y \times z$; VitroCom) was mounted on a microscope glass slide with two thin strips of adhesive tape (Scotch). Two nickel alloy wires (T2 thermocouple alloy wire, Goodfellow; diameter = 0.05 mm) served as electrodes. The wires were bent in a rectangular U-shape and inserted into the capillary (one at each end) in such a way that the wires were typically $\sim$ 1.5 cm apart (Figs. 2.1a and b). We stuck the wires to the glass slide with adhesive tape. In some cases we used two straight wires parallel to the capillary wall, $\sim$ 2.0 mm apart (Figs. 2.1c and d).

We prepared suspensions with an overall volume fraction $\bar{\eta} \approx 0.02$. Each suspension was transferred to a separate electrophoresis cell using a glass Pasteur pipette. We checked that no air bubbles were present between the two electrodes. Both ends of the capillary were sealed with UV-curing optical adhesive (Norland no. 68). We prevented air bubbles at both ends of the capillary by tilting the capillary before applying the glue, such that any air was pushed out by the dispersion inside; the extra volume occupied by the glue also expelled the air from the other side of the capillary.

For each sample we obtained the particle mobility in the following way. We applied a DC electric field and measured the mean particle velocity as a function of depth (total depth = 0.10 mm) in the capillary. The velocities were converted to mobilities (Eq. 2.9, below) and from a fit to the mobility profile we obtained the mean particle mobility (the mean apparent particle mobility at the stationary level). We used a wideband amplifier (Krohn-Hite, Model 7602M) to apply DC fields of 2–8 V mm^{-1}, in both directions. Typically, we measured two mobility profiles for the same sample, using two different field strengths, to check whether the measured mobility was independent of the field strength.

Fig. 2.1 shows the four different set-ups that we used for measuring electrophoretic mobilities. In most cases the capillary was placed vertically (long axis parallel to the direction of gravity; Figs. 2.1a and c), to prevent a density gradient across the 0.10 mm depth due to sedimentation of the particles. In a few cases the capillary was placed horizontally (Figs. 2.1b and d). On the timescale of the experiment, we observed significant sedimentation only for one sample in the horizontal set-up (the mixture, sample 5), as indicated in Section 2.3.

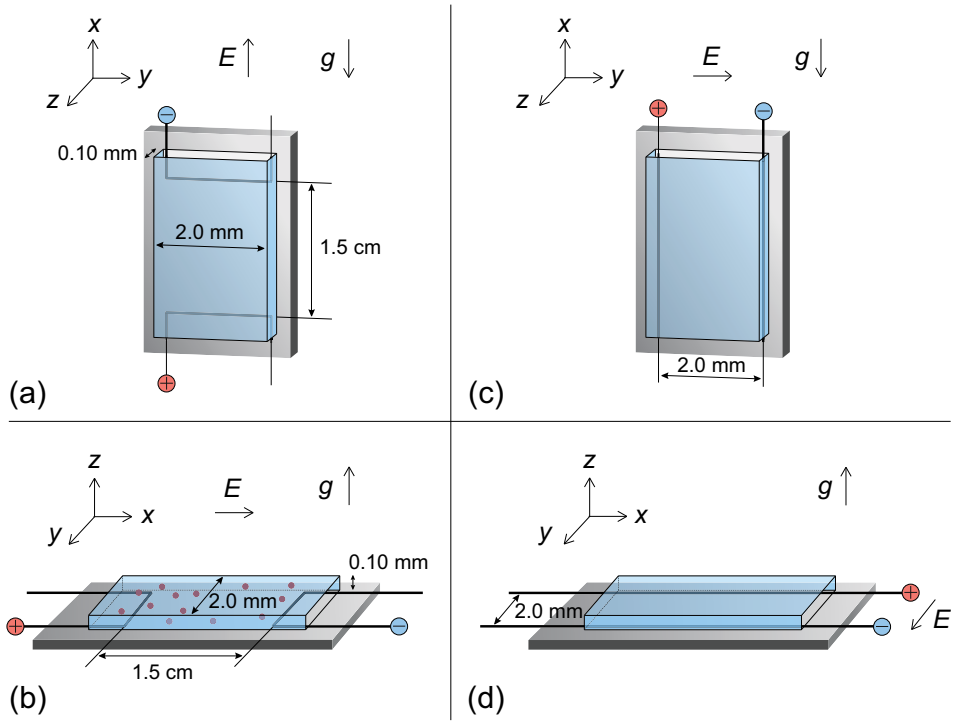

Figure 2.1: Schematic drawings of the four different set-ups used for measuring electrophoretic mobilities. In each case we indicate the direction of the electric field (E), the direction of gravity (g) and the three spatial dimensions x, y and z, chosen along the length (x), width (y) and depth (z) of the capillary. Note that we also applied the field in the opposite direction, with the + and − electrodes reversed. (a) Vertical capillary with U-shaped electrodes. (b) Horizontal capillary with U-shaped electrodes. (c) Vertical capillary with straight electrodes. (d) Horizontal capillary with straight electrodes. We indicated in each case the typical distance between the electrodes: 1.5 cm for (a) and (b) and 2.0 mm for (c) and (d). The depth (0.10 mm) and width (2.0 mm) of the capillary as indicated in (a) and (b) are the same in (c) and (d), respectively. In (b) we schematically show the particles; for clarity they have been left out for (a), (c) and (d).

The field direction was parallel to the direction of gravity in most cases (set-up with vertical capillary and U-shaped electrodes; Fig. 2.1a). We corrected for the effect of gravity on the apparent particle mobility. We averaged the values of the apparent mobilities measured at the same depth but with different field directions, cancelling out the effect of gravity. When we did not have data points at precisely the same depth for the two field directions, we fitted the apparent mobilities obtained for different field directions with one extra fit parameter: a constant representing the contribution of gravity to the apparent mobility of the particles, which was added to the parabolic function used to fit the mobility profiles.

Particle imaging was performed with confocal microscopy with an oil immersion objective (100× NA 1.4, 63× NA 1.4 or 40× NA 1.25, Leica), in fluorescence mode with 532 nm, 543 nm (both RITC) and 488 nm (NBD) excitation. We mostly used a Nipkow spinning-disk confocal microscope (CSU10, Yokogawa) in combination with a digital video camera (Evolution QEi). In some cases we used a Leica SP2 or Nikon C1 confocal microscope. We obtained series of images ($\sim$ 20–50 images; typical image size was 61 µm × 66 µm; pixel size was 0.23–0.45 µm; time interval between two frames was 0.2–0.7 s) at several depths (typically $\sim$ 10 positions across the 0.10 mm total depth). In most cases we took series of 2D images at different depths; in a few cases we took series of 3D image stacks. Typically, we changed the field direction after each series of images or image stacks.

We obtained the 2D trajectories of the particles using an algorithm described by Vissers et al. in Ref. [46], based on the 2D tracking code as described in Ref. [88]. Typically, for each series of images, we determined the trajectories of 10–50 particles, which could be followed in at least five consecutive frames. From the particle trajectories we calculated the (mean) apparent mobility of the particles (see above) in the direction of the electric field as a function of depth z in the capillary (mobility profile), given by

$$\mu(z) = v(z)/E, \tag{2.9}$$

with $v(z)$ the (mean) particle velocity (m s^{-1}) in the direction of the electric field at a certain depth z and E the field strength (V m^{-1}). The particle velocity is the sum of the fluid velocity (electro-osmotic flow velocity) at depth z and the particle velocity v_{E} with respect to the fluid as a result of the applied field; the corresponding particle mobility is $\mu_{\mathrm{E}} = v_{\mathrm{E}}/E$.

We fitted the mobility profile with a parabolic function. As explained above, for samples for which the direction of the electric field was parallel to the direction of gravity, we either averaged $\mu(z)$ for the two different field directions, or fitted with an extra fit parameter, a constant correcting for the sedimentation velocity.

We set $z = 0$ to correspond to the maximum of the parabolic profile and the middle of the capillary. At the stationary levels (at depth $z = z_{\mathrm{stat}}$), where the electro-osmotic flow was assumed to be zero, we could obtain the particle mobility $\mu_{\mathrm{E}} = \mu(z_{\mathrm{stat}})$. The stationary levels in a rectangular cell are located at [12]

$$\frac{z_{\mathrm{stat}}}{h} = \pm\sqrt{\frac{1}{3} + 4\left(\frac{2}{\pi}\right)^5 \frac{1}{k}}, \tag{2.10}$$

where h is half the depth of the channel and k the ratio between the long and short cross-sectional distances (width and depth) of the channel. We measured a depth of $2h \approx 108$ µm, which yields for the set-ups with U-shaped wires $k \approx 2 \times 10^3/108 \approx 18.5$ and $z_{\mathrm{stat}} \approx \pm 32.2$ µm. For the set-ups with straight wires $4(2/\pi)^5/k \ll 1/3$ and thus $z_{\mathrm{stat}} \approx \pm(1/3)^{1/2} h \approx \pm 31.2$ µm.

An estimate for the Debye screening length κ^{-1} was obtained from the measured conductivity of the solvent CHB (see below, Section 2.3.1). We used the theory of Carrique et al. [89] to obtain the dimensionless surface potential $\beta e \psi_0$ and charge number Z from the measured mobility. In this theory a Kuwabara cell model is used to calculate ψ_0 and Z from the measured mobility μ for any given screening length κ^{-1} and volume fraction η by numerically solving the full Poisson-Boltzmann equation; the double layers are allowed to overlap. In Ref. [46] the theory was used to relate the mobility to $\beta e \psi_0$ and Z for a system similar to our systems. As for our systems the plane of shear is close to the particle surface (at a distance of ~ 5 nm, the thickness of the steric stabilising layer), the electrostatic surface potential ψ_0 may be assumed to be similar to the zeta potential [18].

2.3 Results and discussion

2.3.1 Debye screening length

The conductivity of CHB after the cleaning steps was on the order of 10 pS cm^{-1}. From this, we obtained an estimate of the Debye screening length, in the following way (after Ref. [86] and chapter 2 of Ref. [18]). We assumed that the ions contributing to the conductivity of the solvent were H^+ and Br^- and that their concentrations were equal ($c_{H^+} = c_{Br^-} = c_s$). Furthermore, we assumed independent migration of ions, which should be a reasonable assumption in our dilute solutions. The conductivity D (S m^{-1}) is then related to the concentration of free ions through:

$$D = c_s \, \Lambda^0, \tag{2.11}$$

Table 2.1: Viscosities η and limiting molar conductance Λ^0 of HBr in CHB and ethanol (reference solvent). The viscosity of ethanol and Λ^0 in ethanol are literature values from Ref. [90] for $T = 298$ K (see also Refs. [18, 86]); the viscosity of CHB is from Ref. [18] and was measured at $T = 293$ K; Λ^0 in CHB was calculated from Eq. 2.12.

Solvent	η / (mPa s)	Λ^0 / (cm^2 S mol^{-1})
CHB	2.269	42.3
Ethanol	1.08	88.9

where c_s is the concentration (mol m^{-3}) of fully dissociated electrolyte (HBr) (note that the concentration of free ions is $2c_s$) and Λ^0 is the limiting molar conductance (m^2 S mol^{-1}) of the electrolyte in a particular solvent (CHB), i.e. the molar conductance at infinite dilution (as indicated by the superscript '0'). We used Walden's rule to obtain a (rough) estimate [70] for Λ^0 of HBr in CHB, as we do not know of available literature values. Walden's rule states that the product of the viscosity η_i of a solvent i and the limiting molar conductance Λ_i^0 of an electrolyte in that solvent is the same for different solvents:

$$\Lambda_1^0 \, \eta_1 = \Lambda_2^0 \, \eta_2, \tag{2.12}$$

where Λ_1^0 is the (unknown) limiting molar conductance in solvent 1, Λ_2^0 the (known) limiting molar conductance in reference solvent 2, and η_1 and η_2 are the viscosities of the respective solvents. We take ethanol as reference solvent 2, for which the limiting molar conductances of HBr (H^+ and Br^-) are known from literature. Table 2.1 summarises the literature values for the viscosities of ethanol and CHB, and the limiting molar conductance of HBr in ethanol, as well as the limiting molar conductance of HBr in CHB, calculated from Eq. 2.12.

Using the relation between conductivity and ionic strength from Eq. 2.11 and the value for Λ^0 of HBr in CHB from Table 2.1, we calculated that a conductivity $D = 10$ pS cm^{-1} corresponds to an ionic strength $c_s = 2.4 \times 10^{-10}$ mol L^{-1}. This results in a Debye screening length $\kappa^{-1} = 6$ µm (Eq. 2.4).

2.3.2 Mobility profiles

Typically, we measured two mobility profiles for each sample, at two different field strengths (see Table 2.2). We did not find a significant dependence of the mobility on the field strength. All measured mobility profiles on which the electrophoresis results in Table 2.2 were based are included as an appendix to this chapter (Section 2.6, Fig. 2.7). The given errors are the standard deviation of

the measurements on the same sample; they serve as a rough indication of the measurement error.

It is important to note that most samples containing one-component suspensions of locked particles (samples 1–3, 7 and 9) were crystalline before and also during the electrophoresis measurements. No shear melting of the crystals took place during the measurements. Three samples containing one-component suspensions of locked particles were not fully crystalline (samples 4, 6 and 8). Sample 6 was in the fluid state. Samples of similar composition as sample 6 (which were used in Chapter 5) were usually crystalline, indicating that the particle charge and/or Debye screening length may vary between the samples even though they were prepared in the same way. Sample 4 was crystalline within ~ 25 µm from both walls, but shear-molten in the middle of the capillary. Sample 8 was initially crystalline, but shear-melted during the first set of measurements, which yielded a mobility profile that did not look parabolic and was therefore not used to obtain the particle mobility. During the measurements for a second profile, which did have a parabolic shape, the sample was in a shear-molten state; the results from this second profile are included in Table 2.2 (sample 8). The remaining samples (5, 10 and 11), which contained the mixture and unlocked particles, were fluid. Since the mobility profiles for all samples, including the crystalline samples, could be well fitted with a parabolic function (Fig. 2.7), we assumed in all cases that the stationary levels were located at $z = z_{\mathrm{stat}}$ and that $\mu_{\mathrm{E}} = \mu(z_{\mathrm{stat}})$, as explained above (Section 2.2.2). For sample 5, in which a density gradient was present, this might not have been a valid assumption (see also Section 2.3.4).

Our findings are different from observations of Medebach and Palberg [73] in systems of polystyrene particles in water with $\sigma = 136$ nm, $(\kappa\sigma)^{-1} \approx 5$ and a volume fraction of a few percent; they found a distinct difference between the shape of the mobility profile for colloidal crystals and that for fluids or melts (shear-molten crystals). In their case, the profile for fluids and melts had the expected parabolic shape, whereas the profile for colloidal crystals was a flattened parabola at the start of the measurement and became completely flat (plug-like motion) on the timescale of a second. In addition, they observed shear melting of the colloidal crystals above a critical field strength, which increased with volume fraction (from $E \approx 3.5$ V mm^{-1} for $\eta \approx 0.0076$ to $E \approx 4.6$ V mm^{-1} for $\eta \approx 0.0090$). In contrast, we observed parabolic profiles for both fluid and crystalline samples, despite the fact that our measurements typically took ~ 30 seconds to several minutes. We observed shear melting twice, for samples 4 (partly) and 8, as described above. The measurements were performed at relatively high field strengths of $E = 7.6$ and 7.7 V mm^{-1}, respectively. We note that Medebach and Palberg [73] used particles with a diameter of 136 nm, 14–32 times smaller than our particles with $\sigma = 1.92$–4.36 µm. Medebach et al. [74] reported that, despite the non-parabolic

mobility profiles they found for colloidal crystals, the measured electrophoretic mobility seemed to be a single-particle property, not influenced by the structural state of the suspensions (fluid or crystal).

Our results show that it is possible to perform electrophoresis measurements on crystalline samples without shear banding or melting taking place during the measurement and that parabolic flow profiles can be obtained for those crystalline samples.

2.3.3 Surface potential and charge

Table 2.2 summarises the electrophoresis results. For each sample we report the type of set-up (see Fig. 2.1) and the field strengths E at which the measurements were performed. These are followed by the suspension properties: the name of the particle, whether the measurements were done in a one-component suspension or in a mixture, the mean diameter σ and polydispersity s of the particles as determined by static light scattering (SLS; particle U16, samples 10 and 5) or scanning electron microscopy (SEM; all other particles), the type of fluorescent dye used to label the particle, whether the particle was locked or unlocked, the volume fraction η of the suspension and the state of the suspension during the measurements (X = crystalline, F = fluid or S = shear-molten). Finally, in the last three columns of Table 2.2, we report the mean particle electrophoretic mobility μ_{E} as determined by electrophoresis, the dimensionless surface potential $\beta e\psi_0$ ($T = 298$ K) and the number of charges on the particle Z. The latter two were calculated from μ_{E}, assuming a Debye screening length κ^{-1} of 6 µm. The errors reported for μ_{E}, $\beta e\psi_0$ and Z are the standard deviations of multiple measurements for the same sample and thus are not available for samples on which only one measurement was performed.

The volume fraction for samples 1–9 was determined from a 3D data set by multiplying the number of particles by the particle volume and dividing by the volume of the box. For samples 10 and 11 a 3D data set was not available; therefore, the volume fraction was estimated from the amounts of PMMA (mass divided by mass density) and CHB (volume) used for suspension preparation. The volume fractions for samples 1–9 are different from $\bar{\eta} \approx 0.02$, aimed for during suspension preparation. This might be due to inaccuracies introduced by weighing and pipetting small amounts of particles ($\sim$ milligrams) and solvent ($\sim$ 100 µL) and to adsorption of particles to the wall of the capillary and probably also to the glass of the Pasteur pipette from which the sample cells were filled. Sample 5 was prepared with an overall volume fraction $\bar{\eta} \approx 0.02$, but was inhomogeneous due to sedimentation. In Table 2.2 we reported the local volume fraction at the stationary level ($\eta = 0.048$), which is the relevant volume fraction for relating μ_{E}

Table 2.2: Summary of the electrophoresis results for locked and unlocked PHSA-*g*-PMMA-stabilised PMMA particles in CHB. For each sample we report the type of set-up (see Fig. 2.1), field strengths E at which the measurements were performed, the name of the particle, whether the measurements were done in a one-component suspension or in a mixture, the mean diameter σ and polydispersity s as determined by static light scattering (SLS; particle U16, samples 10 and 5) or scanning electron microscopy (SEM; all other particles), the type of fluorescent dye used to label the particle, whether the particle was locked or unlocked, the volume fraction η, the state of the suspension during the measurements (X = crystalline, F = fluid, S = shear-molten), the mean particle mobility μ_E as determined by electrophoresis, the dimensionless surface potential $\beta e\psi_0$ (T = 298 K), and the number of charges on the particle Z, assuming a Debye screening length κ^{-1} of 6 µm. Sample 5 was a binary mixture, measured one day after mixing. Due to sedimentation, sample 5 was inhomogeneous; the volume fraction reported for sample 5 is the local volume fraction at the stationary level. The volume fraction for samples 1–9 was determined from a 3D data set; the volume fraction for samples 10 and 11 was estimated from the amounts of PMMA and CHB used for suspension preparation, as a 3D data set was not available for these samples. Values from the samples marked with an asterisk (*) were used to create the plots in Fig. 2.3.

Sample no.	Set-up	E / V mm^{-1}	Particle	single/ mixture	σ / µm	s (%)	Dye	Locked?	η	State	μ_E / 10^2 µm^2 V^{-1} s^{-1}	$\beta e\psi_0$	Z
1*	a	2.5, 3.5	L19	s	1.92	3.1	NBD	yes	0.014	X	11.7±0.3	4.88±0.09	588±19
2*	b	2.4, 3.4	L20	s	1.98	3.5	NBD	yes	0.018	X	8.6±0.3	4.22±0.10	452±20
3*	a	2.4, 3.3	L20	s	1.98	3.5	NBD	yes	0.011	X	13.5±0.4	5.04±0.13	682±29
4*	d	7.6	L20	s	1.98	3.5	NBD	yes	0.018	X+S	13.4	5.68	794
5	b	2.5, 3.5	L20	m	1.98	3.5	NBD	yes	0.048	F	12.55±0.01	6.950±0.005	1135±2
5	b	2.5, 3.5	U16	m	1.58	3.5	RITC	no	0.048	F	6.8±0.2	5.41±0.07	387±14
6*	a	2.3, 3.2	L22	s	2.23	3.6	NBD	yes	0.031	F	8.6±0.3	4.71±0.08	609±22
7*	a	2.5, 3.4	L29	s	2.87	2.4	NBD	yes	0.006	X	14.1±0.5	3.82±0.13	909±39
8*	d	7.7	L29	s	2.87	2.4	NBD	yes	0.022	S	15.3	5.88	1568
9*	a	2.6, 3.7	L44	s	4.36	2.8	NBD	yes	0.005	X	21.3±1.1	5.44±0.41	2960±400
10	a	2.5, 3.5	U16	s	1.58	3.5	RITC	no	0.02	F	6.04±0.04	3.90±0.01	249±2
11	c	3.5, 7.4, 7.4	U20	s	1.98	3.5	NBD	no	0.02	F	5.6±1.0	3.29±0.38	289±56

to $\beta e\psi_0$ and Z; we note, however, that this is the total volume fraction of L20 and U16 particles.

The electrophoretic mobility μ_E was obtained from a parabolic fit to the mobility profiles as described in Section 2.2.2. We used the theoretical approach of Ref. [89] to calculate the dimensionless surface potential $\beta e\psi_0$ and charge number Z from μ_E, using the values for η specified in Table 2.2 and $\kappa^{-1} = 6$ µm. All entries in Table 2.2 apply to one-component suspensions, except for those corresponding to sample 5, a mixture of particles L20 and U16, which will be discussed below (Section 2.3.4). For two particles (L20 and L29) we measured more than one sample of similar composition. The theory of Ref. [89] took into account the effects of overlapping double layers, which resulted in higher values for $\beta e\psi_0$ and Z than would follow from assuming a very low volume fraction and thus negligible double-layer overlap [46].

The variation in $\beta e\psi_0$ and Z between two samples of similar composition can be quite large, much larger than the error estimated from measurements on the same sample, as we see from the three samples containing L20 (samples 2–4) and the two samples containing L29 (samples 7 and 8). The volume fractions were different in these samples, but this should not have a large effect on the charge, as was shown in Ref. [46] for a system similar to our systems. Moreover, there seems to be no systematic dependence of the charge on the volume fraction. However, the samples were made at different points in time, with different dispersions, prepared from different batches of cleaned CHB. Also, we note that the electrophoresis cell was constructed separately for each sample, each time using a new capillary and new electrodes. These circumstances apparently affected the surface potential and charge of the particles.

All particles were found to be positively charged, from the direction of movement when the electric field was applied, in agreement with earlier work on similar systems [39, 46]. Electrophoresis measurements in previous work on similar systems (PMMA particles in CHB/*cis*-decalin) indicated that the type of dye did not significantly influence the charge (see chapter 2 of Ref. [18]). However, we observed that the locking state had an profound influence on the charge density of the particles. Locked particles clearly had higher surface potentials and charges than unlocked particles. This general trend is most clearly illustrated by comparison of particles L20 (samples 2–4) and U20 (sample 11). Particle L20 was obtained by locking a batch of particle U20. The surface potential and charge of particle L20 were significantly higher than those of particle U20. At present, we do not have a detailed explanation for the difference in charge between locked and unlocked particles. It seems probable that the locking procedure affects the surface chemistry of the particle surface, changing the adsorption equilibria of ions on the surface, and thereby increasing the surface charge density. It is possible

that some 2-dimethylaminoethanol (DMAE), which was added during the locking step (see Section 2.2.1), was adsorbed on/in the particles. As DMAE is relatively polar ($\epsilon_r = 17.18$ [91]), it might not have been completely removed by washing with hexane ($\epsilon_r \approx 2$). DMAE could have enhanced the adsorption of ions to the particles by providing groups in or on the particles for binding ions. For example, the N atom of the basic amino group of DMAE would be a likely candidate to bind H^+ ions.

Samples 10 and 11, containing unlocked particles, were in the fluid state, which is consistent with their lower surface potential and charge compared to the locked particles. We see this from the constant-potential and charge-regulation phase diagrams in Ref. [29] (for $\lambda_B/\sigma = 0.005$): a system with $(\kappa\sigma)^{-1} \approx 3$ and $\eta \approx 0.02$ (approximately as for our samples) is expected to be crystalline with bcc symmetry if $\beta e\psi_0 = 5$, but to be fluid when the surface potential is $\beta e\psi_0 = 3$. Sample 6, containing locked particles and having a potential close to $\beta e\psi_0 = 5$, was also in the fluid state. We see from Ref. [29] that this could be due to the relatively high volume fraction ($\eta = 0.031$) of sample 6. For certain combinations of parameters $\beta e\psi_0$ and $(\kappa\sigma)^{-1}$ re-entrant melting is expected to occur. For example, for $\lambda_B/\sigma = 0.005$, $\beta e\psi_0 = 5$ and $(\kappa\sigma)^{-1} \approx 4.1$ a fluid is stable for $\eta \gtrsim 0.031$ [29].

2.3.4 Binary mixture

In Fig. 2.2 we plotted two mobility profiles for two one-component samples (samples 3 and 10; filled and open black circles), containing particles L20 and U16, respectively. The two profiles were measured at different field strengths, ~ 2.5 V mm^{-1} (filled black circles) and 3.5 V mm^{-1} (open black circles). The five vertical dashed lines indicate the positions of the walls ($z = \pm 54$ µm) and the middle of the capillary ($z = 0$ µm), as well as the two stationary levels (where the electro-osmotic flow is zero; $z = z_{stat}$; Eq. 2.10). The mobility of the particle is given by the value of the mobility profile at the position of the stationary levels. We see that the two profiles measured at different field strengths in each case give almost the same value for the particle mobility.

We also measured the mobility profiles for the same particles in a binary mixture one day after mixing. The green and red triangles in Figs. 2.2a and b correspond to particles L20 (green) and U16 (red), respectively, in the binary mixture (sample 5). Again, the two profiles were measured at different field strengths, ~ 2.5 V mm^{-1} (open green/red triangles) and 3.5 V mm^{-1} (filled green/red triangles). We note that the particles in this sample had sedimented significantly, leaving approximately half the depth of the capillary empty (the region in Figs. 2.2a and b without triangular data points). Despite the density gradient in the sample the profile could be well approximated by a parabolic function. There-

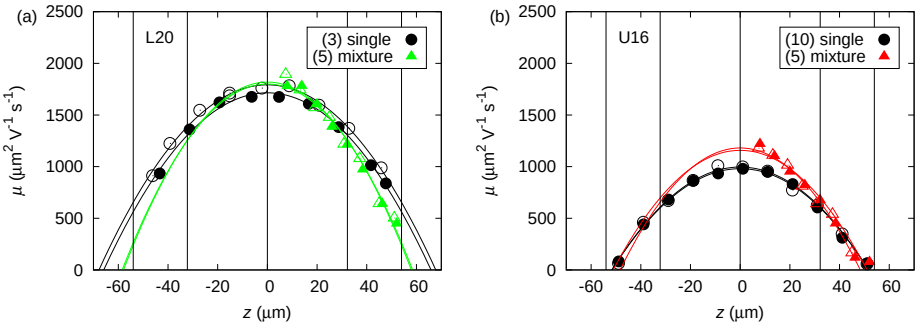

Figure 2.2: Mobility profiles for locked and unlocked PHSA-*g*-PMMA-stabilised PMMA particles in CHB. (a) Locked particles (L20, samples 3 and 5) and (b) unlocked particles (U16, samples 10 and 5), measured in a one-component suspension (black circles) and for the particles in the (same) binary mixture (green or red triangles). For sample 3 the data and fits have been corrected for the contribution of gravity to the apparent mobility of the particles (see Section 2.2.2). Experimental details for these samples are in Table 2.2. The profiles for all samples reported in Table 2.2 can be found in the appendix to this chapter (Section 2.6, Fig. 2.7). See text for details.

fore, we assumed that the location of the stationary levels was still given by Eq. 2.10 and obtained the mobility of the particles from the corresponding value of the parabolic fit. As can be seen from Fig. 2.2, we found similar mobilities for the particles in the binary suspension (sample 5) and for the corresponding one-component suspensions (samples 3 and 10). However, since the measurements were performed at a different local volume fraction (at the stationary level), this results in different values for $\beta e\psi_0$ and Z. The values of $\beta e\psi_0$ and Z for particles L20 and U16 in sample 5 are much higher than the same values in samples 2–4 (L20) and 10 (U16). It seems unlikely that this is the case, given the similar way in which the suspensions were prepared. We used the theory of Ref. [89] to calculate $\beta e\psi_0$ and Z from μ_{E} for sample 5, using the total volume fraction at the stationary level ($\eta = 0.048$). However, the theory of Ref. [89] is valid for one-component suspensions and might not be accurate for the binary mixture of sample 5. Furthermore, due to the density gradient in sample 5, the stationary levels might be at different locations than we assumed, i.e. Eq. 2.10 might not be valid for sample 5. A different location of the stationary level would also correspond to a different local volume fraction. Both factors might yield significantly different values for $\beta e\psi_0$ and Z. A solution would be to prevent a density gradient across the depth of the capillary (in the z direction) by measuring a sample like sample 5, in which sedimentation effects are not negligible, using a vertical set-up (as in Fig. 2.1a or c).

Although we cannot establish the precise values for $\beta e\psi_0$ and Z in the binary mixture, we can draw the following conclusions from the mobility profiles. First, both particles were positively charged, because they both moved in the same direction across (almost) the entire depth of the capillary. Only very close to the wall did the smaller particles move in the opposite direction. Thus, at the location of stationary level, which is not precisely known but expected to be much further from the wall, the smaller particles moved in the same direction as the larger particles, indicating that both particles were positively charged. Second, the charge on the smaller U16 particles was lower than the charge on the larger L20 particles, as the smaller particles had a smaller apparent mobility at all depths.

2.3.5 Size dependence of surface potential and charge

Figs. 2.3a and b show, for the locked particles, the dimensionless surface potential $\beta e\psi_0$ and charge number Z, respectively, as a function of the diameter of the particles σ. We plotted the data for samples 1–4 and 6–9 (marked with an asterisk in Table 2.2), corresponding to particles L19, L20 (3×), L22, L29 (2×) and L44. All these samples contained locked particles with diameters in the range 1.92–4.36 µm. Samples 1, 3, 6, 7 and 9 and were prepared using the same batch of purified CHB. The values for $\beta e\psi_0$ (red squares in Fig. 2.3a) and for Z (red squares in Fig. 2.3b) corresponding to $\kappa^{-1} = 6$ µm, were taken from Table 2.2. To show what the effect is of using slightly different estimates for κ^{-1}, we also included $\beta e\psi_0$ and Z values, obtained from a similar cell model calculation carried out for $\kappa^{-1} = 4$ µm (green triangles pointing down) and 8 µm (blue triangles pointing up). In general, assuming a smaller screening length yields a smaller $\beta e\psi_0$ (Fig. 2.3a) and a larger Z (Fig. 2.3b). For the smaller particles, varying the estimate for κ^{-1} in the range 4–8 µm has little effect on the calculated charge. For the largest particle, the effect can be quite substantial, especially when lowering the estimate of κ^{-1} (the data point for Z corresponding to $\kappa^{-1} = 4$ µm for the largest particle is off the scale of the graph in Fig. 2.3b).

Fig. 2.3a shows that the surface potential is approximately constant, independent of the size of the particle, in agreement with results of Roberts et al. [45], who also found a size-independent surface potential; however, in their case in a system with added surfactants to control the charge. A fit to our data for $\kappa^{-1} = 6$ µm resulted in $\beta e\psi_0 = 5.0 \pm 0.3$ (for $\kappa^{-1} = 4$ and 8 µm the fits gave $\beta e\psi_0 = 4.3 \pm 0.3$ and 5.5 ± 0.3, respectively). In Fig. 2.3b we see that the data points of Z versus σ can be approximated by a parabolic fit of the form $y = ax^2$, which is also plotted in the figure, suggesting a roughly constant surface charge density on the particles ($Z \propto \sigma^2$), for this range of particle diameters. The inset of Fig. 2.3b makes this more clear. Here, we show Z as a function of the surface area of the particle,

given by $\pi\sigma^2$. The line plotted through the data is a linear fit to the data. The slope is equal to the surface charge density divided by the elementary charge e, and correspond to surface charge densities of 49 ± 3 e µm^{-2} (58 ± 4 e µm^{-2} and 47 ± 3 e µm^{-2} for $\kappa^{-1} = 4$ and 8 µm, respectively). Our results for the surface potential and surface charge density are comparable to values measured in Ref. [46] for systems of PMMA particles ($\sigma \approx 1$ µm) in CHB/*cis*-decalin with $\epsilon_r = 5.6$ for the solvent mixture and $(\kappa\sigma)^{-1} \approx 1$ (in Ref. [46] for $\eta \lesssim 0.04$: $\beta e\psi_0 \approx 3$–4 and surface charge density ~ 80 e µm^{-2}).

The dark grey shaded area in Fig. 2.3b is bound on the lower side by the line $Z = \sigma/\lambda_B$ and on the upper side by the line $Z = Z_{sat} = 3\sigma/\lambda_B$. The light grey shaded area is bound on the upper side by the line $Z = Z_{sat} = 4\sigma/\lambda_B$. The lower bound of the dark grey area indicates above which charge renormalisation effects become relevant [78, 92]. The upper bound is an indication of the maximum charge (saturated charge Z_{sat}) that a particle can acquire [80, 92], when charge renormalisation is taken into account.

Alexander et al. proposed the relation $Z_{sat} = A\sigma/\lambda_B$ for the saturated charge [16]. The proportionality constant A was found to depend on the volume fraction η and salt concentration c_s. Experiments [78], simulations [79] and two theoretical approaches, using the Poisson-Boltzmann cell model and the jellium model [16, 80, 93], all found $A \approx 3$–4.5 for the volume fraction range 10^{-3}–10^{-2}. In accordance with these values, we made the lines corresponding to $A = 3$ and 4 the upper bounds of the dark grey and light grey shaded area, respectively.

The shaded areas thus indicate possible renormalisation regimes for the particle charge. As the theory in Ref. [89], which we used to obtain $\beta e\psi_0$ and Z from the mobility, employs the non-linearised Poisson-Boltzmann (PB) theory, the corresponding charges are *not* renormalised charges. The renormalised charges would follow from matching the linear to the non-linear PB solution at the cell boundary [93] and are expected to saturate at a value Z_{sat} when the bare charge (i.e. the charge that follows from the non-linear PB solution) exceeds this value. The bare charge for all particles is in or above the renormalisation regime (grey areas) and therefore the renormalised charge is expected to be lower than the reported bare charge.

2.3.6 Alternating strings

We performed electrophoresis measurements on a binary mixture of particles L20 and U16 one day after mixing (sample 5). Mixtures of this composition were also used in Chapter 6 to achieve the colloidal Brazil-nut effect. When checking one of the samples that had been prepared two days earlier, we observed alternating strings: strings consisting of alternating L20 (green) and U16 (red) particles (see

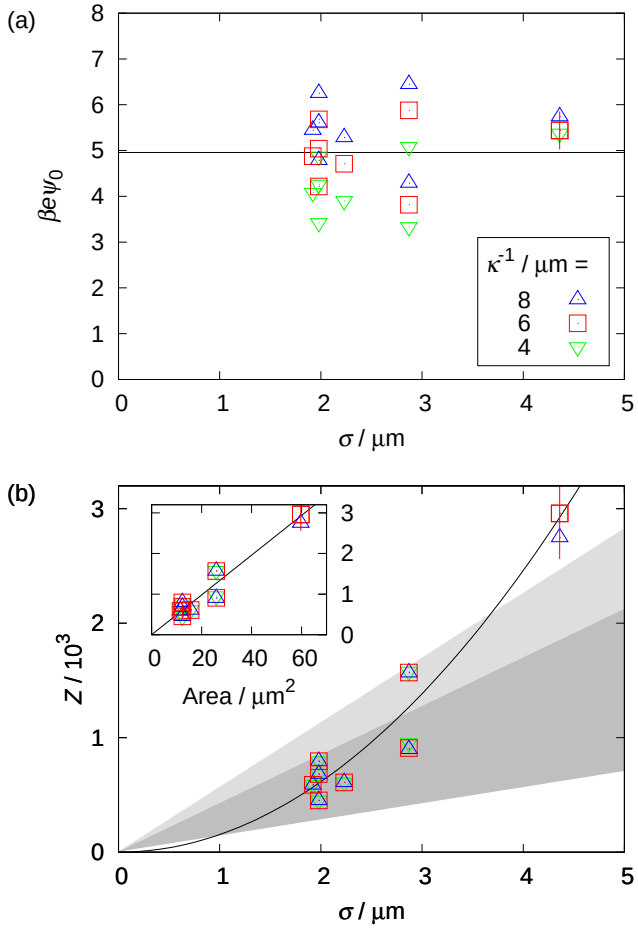

Figure 2.3: Surface potential and charge number versus diameter for locked PHSA-*g*-PMMA-stabilised PMMA particles in CHB for different estimates of the Debye screening length κ^{-1}. (a) Dimensionless surface potential $\beta e\psi_0$ versus diameter σ. (b) Charge number Z versus diameter σ; inset: charge number Z versus the surface area $\pi\sigma^2$ of the particles. Error bars are shown only for the largest particle (for $\kappa^{-1} = 6$ μm) and correspond to the errors given in Table 2.2; for all other particles the error bars are smaller than the point size. The grey shaded areas indicate possible charge renormalisation regimes. See text for details.

Fig. 2.4a). The strings consisted almost exclusively of this alternating sequence: red particles had green neighbours and green particles had red neighbours. Sometimes we encountered a red particle flanked by a green and a red neighbour. We ascribe this to the incorporation of a pre-existing red-red dumbbell into the string, as we occasionally also observed free red-red dumbbells in the binary suspensions. The strings were not rigid, but quite flexible: the bond angles in a string were not entirely fixed. From the image in Fig. 2.4a it is clear that the particle-particle interactions between particles in a string and free particles is still long-range repulsive: the green particles stay far apart.

One explanation for the occurrence of these alternating strings could be that the two particle species had become oppositely charged. To check this, we did electrophoresis measurements on a binary mixture (sample 5) in which a few green-red clusters had formed (one day after mixing), but we saw no indication that the particles had acquired net charges of opposite sign (Section 2.3.4). We take the presence of a few green-red clusters as an indication that the interactions in this measured sample were close to those in the sample where extensive string formation took place (two days after mixing). As there were far more single particles than clusters, the clusters presumably had a negligible effect on the measured mobility profiles. Thus, the system contained two species of like-charged (positively charged) particles, which spontaneously formed alternating strings. From the electrophoresis measurements on the one-component suspensions (samples 2–4 and 10) and the mixture (sample 5), we know that the green particles had a higher charge than the red particles (see Table 2.2). We hypothesise that a higher-charged green particle, upon approaching a lower-charged red particle, could induce a patch of opposite charge on the red particle, which then caused the green and red particle to attach (see also chapter 9 of Ref. [94]).

In previous experiments with samples containing a *one-component* suspension and a deionised water phase, we observed that sometimes small clusters formed near the CHB-water interface (Fig. 2.5). Inspired by these observations, we prepared a sample containing the binary suspension of L20 and U16 particles adjacent to a deionised water phase. Indeed, the presence of the water phase strongly promoted the formation of extended alternating strings and clusters (see Figs. 2.4b and c). Close to the water phase (Fig. 2.4c) we observed alternating clusters that were more compact than strings, but still quite extended (alternating meaning here that green particles had red neighbours and vice versa). Further from the water phase we observed a network of alternating strings (Fig. 2.4b). These strings appeared less flexible than in the sample without water (Fig. 2.4a). At other places in the capillary, below and above the network of strings, we encountered shorter strings, small clusters and single green and single red particles (see Fig. 2.6 for typical images). At this point, we do not know what the mechanism is behind the

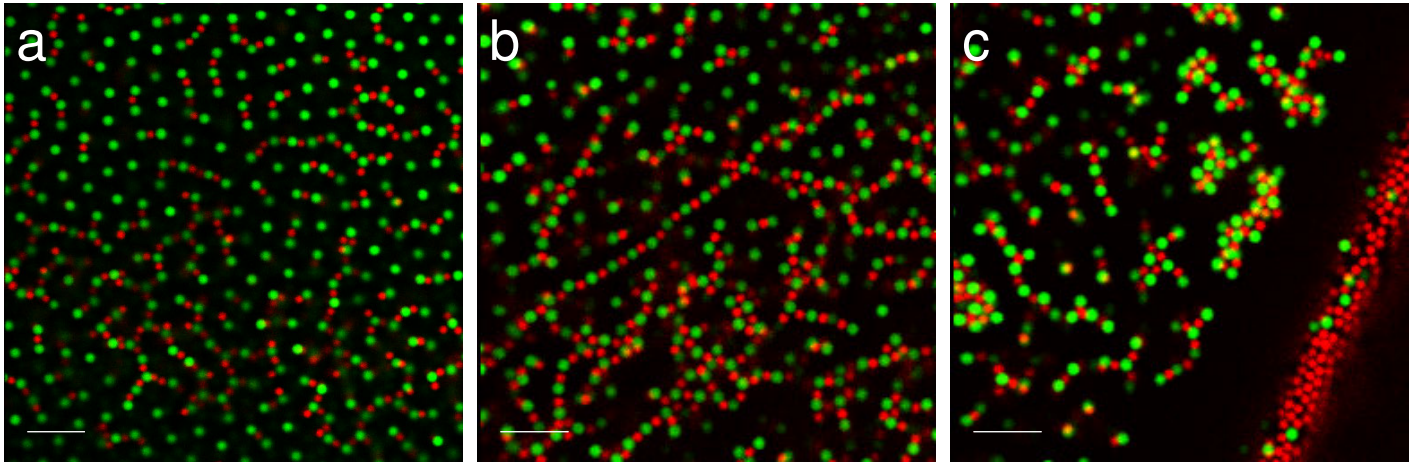

Figure 2.4: Alternating strings formed in binary suspensions of large (green) and small (red) particles in a system (a) without deionised water; two days after mixing. (b) In contact with deionised water; 0.2 mm from CHB-water interface, $\sim$ 6.5 hours after mixing. (c) Extended clusters near CHB-water interface; $\sim$ 4.5 hours after mixing. Particles are adsorbed to the CHB-water interface, making the interface clearly visible; the water phase is on the right, the CHB phase, containing the clusters, is on the left. Scale bars indicate 10 µm.

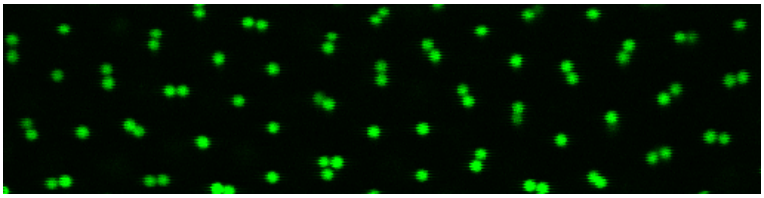

Figure 2.5: Clusters (mostly dumbbells) formed in a suspension of locked PMMA particles (σ = 2.23 µm) in CHB; 0.3 mm from CHB-water interface, two days after sample preparation. Image size: 125.1 µm × 31.3 µm.

enhanced formation of clusters in the presence of water. Previous work showed that the water phase may take up ions from the CHB phase [40], reducing the ionic strength and thus changing the particle interactions. A lower ionic strength corresponds to a larger $(\kappa\sigma)^{-1}$ and may lead to a lower charge on the particles through particle discharging [29]. It seems unlikely that water itself plays a role in string formation, as we also observed clusters and strings in suspensions made with purified CHB in samples in which no water phase was present (Fig. 2.4a).

Further information on the mechanism of cluster formation could come from analysis of the attachment processes. We succeeded in capturing a few of the rare attachment events with confocal microscopy. We prepared a sample containing the binary suspension and deionised water and put this vertically, with the water phase on top and gravity pointing along the length of the capillary. The particles (having a lower density than CHB) sedimented towards the CHB-water interface. We recorded movies of $\sim$ 1000 frames at a rate of $\sim$ 1 frame per second. By careful inspection of the movies we were able to find rare attachment events where a green particle and a red particle approached each other and attached. Fig. 2.6 shows two series of images depicting attachment events. In the first series (Figs. 2.6a–d) a green member of a green-red dumbbell attaches to a red particle, which is part of a alternating string. Note that the red member of the green-red dumbbell is not visible in frames a and b and only barely visible in frames c and d. In the second series (Figs. 2.6e–h) a single red particle attaches to a green particle, which is part of a green-red dumbbell. In both cases the white arrows indicate the two attaching particles in the frame right before and right after attachment. Dynamically, the attachment was simply visible as a transition from two particles moving rather independently of each other to two particles moving coherently and staying at short distance from each other (see movies in the supplementary information [95]). A more detailed investigation of these events would be needed to better understand the mechanism of cluster and string formation.

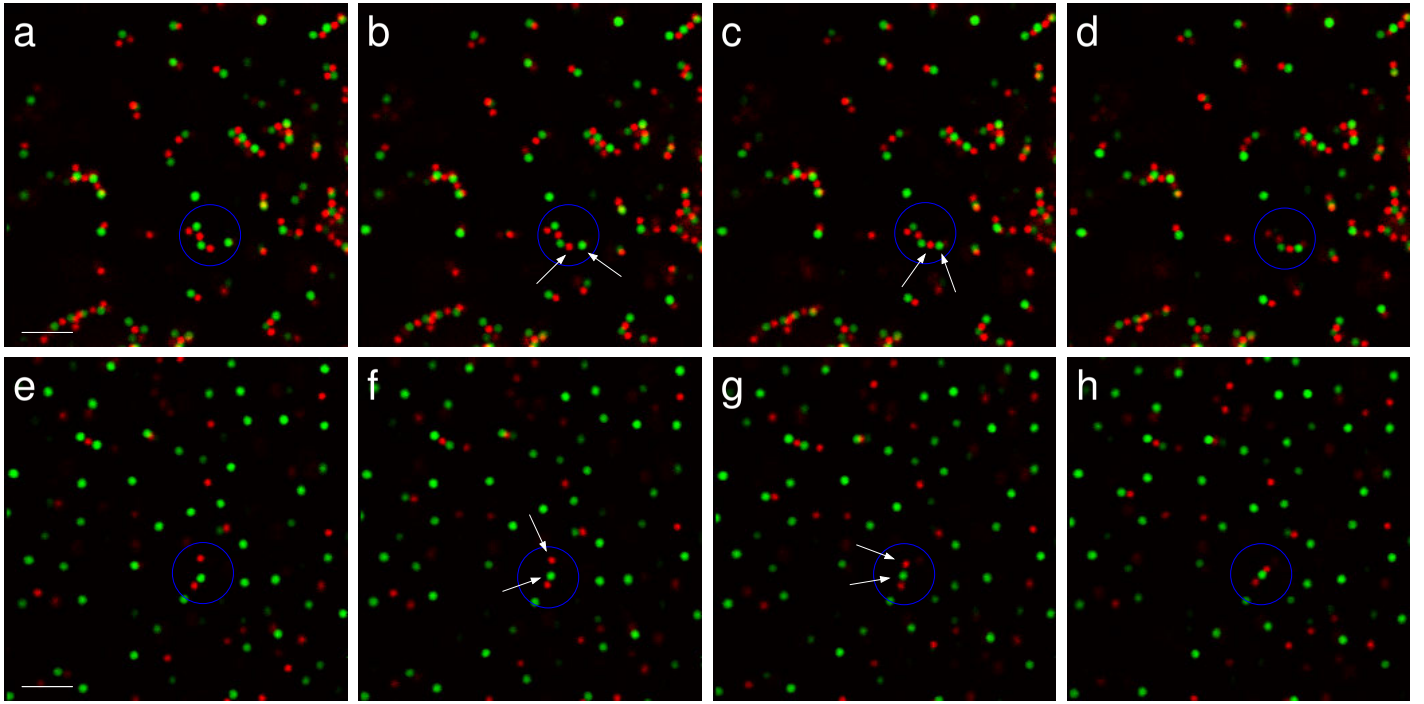

Figure 2.6: Two sequences of four confocal images (a)–(d) and (e)–(h) showing the attachment of a large (green) and small (red) particle. The images were taken 1.3 mm and 1.1 mm from the CHB-water interface, ~ 1 hours and ~ 4 hours after mixing, respectively. In each case we show, from left to right, two images that were taken before attachment, followed by two images taken after attachment. The arrows indicate the two particles involved before and after attachment. The time step between two consecutive images was 1.04 s. The scale bars indicate 10 µm. The corresponding movies are available in the supplementary information [95].

2.4 Conclusions

We determined the size dependence of the dimensionless surface potential $\beta e\psi_0$ and particle charge number Z in suspensions of PHSA-g-PMMA-stabilised poly(methyl methacrylate) (PMMA) particles in cyclohexyl bromide (CHB) with diameters in the range $\sigma = 1.92$–4.36 µm. From the conductivity of CHB, the Debye screening length κ^{-1} was estimated to be 6 µm. We performed electrophoresis measurements in home-made electrophoresis sample cells, using confocal microscopy to measure the particle velocity profiles, from which we obtained the electrophoretic mobility μ_{E} for each particle species. To calculate the $\beta e\psi_0$ and Z from μ_{E} we employed the theoretical approach by Carrique et al. [89], which takes into account double-layer overlap and uses a Kuwabara cell model to relate μ_{E} to $\beta e\psi_0$ and Z for arbitrary κ^{-1} and volume fraction η by numerically solving the full Poisson-Boltzmann equation.

We used mostly locked particles (for which the stabiliser is covalently bonded to the particle surface), but also some unlocked species (stabiliser adsorbed to the particle surface) for our measurements. We found that the locking state of the particles had a profound influence on their surface potential. Unlocked particles had a significantly lower surface potential and charge ($\beta e\psi_0 \approx 3.3$–$3.9$) than locked particles ($\beta e\psi_0 \approx 3.8$–$5.9$). For locked particles we found a roughly constant surface potential (a fit yields $\beta e\psi_0 = 5.0 \pm 0.3$), independent of the size of the particle, and a (bare) particle charge that was proportional to the square of the diameter, corresponding to a surface charge density of roughly $49 \pm 3\ e\ \mu\mathrm{m}^{-2}$.

In a binary suspension of two charged particle species, we observed spontaneous formation of flexible alternating strings. We measured the surface potential and charges in the binary system and found that both species were positively charged, but had charges of different magnitude. We speculate that the higher-charged species induced a patch of opposite charge on the lower-charged species, inducing attractions between the two species, which resulted in the formation of alternating strings.

In future work, it would be interesting to extend the $\beta e\psi_0$-versus-σ and Z-versus-σ curves to even smaller and larger particle diameters than in the present work ($\sigma = 1.92$–4.36 µm), and to address the role of the screening length through addition of salt. Questions relating to the details of the particle interactions remain open – for example, the question of why locked particles are significantly higher charged than unlocked particles and how the particle-particle interactions in binary mixtures can be described. The answers would certainly help to gain more insight in the charging mechanisms in suspensions of PMMA particles in CHB and similar solvents.

2.5 Acknowledgements

I am grateful to Teun Vissers for an introduction to the experimental procedure of microelectrophoresis, and for providing his particle tracking algorithm and the cell model code by Félix Carrique and Angèl Delgado. I would like to thank Peter Helferich for his useful technical assistance, and Johan Stiefelhagen (RITC-labelled particles) and Gulşen Heessels-Gürboğa (NBD-labelled particles) for particle synthesis. Johan Stiefelhagen is also thanked for his help with the locking procedure and useful discussions on PMMA synthesis.

2.6 Appendix

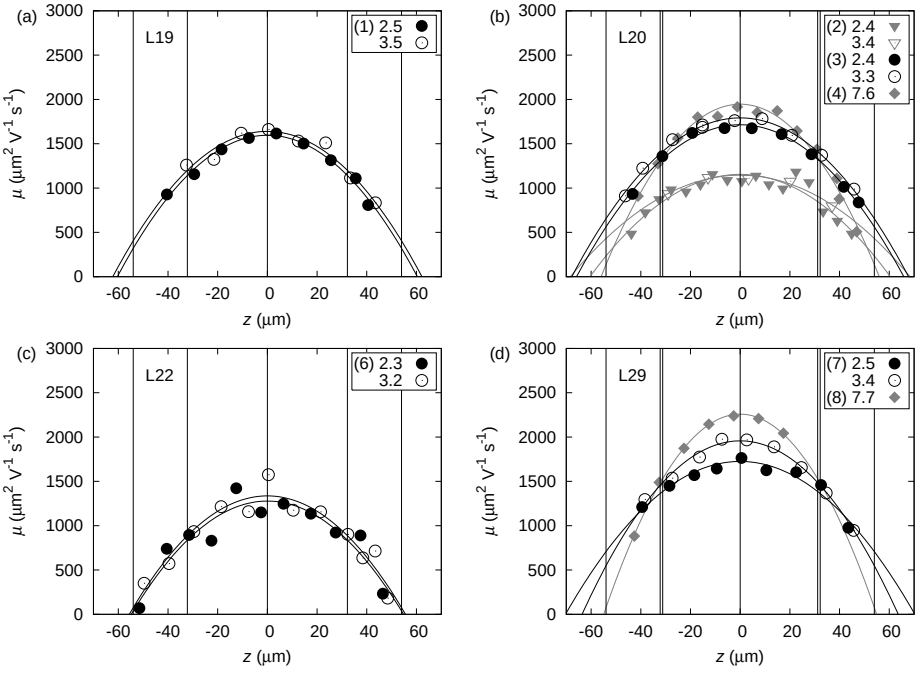
(a)
L19
(1) 2.5
3.5
(b)
L20
(2) 2.4
3.4
(3) 2.4
3.3
(4) 7.6
(c)
L22
(6) 2.3
3.2
(d)
L29
(7) 2.5
3.4
(8) 7.7
μ (μm² V⁻¹ s⁻¹)
z (μm)

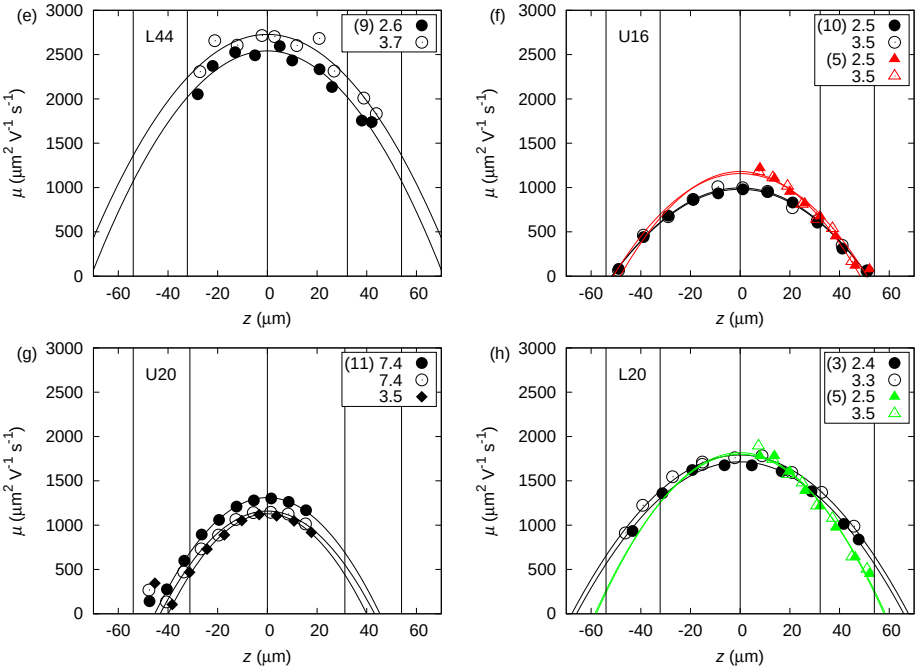

Figure 2.7: ((a)–(d) on previous page) Mobility profiles for locked and unlocked PHSA-*g*-PMMA-stabilised PMMA particles in CHB, corresponding to the samples reported in Table 2.2: (a) L19, sample 1; (b) L20, samples 2–4 (one-component) and 5 (mixture with U16); (c) L22, sample 6; (d) L29, samples 7 and 8; (e) L44, sample 9; (f) U16, samples 10 (one-component) and 5 (mixture with L20); (g) U20, sample 11; (h) L20, samples 3 (one-component) and 5 (mixture with U16). Each panel corresponds to one type of particle, as labelled. Panels (h) and (f) show the same data as Figs. 2.2a and b. The legend gives the sample number in brackets followed by the field strength E in V mm^{-1}. Each legend entry corresponds to one mobility profile. The five or seven vertical dashed or dotted lines in each panel indicate the positions of the walls ($z = \pm 54$ µm) and the middle of the capillary ($z = 0$ µm), as well as the two stationary levels (where the electro-osmotic flow is zero; $z = z_{\mathrm{stat}}$; Eq. 2.10). Samples 4, 8 and 11 had straight wires as electrodes, with $z_{\mathrm{stat}} \approx \pm 31.2$ µm (dotted lines). All other samples had U-shaped wires as electrodes, with $z_{\mathrm{stat}} \approx \pm 32.2$ µm (dashed lines). For samples 1, 3, 6, 7, 9 the data and fits have been corrected for the contribution of gravity to the apparent mobility of the particles (see Section 2.2.2). For further experimental details see Table 2.2.

3

Effect of size polydispersity on the crystal-fluid and crystal-glass transition in hard-core repulsive Yukawa systems

We investigated the effect of size polydispersity on the crystal-fluid transition in hard-core repulsive Yukawa systems by means of Monte Carlo simulations for several state points in the Yukawa parameter space. Size polydispersity was introduced in the system only with respect to the hard particle cores; particles with different diameters had the same surface potential ψ_0, but the charge per particle was not varied with volume fraction or distance. We observed a shift of the crystal-fluid transition of bulk crystals with a fixed log-normal size distribution to higher volume fraction upon increasing the polydispersity. The shift was more pronounced for weakly charged particles ($\beta e\psi_0 \approx 1$, with $\lambda_B/\bar{\sigma} = 0.01$) compared to more highly charged particles ($\beta e\psi_0 \approx 2$), and also more pronounced for larger Debye screening length. At high polydispersities (≥ 0.13) parts of the more highly charged systems that were initially crystalline became amorphous. The amorphous parts had a higher polydispersity than the crystalline parts, indicating the presence of a terminal polydispersity beyond which the homogeneous crystal phase was no longer stable.

3.1 Introduction

For certain charge-stabilised colloidal systems, such as well-index-matched particles and/or colloids with a thick enough steric stabilising layer, the always-present and attractive Van der Waals forces can be neglected [1]. The interactions between such like-charged colloids can be described by the hard-core repulsive Yukawa (screened Coulomb) potential, an effective pair potential that results after the degrees of freedom of the microions have been integrated out. The equilibrium phase behaviour of colloidal spheres interacting through a Hard-Sphere-Yukawa (HSY) potential is well known from computer simulations [26–28] and experiments [10, 19, 30, 39, 86, 96]. In the (volume fraction η, Debye screening length $(\kappa\sigma)^{-1}$) plane of the phase diagram, a fluid is found at low volume fractions and two different crystal structures at higher volume fractions: a face-centred-cubic (fcc) crystal at small screening lengths and a body-centred-cubic (bcc) crystal at larger screening lengths and moderate volume fractions, flanked by an fcc crystal at higher volume fractions. The exact locations of the phase boundaries depend on the details of the model system, i.e. the charge on the colloids, the salt concentration and the dielectric constant of the solvent.

Almost all phase diagrams for the HSY systems were calculated under the assumption that the particles are monodisperse in size, i.e. that all particles have the same diameter, and many for a fixed contact value of the interaction potential [26–28]. In real colloidal dispersions, however, both are never truly the case. In an experimental system the distribution of particle diameters is determined by the synthesis of the particles and can approximately be described by a Gaussian or log-normal distribution [1]. The system can be viewed as containing an effectively infinite number of particle species (each having a different diameter), and we call the system therefore size *poly*disperse [97]. The polydispersity is commonly defined as the ratio of the standard deviation and the mean of the size distribution. In experimental systems the charge on the particles is affected by the local chemical potential of the charge-determining ions; the two limiting cases are described by assuming constant-charge or constant-potential boundary conditions on the particle surface [12].

For the case of hard spheres (or approximations thereof), phenomena arising from the presence of polydispersity have been investigated theoretically [20, 98–107], computationally [99, 105–109] and experimentally [8, 9, 110, 111] (for a review see Ref. [97]). We first consider the case of quenched polydispersity, i.e. where the polydispersity in the coexisting phases is kept (nearly) constant and where fractionation is thus not allowed. In experiments it has been observed that above a certain value of the polydispersity, crystallisation in the system does not occur [8]. This *terminal polydispersity* is thought to arise because with increasing polydis-

persity the particles fit less well on the crystal lattice and the crystal structure is destabilised. At sufficiently high polydispersity the free energy of the fluid becomes lower than that of any crystal phase. The terminal polydispersity is the maximum polydispersity that a single stable crystalline phase can have. Several theoretical and computational studies provide estimates for the value of the terminal polydispersity (ranging from ~ 0.05 to 0.12), see, e.g. Refs. [20, 98, 99, 108]. For polydispersities just below the terminal polydispersity *re-entrant melting* was found at higher volume fractions in theoretical work [100] and experiments [110]. Others report a crystal-to-glass transition instead, due to the presence of an equilibrium glassy phase at high densities and high polydispersities [103]; also experimentally, a polydispersity-induced crystal-to-glass transition has been observed [111]. These findings could be explained by noting that with increasing polydispersity, the maximum volume fraction for an ordered 3D crystal decreases, while it increases for a fluid or disordered glassy state [99, 109], making the fluid or glass the thermodynamically stable phase at high volume fractions [100].

For systems interacting through a softer pair potential than the hard-sphere potential, terminal polydispersities have been found as well. Monte Carlo simulations revealed a crystal-to-glass transition in systems of polydisperse charged colloids interacting through a HSY pair potential [112]. In semigrand ensemble simulations a terminal polydispersity was reported for a soft-sphere system, which increased with increasing potential softness [113]. In recent simulation work a terminal polydispersity as well as re-entrant melting were found for HSY systems with quenched size polydispersity using free energy calculations [114].

A common feature in the above-mentioned theoretical and computational studies is that the polydispersity in the coexisting phases was kept constant. For the hard-sphere system, simulations were also carried out under different conditions where the size distribution in the coexisting phases was allowed to vary. This gives rise to the phenomenon where the system splits into two or more coexisting phases with different polydispersities, so-called *fractionation*. One scenario where fractionation occurs is when a fluid with large size polydispersity (~ 0.12) coexists with a crystal that has a narrower size distribution (~ 0.06) [101]. However, the simulations that led to this result were carried out in the semigrand canonical ensemble, which fixes the chemical potential differences for different particle sizes with respect to some reference particle, but not the overall particle size distribution in the system, thus allowing for variable polydispersity. Later, solid-fluid coexistence with fractionation was found in more realistic theory and simulation work for the experimentally relevant situation of a fixed overall size distribution [102, 106]. Also, in theoretical and computational studies the coexistence of multiple solid phases was found, each with a narrow size distribution, in a system with a large overall polydispersity and a fixed overall size distribution [102, 105, 107].

It should be noted here that, when given enough time, a system can of course always divide itself up in less polydisperse subsystems that then may form crystal phases. However, since fractionation requires significant long-distance particle diffusion, it is expected that in experimental systems extensive fractionation will take (inaccessible) long times [104].

The outcome of experiments on systems with polydisperse particles will thus be determined not only by equilibrium thermodynamics, but also by *non-equilibrium phenomena*. The above-mentioned experimentally observed absence of crystallisation above a certain polydispersity value could also be due to slow dynamics (the dynamic glass transition), or high nucleation barriers, which are known to increase with polydispersity [8, 115]. Simulations on a soft-sphere system predict that while a first-order freezing transition is present up to a polydispersity of 0.45, non-equilibrium effects will dominate in experiments at polydispersities above 0.12 [116].

Most experiments on HSY systems have been performed on colloidal systems where the double-layer thickness κ^{-1} is smaller than the particle diameter σ. However, recently there has been renewed interest in long-range systems where the double-layer thickness is on the order of the particle size or larger [39, 117]. Inevitably, polydispersity is present in these experimental systems as well, although the non-linear double-layer interaction is expected to make its effects on phase behaviour less strong than for hard-sphere systems. Preliminary experimental observations indicate that the long-range interactions enable the crystal structure to accommodate a very large polydispersity [18]. In this work we move beyond the simple hard-sphere-like colloidal systems and investigate the phenomena arising from the presence of polydispersity in systems in which the particles interact through a hard-core repulsive Yukawa potential.

Experiments indicate that in systems of charge-stabilised colloidal particles suspended in apolar or low-polar solvents the charge on the colloids is volume-fraction-dependent [46, 86, 118–120]. The interactions in these HSY systems are therefore more accurately described by constant-potential or charge-regulation boundary conditions than constant-charge boundary conditions [119–121]. Only recently, phase diagrams for HSY systems were calculated within the constant-potential and charge-regulation model [29]. Use of these models requires calculation of the volume-fraction-dependent effective colloidal charge and effective screening length. Because of these technical difficulties the present simulations were started with all particles having the same surface potential, but the charge was not a function of the volume fraction or distance between the particles.

We used Monte Carlo simulations to study the effect of polydispersity on the behaviour of hard-core Yukawa systems. It was found that Monte Carlo simulations in which physically relevant moves (small particle displacements) are used,

are a correct and efficient way to investigate the dynamics in colloidal systems [122–124]. Molecular dynamics simulations are less appropriate to describe the dynamics in suspensions of colloidal particles, as they employ Newtonian dynamics rather than the Brownian dynamics which is operative in colloidal systems. We expect only limited fractionation, to the extent introduced by the selected initial configuration and allowed for by the diffusion of the particles on simulation timescales.

We note that NVT Monte Carlo simulations are not a suitable technique to establish the equilibrium behaviour of a polydisperse system, as was pointed out in Ref. [106]. The behaviour of the system at coexistence will be dominated by finite-size effects, which can be more severe in polydisperse systems compared to monodisperse systems, because in polydisperse systems some phases may occupy only a very small volume when the constituting particle sizes are under-represented in the overall size distribution. Furthermore, the use of fixed particle sizes in combination with slow diffusion, as is the case for our system, means that fractionation is very slow and on simulation timescales equilibrium is not reached. The results might be indicative of what could happen in an experiment in which a polydisperse system is allowed to crystallise at a low volume fraction and is subsequently slowly compressed, for example by gravity. For certain combinations of parameters sufficiently slow compression is expected to preserve the crystalline structure up to the volume fraction where the lattice spacing becomes too small to accommodate the spread of sizes present in a polydisperse system. The extent to which fractionation takes place will be determined by the mobility of the particles at this volume fraction. Slow dynamics will prevent the system to fully fractionate on experimental timescales, resulting in phase behaviour that depends on the quenched polydispersity.

The remainder of this chapter is organised in the following way. In Section 3.2 we give simulation details and describe the order parameters we used to analyse the results, in Section 3.3 we discuss the results, and in Section 3.4 our conclusions are presented.

3.2 Computational methods

3.2.1 Simulation details

In our model, the particles interact through a pairwise-additive hard-core repulsive Yukawa (screened Coulomb) potential [15]:

$$\beta u_{ij}(r) = \begin{cases} \beta\epsilon_{ij}\,\dfrac{\exp\left[-\kappa(r-\sigma_{ij})\right]}{r/\sigma_{ij}} & r \geq \sigma_{ij} \\ \\ \infty & r < \sigma_{ij} \end{cases}, \tag{3.1}$$

with $\sigma_{ij} = (\sigma_i + \sigma_j)/2$ and the contact value of the potential between two colloids i and j:

$$\beta\epsilon_{ij} = \frac{Z_i Z_j}{(1+\kappa\sigma_i/2)(1+\kappa\sigma_j/2)}\,\frac{\lambda_\mathrm{B}}{\sigma_{ij}}\,, \tag{3.2}$$

where r is the centre-to-centre distance between particles i and j, Z_i (Z_j) and σ_i (σ_j) are the charge number and diameter of colloid i (j), $\beta = 1/(k_\mathrm{B}T)$, with k_B the Boltzmann constant, and T the absolute temperature. The Bjerrum length is given by

$$\lambda_\mathrm{B} = \frac{e^2}{4\pi\epsilon_\mathrm{r}\epsilon_0 k_\mathrm{B}T}\,, \tag{3.3}$$

with e the elementary charge, ϵ_r the relative dielectric constant of the solvent and ϵ_0 the dielectric permittivity of vacuum. The Bjerrum length represents the distance at which the electrostatic interaction energy between two monovalent ions is equal to the thermal energy $k_\mathrm{B}T$. The inverse Debye screening length is given by

$$\kappa = \sqrt{8\pi\lambda_\mathrm{B}c_\mathrm{s}}\,, \tag{3.4}$$

with c_s the concentration of the monovalent salt. The Debye screening length κ^{-1} indicates the thickness of the electrical double layer surrounding a colloidal particle and is a measure for the interaction range between two colloids. The electrostatic surface potential $\psi_{0,\,i}$ for an isolated particle i can be approximated at low $\psi_{0,\,i}$ by [12]

$$\beta e\psi_{0,\,i} = \frac{Z_i}{1+\kappa\sigma_i/2}\,\frac{2\lambda_\mathrm{B}}{\sigma_i}\,. \tag{3.5}$$

We took the charge number of the particles such that particles with a different size had the same surface potential. However, as mentioned before, the surface charge

was not a function of the volume fraction or distance between the particles. This means that the charge number of particle i with diameter σ_i is given by

$$Z_i = Z\left(\frac{\sigma_i}{\bar{\sigma}}\frac{1+\kappa\sigma_i/2}{1+\kappa\bar{\sigma}/2}\right), \tag{3.6}$$

where Z and $\bar{\sigma}$ are the charge number and diameter of a chosen reference particle. Inserting this expression for the charge number in Eq. 3.1 leads to the following expression for the potential:

$$\beta u_{ij}(r) = \begin{cases} \beta\bar{\epsilon}\,\dfrac{\sigma_i\sigma_j}{\bar{\sigma}}\,\dfrac{\exp\left[-\kappa(r-\sigma_{ij})\right]}{r} & r \geq \sigma_{ij} \\ \infty & r < \sigma_{ij} \end{cases}, \tag{3.7}$$

where $\beta\bar{\epsilon} = Z^2\lambda_\mathrm{B}/[(1+\kappa\bar{\sigma}/2)^2\,\bar{\sigma}]$ is the contact value of the potential for two reference particles with charge number Z and diameter $\bar{\sigma}$ (see Eq. 3.2). Combining Eqs. 3.2 and 3.5 yields the relation between ϵ_{ij} and the surface potentials $\psi_{0,\,i}$ and $\psi_{0,\,j}$:

$$\beta\epsilon_{ij} = \frac{(\beta e\psi_{0,\,i})(\beta e\psi_{0,\,j})}{4\lambda_\mathrm{B}}\,\frac{\sigma_i\sigma_j}{\sigma_{ij}}\,, \tag{3.8}$$

which simplifies for equally sized particles ($\sigma_i = \sigma_j = \bar{\sigma}$) with identical surface potentials ($\psi_{0,\,i} = \psi_{0,\,j} = \psi_0$) to

$$\beta\bar{\epsilon} = \frac{(\beta e\psi_0)^2}{4}\,\frac{\bar{\sigma}}{\lambda_\mathrm{B}}\,. \tag{3.9}$$

The particle diameters σ in our systems are distributed according to a log-normal distribution:

$$p(\sigma;\mu,\delta) = \frac{1}{\sigma\delta\sqrt{2\pi}}\,\exp\left[-\frac{(\ln\sigma-\mu)^2}{2\delta^2}\right], \tag{3.10}$$

where μ and δ are the mean and the standard deviation of the natural logarithm of variable σ (which is a continuous variable, contrary to σ_i above). The diameter of the above-mentioned reference particle ($\bar{\sigma}$) is chosen such that $\mu = \ln\bar{\sigma}$. The use of a log-normal distribution rather than a Gaussian distribution avoids the problem of having a finite probability for negative diameters. We define the polydispersity s as the ratio of the standard deviation and the mean of σ:

$$s \equiv \frac{\sqrt{\langle\sigma^2\rangle - \langle\sigma\rangle^2}}{\langle\sigma\rangle}\,. \tag{3.11}$$

The polydispersity can be written in terms of the log-normal distribution parameter δ:

$$s = \sqrt{e^{\delta^2} - 1}\,, \tag{3.12}$$

and for the values of δ that we use ($\delta \in [0.00, 0.15]$), s can be approximated by

$$s \approx \delta\,. \tag{3.13}$$

We performed NVT Monte Carlo simulations, keeping the number of particles N, the volume of the cubic box V and the absolute temperature T constant. The volume fraction η is given by

$$\eta = \frac{\pi}{6V} \sum_{i=1}^{N} \sigma_i^3\,, \tag{3.14}$$

where the sum runs over all particles N in the system and σ_i is the diameter of particle i. The initial configuration was either a face-centred-cubic (fcc; $N = 2048$) or body-centred-cubic (bcc; $N = 2000$) crystal configuration, chosen to match the stable crystalline phase of the monodisperse system at the volume fraction of the crystal-fluid transition, as determined from free energy calculations in Monte Carlo simulations [28]. Polydisperse initial configurations were made by placing N particles on a crystal lattice with diameters randomly assigned according to the aforementioned log-normal distribution. If overlap occurred each particle was assigned a new diameter. For each combination of $\beta\bar{\epsilon}$, $\kappa\bar{\sigma}$, η and s we made not more than 10^6 attempts at generating non-overlapping configurations. It should be noted that above a certain polydispersity this procedure does not result in non-overlapping initial configurations. We used two different typical contact values, $\beta\bar{\epsilon} = 20$ and 81 (corresponding to surface potentials $\beta e\psi_0 \approx 1$ and 2, assuming $\lambda_B/\bar{\sigma} = 0.01$), and several values of $\kappa\bar{\sigma}$ from the range 2.5–10. The pair potential was cut off at a distance of $4.10\,\bar{\sigma}$. We found no significant differences in our results for larger values of this cut-off distance. The maximum displacement of the particles was set to $0.1\,\bar{\sigma}$. Simulations were run for 2×10^4 Monte Carlo cycles, where one cycle means on average one displacement per particle. For each state point five independent runs were performed. After 2×10^4 Monte Carlo cycles we analysed the configurations by calculating various order parameters (see Section 3.2.2).

3.2.2 Order parameters

For each particle i we can define a set of $2l+1$ bond-orientational order parameters $q_{lm}(i)$:

$$q_{lm}(i) = \frac{1}{N_\mathrm{b}(i)} \sum_{j=1}^{N_\mathrm{b}(i)} Y_{lm}(\theta_{ij}, \phi_{ij}) \,, \tag{3.15}$$

where $N_\mathrm{b}(i)$ is the number of neighbours of particle i, θ_{ij} and ϕ_{ij} are the inclination and azimuth angles of the bond $\mathbf{r}_{ij} = \mathbf{r}_i - \mathbf{r}_j$ (where $\mathbf{r}_i$ ($\mathbf{r}_j$) denotes the position of particle i (j)) connecting the centres of particle i and its neighbour j, and $Y_{lm}(\theta_{ij}, \phi_{ij})$ are the spherical harmonics (with $m = -l, -l+1, \ldots, l-1, l$). The neighbours of particle i are defined as all particles within a certain cut-off distance r_c from particle i.

We used these sets of bond-orientational order parameters to calculate three different order parameters. The local bond-orientational order parameter $q_l(i)$ is calculated in the following way [34]:

$$q_l(i) = \sqrt{\frac{4\pi}{2l+1} \sum_{m=-l}^{l} |q_{lm}(i)|^2} \,, \tag{3.16}$$

where $q_{lm}(i)$ is defined in Eq. 3.15. We can average each of the members of the set from Eq. 3.15 over the central particle and its neighbours, to obtain for each particle i a set of *averaged* bond-orientational order parameters $\bar{q}_{lm}(i)$:

$$\bar{q}_{lm}(i) = \frac{1}{N_\mathrm{b}(i)+1} \sum_{j=0}^{N_\mathrm{b}(i)} q_{lm}(j) \,, \tag{3.17}$$

where the sum runs over all the neighbours of particle i plus the particle i itself. From these sets of averaged bond-orientational order parameters, we obtain an averaged local bond-orientational order parameter $\bar{q}_l(i)$ [35]:

$$\bar{q}_l(i) = \sqrt{\frac{4\pi}{2l+1} \sum_{m=-l}^{l} |\bar{q}_{lm}(i)|^2} \,. \tag{3.18}$$

Finally, the correlation between the sets of bond-orientational order parameters for each pair of neighbouring particles can be written as

$$c_l(ij) = \frac{\sum_{m=-l}^{l} q_{lm}(i) q^*_{lm}(j)}{\left(\sum_{m=-l}^{l} |q_{lm}(i)|^2 \right)^{1/2} \left(\sum_{m=-l}^{l} |q_{lm}(j)|^2 \right)^{1/2}} \,, \tag{3.19}$$

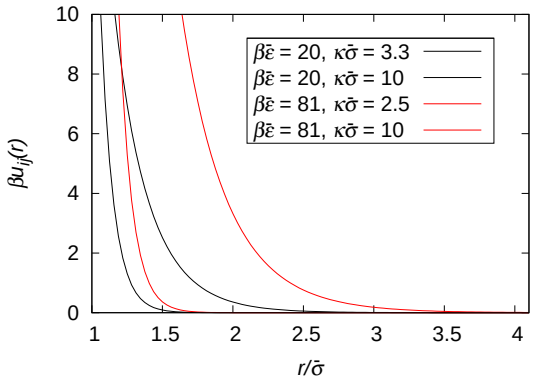

Figure 3.1: Pair potentials for two reference particles with diameter $\bar{\sigma}$ for four different combinations of Yukawa potential parameters $\beta\bar{\epsilon}$ and $\kappa\bar{\sigma}$.

where $q_{lm}(i)$ is defined in Eq. 3.15 and $q^*_{lm}(j)$ is the complex conjugate of $q_{lm}(j)$. Crystalline particles are defined as particles with more than a certain number n_c of connected neighbours, where a connected neighbour is a neighbour j to particle i for which $c_l(ij)$ exceeds a threshold value c_c [36]. For our analysis we chose $l = 6$, $r_c = 1.5\rho^{-1/3}$ (with $\rho = N/V$ the number density of the particles, and $\rho^{-1/3}$ the characteristic interparticle distance), $c_c = 0.6$ and $n_c = 8$. We used this order parameter to calculate the fraction of crystalline particles in the system (the crystalline fraction is 1.0 in a perfect bulk fcc or bcc crystal, and close to 0.0 in a fluid), and to calculate the average crystallinity of a particle during a part of the simulation, which is the fraction of time that the particle is crystalline during that part of the simulation.

In order to determine whether certain arrangements of particles were liquid or glassy we also looked at particle dynamics (as measured by particle diffusion), without taking interparticle hydrodynamic effects into account. The mean square displacement from the initial (ideal) lattice positions at a certain point τ in the simulation is given by:

$$\langle \Delta r(\tau)^2 \rangle = \frac{1}{N} \sum_{i=1}^{N} (\mathbf{r}_i(\tau) - \mathbf{r}_i(0))^2, \tag{3.20}$$

where $\mathbf{r}_i(\tau)$ is the position of particle i at time τ and $\mathbf{r}_i(0)$ the initial (ideal) lattice position of particle i.

3.3 Results and discussion

We studied the following combinations of the Yukawa potential parameters: for the weakly charged particles with reference contact value $\beta\bar{\epsilon} = 20$ we studied $\kappa\bar{\sigma}$ values in the range 3.3–10, corresponding to screening lengths $(\kappa\bar{\sigma})^{-1}$ in the range 0.30–0.10; for the more highly charged particles with $\beta\bar{\epsilon} = 81$ we studied $\kappa\bar{\sigma}$ values in the range 2.5–10, corresponding to screening lengths $(\kappa\bar{\sigma})^{-1}$ in the range 0.40–0.10. In Fig. 3.1 we plotted some of the pair potentials for two reference particles with diameter $\bar{\sigma}$. For each polydispersity we calculated the crystalline fraction and the mean square displacement from the initial lattice positions over a range of volume fractions. We found qualitatively different behaviour for the weakly and more highly charged particles; below we discuss the results for both.

3.3.1 Weakly charged particles

First we consider the case of more weakly charged particles ($\beta e\psi_0 \approx 1$). Despite their low surface potential, particles hardly ever come into contact with their hard cores, as the size of the particles makes that $\beta\bar{\epsilon} = 20$ (Eq. 3.9, with $\lambda_B/\bar{\sigma} = 0.01$). Fig. 3.2 presents the crystalline fraction versus volume fraction for $\kappa\bar{\sigma} = 3.3$, 4.0, 6.7 and 10. We started our simulation with a bcc phase for $\kappa\bar{\sigma} = 3.3$ and 4.0, while an fcc phase was used for $\kappa\bar{\sigma} = 6.7$ and 10, chosen to match the stable crystalline phase of the monodisperse system at the volume fraction of the crystal-fluid transition [28]. Due to hysteresis the crystal-fluid transition for the monodisperse system $\eta_{CF}(s = 0)$ was found at slightly lower volume fraction than in the equilibrium phase diagram, e.g. for $\kappa\bar{\sigma} = 3.3$ we find $\eta_{CF}(0) \approx 0.26$ versus $\eta_{CF}(0) \approx 0.28$ in the phase diagram obtained from free energy calculations using Monte Carlo simulations [28, 114]. Hysteresis was also found for the polydisperse systems with $\kappa\bar{\sigma} = 3.3$ and 10, when comparing to results on systems with very similar potential parameters from Ref. [114]. For systems with polydispersity above 0.10 (values tried were 0.13 and 0.15) it was not possible to obtain a fully crystalline starting configuration within a reasonable number of attempts. From the plots in Fig. 3.2 we see that the crystal-fluid transition shifts to higher volume fractions with increasing polydispersity. This shift is present for all $\kappa\bar{\sigma}$ values in the range 3.3–10, but the shift is larger if the potential is longer-range (smaller $\kappa\bar{\sigma}$ or larger screening length $(\kappa\bar{\sigma})^{-1}$). To illustrate this, we plotted in Fig. 3.3 the shift in volume fraction for four different $\kappa\bar{\sigma}$ values. The shift is defined as

$$\Delta\eta(s) = \eta_{CF}(s) - \eta_{CF}(0), \tag{3.21}$$

where $\eta_{CF}(s)$ and $\eta_{CF}(0)$ are the volume fraction of the crystal-fluid transition for polydispersity s and for the monodisperse system (with $s = 0$), respectively. We

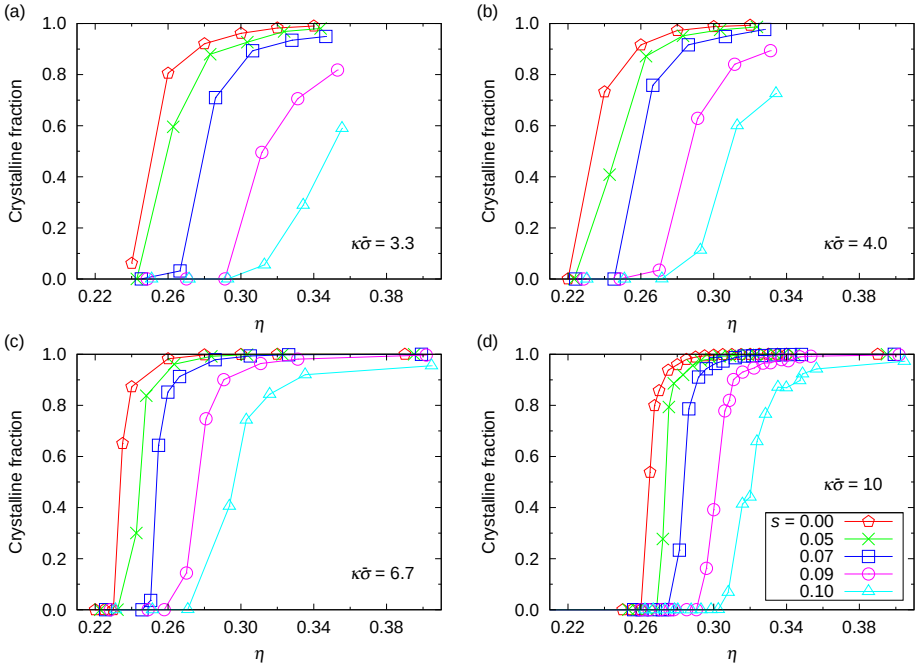

Figure 3.2: Crystalline fraction versus volume fraction η of a system of particles which interact through a hard-core repulsive Yukawa pair potential with reference contact value $\beta\bar{\epsilon} = 20$ and (a) $\kappa\bar{\sigma} = 3.3$, (b) 4.0, (c) 6.7, and (d) 10 after a simulation of 2×10^4 Monte Carlo cycles, starting from a bcc ($\kappa\bar{\sigma} = 3.3$ and 4.0) or fcc ($\kappa\bar{\sigma} = 6.7$ and 10) crystal structure, for different polydispersities s in the range 0.00–0.10 as labelled.

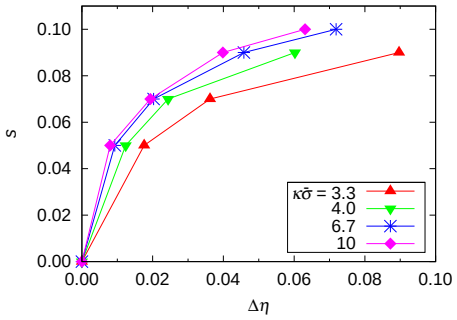

Figure 3.3: Shift in volume fraction of the crystal-fluid transition $\Delta\eta(s)$ (as defined in Eq. 3.21) with size polydispersity s of a system of hard-core repulsive Yukawa particles with reference contact value $\beta\bar{\epsilon} = 20$ and $\kappa\bar{\sigma} = 3.3$, 4.0, 6.7 and 10 as labelled.

took for $\eta_{\mathrm{CF}}(s)$ and $\eta_{\mathrm{CF}}(0)$ the values of the volume fraction at which the (interpolated) crystalline fraction equals 0.80. From Fig. 3.3 it is clear that the shift of the crystal-fluid transition with increasing polydispersity is larger for longer-range potentials. The initial crystal type (bcc or fcc) does not appear to qualitatively influence the shift. We assume that a volume fraction corresponding to a crystalline fraction of 0.80 lies in the coexistence gap and take it as a measure for the volume fraction at which the crystal-fluid transition would occur in quenched equilibrium where fractionation does not take place. We wish to remark here that different simulation techniques that allow for fractionation should be employed to determine the equilibrium phase behaviour of polydisperse systems (see e.g. Refs. [106, 107, 125, 126]). It is tempting to speculate that a longer-range potential gives rise to a larger effective polydispersity, which would explain the larger shift of the crystal-fluid volume fraction with polydispersity.

3.3.2 More highly charged particles

Fig. 3.4 shows the crystalline fraction versus volume fraction for more highly charged particles ($\beta e\psi_0 \approx 2$) with $\beta\bar{\epsilon} = 81$ and $\kappa\bar{\sigma} = 2.5$, 3.3, 6.7 and 10. We started our simulation with a bcc phase for $\kappa\bar{\sigma} = 2.5$ and 3.3, while an fcc phase was used for $\kappa\bar{\sigma} = 6.7$ and 10, chosen to match the stable crystalline phase of the monodisperse system at the volume fraction of the crystal-fluid transition [28]. Comparing these plots to Fig. 3.2 for $\beta\bar{\epsilon} = 20$, we see a much weaker shift in the crystal-fluid transition with increasing polydispersity. Up to $s = 0.10$ we hardly see a shift at all, while for higher polydispersities the shift, if present, is much smaller than in the case of weakly charged particles. For the weakly charged particles melting takes place at relatively high volume fraction; the characteristic interparticle distance at the crystal-fluid transition is thus smaller than for the more highly charged particles. It seems likely that for the case of weakly charged particles, the crystal lattice can therefore not accommodate an equally broad spread in sizes as for the case of more highly charged particles, which seems a possible reason for the larger shift of the crystal-fluid volume fraction for the case of weakly charged particles.

The crystal-fluid transition for $\beta\bar{\epsilon} = 81$ occurred at lower volume fractions than for $\beta\bar{\epsilon} = 20$, which allowed us to investigate higher polydispersities and higher volume fractions relative to the volume fraction of the monodisperse crystal-fluid transition. In this region we observed something not found for the more weakly charged systems: for $s = 0.13$ and 0.15 only parts of the system became disordered, while the remaining parts stayed crystalline. After running the simulations for 2×10^5 cycles (ten times the length of the initial run) the crystalline fraction for $s = 0.13$ was still at the same value, and the crystalline fraction for

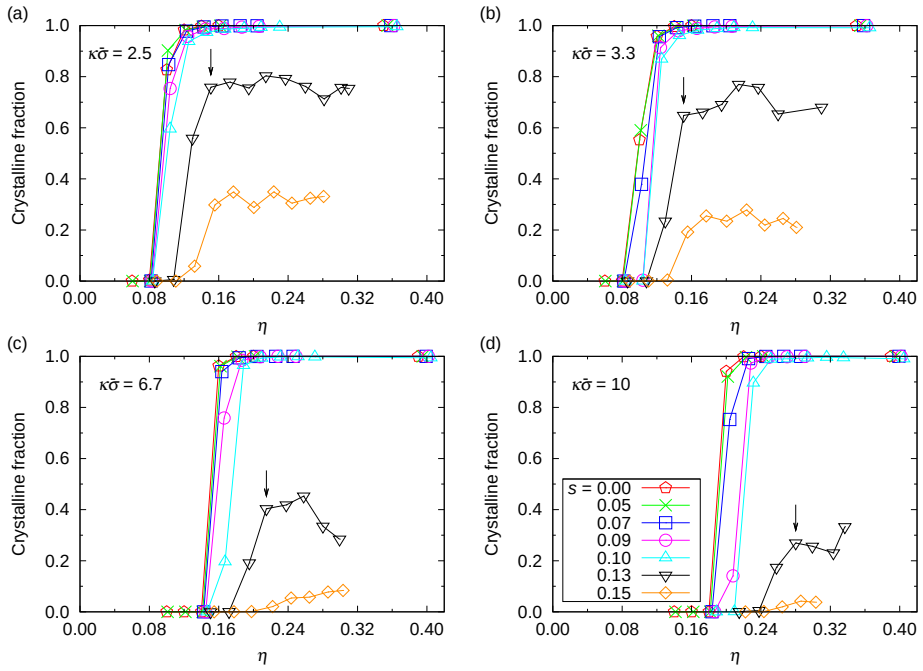

Figure 3.4: Crystalline fraction versus volume fraction η of a hard-core repulsive Yukawa system with reference contact value $\beta\bar{\epsilon} = 81$ and (a) $\kappa\bar{\sigma} = 2.5$, (b) 3.3, (c) 6.7, and (d) 10 after a simulation of 2×10^4 Monte Carlo cycles, starting from a bcc ($\kappa\bar{\sigma} = 2.5$ and 3.3) or fcc ($\kappa\bar{\sigma} = 6.7$ and 10) crystal structure, for different polydispersities s in the range 0.00–0.15 as labelled. The arrows indicate the edge of the plateau for $s = 0.13$ and may be used for comparison with Figs. 3.7 and 3.8.

$s = 0.15$ had only slightly decreased (for analysis confirming that the disordered parts did not display long-time self-diffusion and hence were not fluid, see below). The crystalline fraction at which the system seems to stabilise is lower for higher polydispersity (e.g. for $\kappa\bar{\sigma} = 2.5$ this crystalline fraction is ~ 0.80 for $s = 0.13$ and ~ 0.30 for $s = 0.15$), but is for a given polydispersity approximately the same over a whole range of volume fractions. For all other $\kappa\bar{\sigma}$ values we observed the same phenomenon, with the crystalline fraction at which the system stabilises decreasing with increasing $\kappa\bar{\sigma}$ to ~ 0.25 and ~ 0.05, respectively, for $s = 0.13$ and 0.15 (for $\kappa\bar{\sigma} = 10$).

We took a closer look at several of the configurations where the crystalline fraction reached a plateau for a range of volume fractions. Fig. 3.5 shows four times the same snapshot after 2×10^4 cycles of a configuration with $\beta\bar{\epsilon} = 81$, $\kappa\bar{\sigma} = 2.5$, $s = 0.15$ and $\eta = 0.20$. For Fig. 3.5a we calculated the crystallinity for each particle as described in Section 3.2 for a series of six configurations between 1.5×10^4 and 2×10^4 Monte Carlo cycles (crystallinity = 1 for a crystalline particle, 0 for a non-crystalline particle) and determined the average crystallinity; black particles have low crystallinity, while yellow (light grey) particles have high crystallinity. In Fig. 3.5b each particle's colour indicates for the configuration after 2×10^4 cycles whether its average local bond-orientational order parameter $\bar{q}_6$ is low (black) or high (yellow/light grey). In Fig. 3.5c we show the same, but for the non-averaged local bond-orientational order parameter q_6. In the fourth snapshot, Fig. 3.5d, a particle's colour is determined by the square of the displacement $\Delta r_i(\tau)^2 = (\mathbf{r}_i(\tau) - \mathbf{r}_i(0))^2$ from its ideal initial lattice position: small (black) or large (yellow/light grey).

From the average crystallinity of each particle (Fig. 3.5a) we see that in this snapshot, and also the other snapshots we looked at, the crystalline particles and non-crystalline particles are in different domains. We observed strong correlation between the average crystallinity and the average local order parameter $\bar{q}_6$ of each particle: Fig. 3.5b shows similar domains. A much weaker correlation is found between the average crystallinity and the non-averaged local bond-orientational order parameter q_6: there are large fluctuations in the value of q_6 within a domain (Fig. 3.5c). This means that an individual particle within an ordered domain does not necessarily have high q_6 itself. However, the probability of finding a particle with a high q_6 value is higher in a domain consisting of particles with high average crystallinity and high $\bar{q}_6$. The correlation between the square displacement $\Delta r_i(\tau)^2$ and average crystallinity is present, but also not very strong: the *mean* square displacement $\langle \Delta r(\tau)^2 \rangle$ (Eq. 3.20) is smaller in crystalline domains than non-crystalline domains, but we find large fluctuations in the square displacement $\Delta r_i(\tau)^2$ of individual particles within a domain.

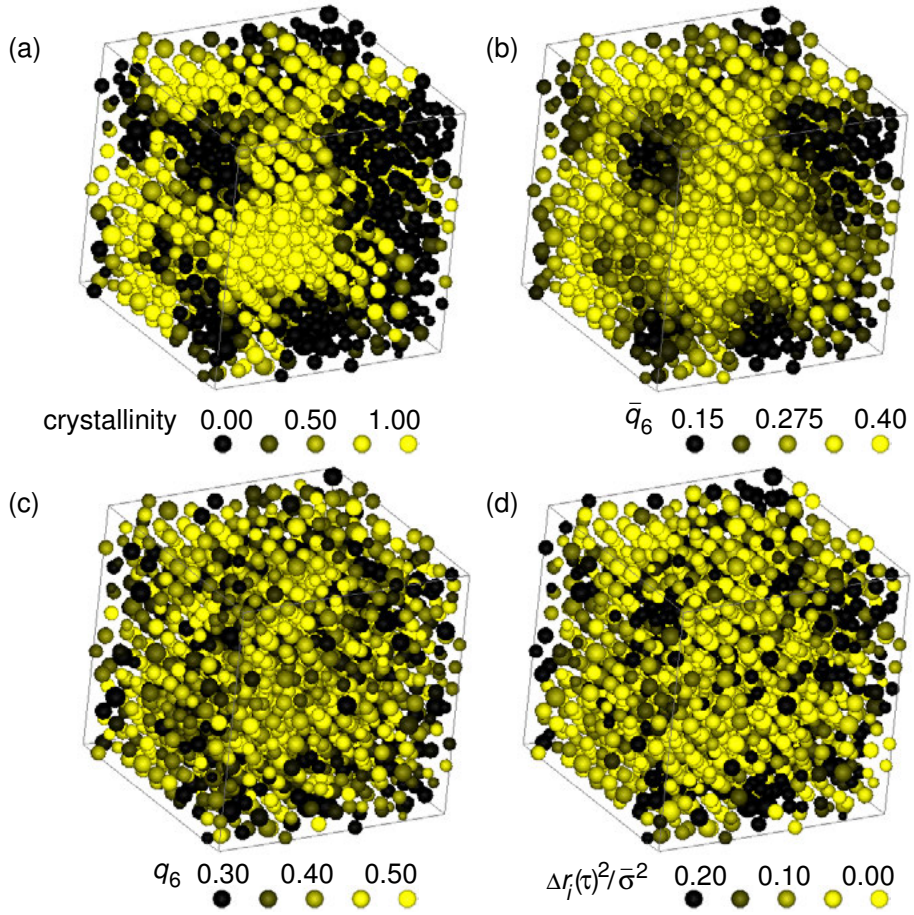

Figure 3.5: Snapshot after 2×10^4 Monte Carlo cycles of a hard-core repulsive Yukawa system with reference contact value $\beta\bar{\epsilon} = 81$, $\kappa\bar{\sigma} = 2.5$, $\eta = 0.20$ and $s = 0.15$. The colour of a particle indicates (a) the average crystallinity in a series of six configurations between 1.5×10^4 and 2×10^4 Monte Carlo cycles, (b) the average local bond-orientational order parameter $\bar{q}_6(i)$ (Eq. 3.18) after 2×10^4 MC cycles, (c) local bond-orientational order parameter $q_6(i)$ (Eq. 3.16) after 2×10^4 MC cycles, and (d) the square displacement from the particle's ideal lattice position $\Delta r_i(\tau)^2/\bar{\sigma}^2 = (\mathbf{r}_i(\tau) - \mathbf{r}_i(0))^2/\bar{\sigma}^2$ for $\tau = 2 \times 10^4$ Monte Carlo cycles.

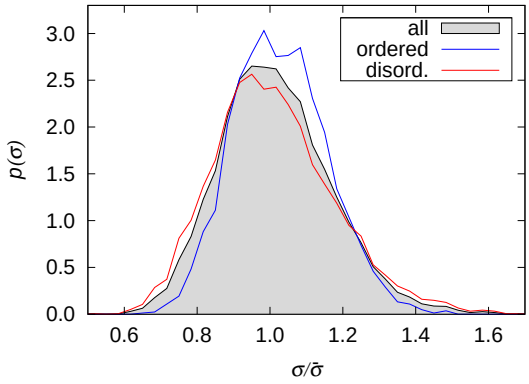

Figure 3.6: Normalised probability distribution functions $p(\sigma)$ of the particle diameter σ for $\beta\bar{\epsilon} = 81$, $\kappa\bar{\sigma} = 2.5$, $s = 0.15$ and $\eta = 0.20$ (55% most-disordered particles, 25% most-ordered particles). Filled grey curve: all particles, solid blue line: most-ordered particles (particles that are crystalline in at least five out of six configurations between 1.5×10^4 and 2×10^4 Monte Carlo cycles), dashed red line: most-disordered particles (particles that are crystalline in at most one out of six configurations between 1.5×10^4 and 2×10^4 Monte Carlo cycles).

3.3.3 Terminal polydispersity

We determined three size distributions for the final configuration of each run (after 2×10^4 MC cycles): one for the total system, a second for the most-disordered particles and a third for the most-ordered particles. Particles are labelled 'most-disordered' or 'most-ordered' by calculating the average crystallinity as described in Section 3.2. A most-disordered particle is crystalline in at most one out of six configurations and a most-ordered particle in at least five out of six configurations between 1.5×10^4 and 2×10^4 Monte Carlo cycles. The diameters were sampled from a continuous log-normal distribution; the calculated polydispersities for the sampled size distributions for the total system were very close to (within $\sim 1\%$ from) the polydispersity of the continuous distribution.

In Fig. 3.6 we plotted the three size distributions averaged over five simulations (for better statistics) with $\beta\bar{\epsilon} = 81$, $\kappa\bar{\sigma} = 2.5$, $s = 0.15$ and $\eta = 0.20$. The most-disordered size distribution (dashed red line) has a peak slightly, but significantly, more to the left (at smaller size) than the most-ordered size distribution (solid blue line). The most-disordered size distribution is also broader (has a higher polydispersity) than the most-ordered size distribution. Size distributions for configurations at different volume fractions show similar characteristics, as do the distributions for $s = 0.13$. Probably, local differences in polydispersity de-

termine whether the system stays crystalline or becomes disordered, with a higher local polydispersity destabilising the crystal structure and causing the system to become locally disordered.

Whether a configuration is disordered or crystalline depends on our definitions; however, it is clear that above a certain polydispersity a long-range ordered configuration or crystal cannot be formed regardless of the definition. If the system had sufficient time to fractionate, this is presumably what would eventually happen; however, given the slow dynamics in solid and glassy states, it is probably still useful to determine a value of the quenched polydispersity, i.e. with no fractionation taken into account, above which crystallisation does not occur. It should be kept in mind that the way the initial crystal configurations are chosen can also be regarded as selecting systems that are already slightly fractionated.

In a system with a higher polydispersity a larger part of the configuration is locally destabilised by fluctuations in the polydispersity, which explains why we find a larger fraction of disordered particles in the configurations with $s = 0.15$ than in the configurations with $s = 0.13$. As mentioned above, the crystalline fraction at which the system stabilises is, for a given polydispersity, approximately the same over a range of volume fractions. This can be explained by noting that the fraction of particles in the system that experiences the local polydispersity to be larger than some terminal polydispersity is independent of the volume fraction in the system, and assuming that significant re-entrant melting does not yet happen in this range of volume fractions.

To verify this explanation further, we calculated the polydispersity for the most-disordered and most-ordered particles in the systems with overall polydispersity $s = 0.13$ and 0.15. For the final configuration of each run (after 2×10^4 MC cycles) we calculated the polydispersity of the size distribution for the most-disordered particles and the polydispersity of the size distribution for the most-ordered particles. For each state point we averaged the obtained polydispersity values for the five independent runs. The results are shown in Fig. 3.7, where we plotted, for overall polydispersity $s = 0.13$, the polydispersity versus volume fraction in the total system, in the most-disordered parts and in the most-ordered parts of the system. The polydispersity in the most-ordered parts is significantly lower than in the most-disordered parts. We also note that the polydispersities in the most-ordered and most-disordered parts of the system are similar over the range of volume fractions for which the system seems to stabilise at a certain crystalline fraction (i.e. the range of volume fractions where the plot for $s = 0.13$ in Fig. 3.4 forms a plateau). For systems with $s = 0.15$ we find for the polydispersity of the most-ordered particles values similar to those for systems with $s = 0.13$.

The polydispersity of the most-ordered parts can be regarded as a measure for the terminal polydispersity, since the homogeneous crystal phase is no longer stable

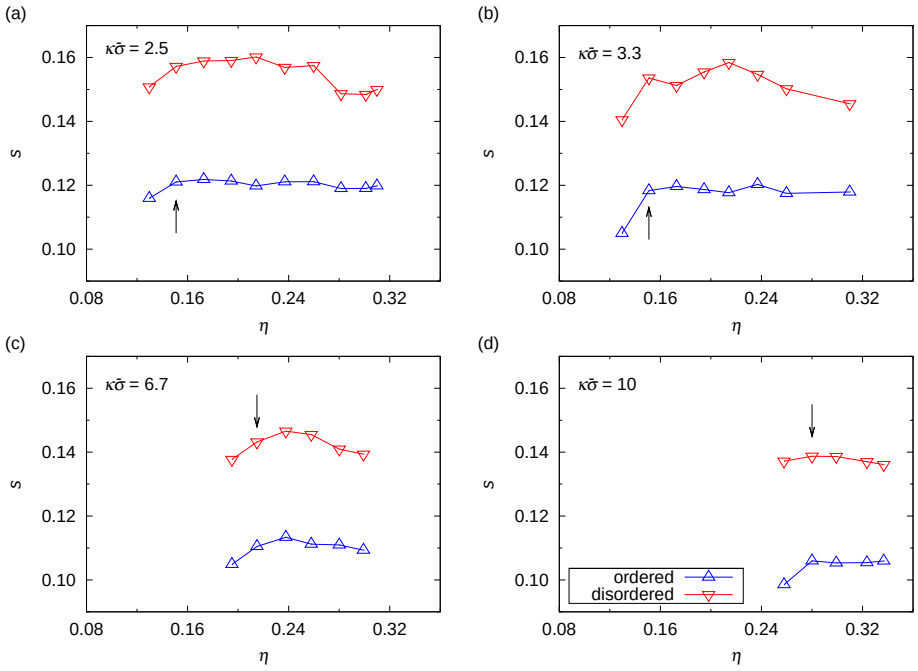

Figure 3.7: Polydispersity s versus volume fraction η of the most-ordered and most-disordered parts of hard-core repulsive Yukawa systems with reference contact value $\beta\bar{\epsilon} = 81$ and an overall polydispersity $s = 0.13$. For (a) $\kappa\bar{\sigma} = 2.5$, (b) 3.3, (c) 6.7, and (d) 10 after a simulation of 2×10^4 Monte Carlo cycles, starting from a bcc ($\kappa\bar{\sigma} = 2.5$ and 3.3) or fcc ($\kappa\bar{\sigma} = 6.7$ and 10) crystal structure. The arrows indicate the same state points as in Fig. 3.4.

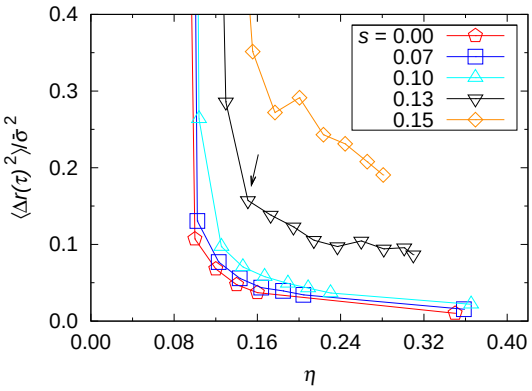

Figure 3.8: Mean square displacement $\langle \Delta r(\tau)^2 \rangle$ from the ideal lattice position (Eq. 3.20) versus volume fraction η for reference contact value $\beta\bar{\epsilon} = 81$ and $\kappa\bar{\sigma} = 2.5$ after a simulation of 2×10^4 Monte Carlo cycles, starting from a bcc crystal structure, for different polydispersities s in the range 0.00–0.15 as labelled. The arrow indicates the same state point as in Fig. 3.4a.

if the local polydispersity of the system is higher than this value. This terminal polydispersity decreases with increasing $\kappa\bar{\sigma}$ from ~ 0.12 for $\kappa\bar{\sigma} = 2.5$ to ~ 0.105 for $\kappa\bar{\sigma} = 10$. We expect particles with a longer-range potential ($\kappa\bar{\sigma} < 2.5$) to have an even higher terminal polydispersity. These values are in good agreement with the estimated terminal polydispersity ($0.125 < s < 0.13$ for parameters close to $\beta\bar{\epsilon} = 81$ and $\kappa\bar{\sigma} = 3.3$) as obtained from free energy calculations [114]. We take the trend observed for our values for the terminal polydispersity as an indication of what might be found for more reliable terminal polydispersities that could be measured using simulations that can achieve equilibrium [106].

3.3.4 Slow dynamics

Fig. 3.8 shows the mean square displacement from the initial ideal lattice positions versus volume fraction for $\beta\bar{\epsilon} = 81$, $\kappa\bar{\sigma} = 2.5$ and a range of polydispersities s. From this plot we see that in all systems that stay completely or partly crystalline, particles do not move over a distance larger than the typical particle diameter during the length of the simulation. This means that the dynamics in the system does not allow for the local polydispersity to change during the simulation and that the disordered parts in these systems are therefore essentially glassy, i.e. the particles display no long-time self-diffusion and are disordered.

This is illustrated further in Fig. 3.9, which shows the trajectories for 25 neighbouring particles during a simulation of 2×10^5 cycles for the state point with

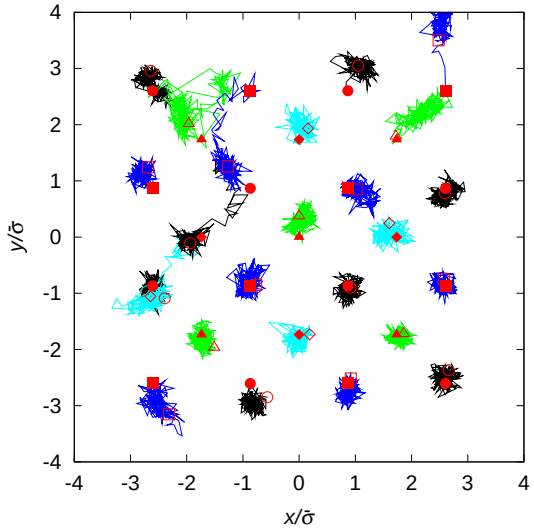

Figure 3.9: 2D projections of 3D trajectories during 2×10^5 Monte Carlo cycles of 25 particles from a configuration with $\beta\bar{\epsilon} = 81$, $\kappa\bar{\sigma} = 2.5$, $s = 0.15$ and $\eta = 0.20$. The initial configuration is a perfect bcc crystal; the initial positions of the particles are indicated by *filled* red symbols. Initially, the 25 particles are in two parallel {100} planes: 16 particles (filled red circles and filled red squares) in one plane occupy the corners of 3×3 unit cells, 9 particles (filled red triangles and filled red diamonds) in the second plane are in the centres of the unit cells. The end positions after 2×10^5 MC cycles are indicated by *open* red symbols (again circles, squares, triangles and diamonds; for each particle we used a symbol of the same shape to indicate the initial and end position). The trajectories are shown with four different colours (black, blue, green and cyan, which correspond to the circles, squares, triangles and diamonds, respectively).

$\beta\bar{\epsilon} = 81$, $\kappa\bar{\sigma} = 2.5$, $s = 0.15$ and $\eta = 0.20$. Most particles are confined to the cage formed by their neighbours during the length of the simulation, whereby some stay on their lattice position, while others are moved from their original position due to local distortion of the lattice. A few particles move from their lattice point and displace one of their neighbours, which then in turn hops to the lattice point of another neighbour or simply becomes part of a disordered part of the system. Most of these hopping movements and lattice distortions seem to occur early in the simulation, which is consistent with the observation that increasing the simulation length from 2×10^4 to 2×10^5 cycles does not significantly change the crystalline fraction in the system.

3.4 Conclusions

We investigated the effect of size polydispersity on the crystal-fluid transition in hard-core repulsive Yukawa systems. We observed a shift of the crystal-fluid transition of bulk crystals to higher volume fraction upon increasing the polydispersity. The shift was more pronounced for weakly charged particles ($\beta\bar{\epsilon} = 20$) compared to more highly charged particles ($\beta\bar{\epsilon} = 81$), and also for larger Debye screening length. For $\beta\bar{\epsilon} = 81$ at high polydispersities ($s \geq 0.13$; values used: $s = 0.13$ and 0.15) and high volume fractions, parts of the system that were initially crystalline became amorphous, indicating for these systems a terminal polydispersity beyond which the homogeneous crystal phase was no longer stable. For $\beta\bar{\epsilon} = 20$ we could not obtain crystalline systems for $s = 0.13$ and 0.15 for the volume fraction range of interest, providing a more direct indication that these values are above the terminal polydispersity.

We did not explicitly allow for size fractionation of the system other than the fractionation that 'naturally' occurred within the system, although it should be kept in mind that the way the initial crystal configurations are chosen can also be regarded as selecting systems that are already slightly fractionated. Due to the rather slow dynamics, we can only observe an onset to further fractionation because of the way the starting configurations were selected: the size distribution for 'most-ordered' particles was narrower than the overall (imposed) size distribution. Note that this is precisely the situation that prevails in experimental systems: as in our simulations, the size distribution imposed by the particle synthesis can only fractionate to the extent allowed for by the system's dynamics. In this sense, the simulations closely resemble the experimental situation.

Free energy calculations in which fractionation is included, could give a better insight in the equilibrium phases of the hard-core repulsive Yukawa system. Those have been performed for the case of hard spheres, but not yet for the longer-range Yukawa system, which is more difficult to probe due to its much larger parameter space.

4

Can we tune the fragility of long-range colloidal glasses with salt?

Using Monte Carlo simulations we investigated the slow dynamics close to the glass transition in suspensions of charged colloids, which interact through a hard-core repulsive Yukawa potential. We studied systems with a contact value of the Yukawa potential $\beta\bar{\epsilon} = 81$, corresponding to dimensionless surface potential $\beta e\psi_0 \approx 2$ (for $\lambda_B/\bar{\sigma} = 0.01$), and three different inverse screening lengths $\kappa\bar{\sigma} = 2.5$, 3.3 and 10. We calculated the self-intermediate scattering functions (SISFs) for three different values of the wave number q, one of which is close to the first peak of the structure factor. The structural relaxation times τ_α were obtained from stretched exponential fits. In addition, we calculated mean square displacements (MSDs), from which we determined the long-time self-diffusion coefficient D_L. The obtained values for τ_α at different q, and D_L^{-1}, could be well fitted both by a power law ($\tau_\alpha \propto D_L^{-1} \propto (\eta_c - \eta)^{-\gamma}$), predicted by mode-coupling theory (MCT), and by the Vogel-Fulcher-Tammann (VFT) equation ($\tau_\alpha \propto D_L^{-1} \propto \exp[B\eta/(\eta_0 - \eta)]$). The power-law fit from MCT yielded a glass transition volume fraction η_c that was much lower than the glass transition volume fraction η_0 from the VFT fit. The power-law exponent γ and VFT fit parameter B were larger for longer-range potentials. Furthermore, we found that the fragility of the glass-forming system decreased with increasing range of the potential (larger screening length κ^{-1}), suggesting that the fragility of experimental colloidal systems can be tuned by changing the salt concentration.

4.1 Introduction

Colloidal suspensions are excellent model systems for simple atomic or molecular systems. They display the same equilibrium phase behaviour, forming crystals and fluids, but also exhibit a glass transition [1]. Increasing the density of a colloidal fluid results in the slowing down of long-time particle diffusion and long-time structural relaxation, as measured by the long-time self-diffusion coefficient D_{L} and the long-time structural relaxation time τ_α, respectively. The volume fraction at which D_{L}^{-1} and τ_α diverge is the glass transition volume fraction [22]. An estimate for the glass transition volume fraction may be obtained by fitting measured values for τ_α or D_{L}^{-1} to an expression for τ_α or D_{L}^{-1} as a function of volume fraction, such as the power law predicted by mode-coupling theory (MCT) or the Vogel-Fulcher-Tammann (VFT) equation [127–129]. Alternatively, the glass transition volume fraction may be approximated by the volume fraction where τ_α or D_{L}^{-1} reach an arbitrarily chosen high value [22, 129]. The larger length scale and slower dynamics in colloidal systems compared to atomic or molecular systems, make it relatively easy to experimentally study the glass transition in these systems. Pusey and Van Megen found that effective hard spheres exhibit a glass transition at $\eta \approx 0.56$–0.58 [22]. The glass transition has also been found in charged colloidal systems that interact through longer-range repulsive potentials [30, 130, 131]. The glass transition volume fraction in these systems is much lower than for hard spheres, $\eta \approx 0.18$–0.22.

It has been argued that the (near) absence of hopping processes makes colloidal systems very suitable to test the idealised mode-coupling theory (MCT) [127, 132, 133]. Van Megen and Underwood performed dynamic light scattering (DLS) experiments on a system of poly(methyl methacrylate) PMMA colloids interacting through an effective hard-sphere potential and showed that the glass transition dynamics could be quantitatively described by MCT [127]. Agreement with MCT was also found in experiments on cross-linked polymer particles dispersed in a good solvent (microgels) [134] and charged colloidal systems [130, 131]. In more recent years, simulation studies suggested that the MCT divergence is avoided in colloidal systems [122, 135]. Experimental evidence was reported by Brambilla et al. [128], who performed DLS experiments and Monte Carlo (MC) simulations to probe the dynamics in concentrated suspensions of colloidal hard spheres over a very large range (seven decades) of structural relaxation times τ_α. They found that the volume-fraction dependence of τ_α is well described by MCT, but only up to $\eta_{\mathrm{c}} \approx 0.59$, the location of the glass transition volume fraction obtained from fits to MCT. At higher volume fractions τ_α increased more strongly and was found diverge at a volume fraction η_0. The authors conclude that η_{c} does not correspond

to a genuine colloidal glass transition, i.e. τ_α does not diverge at η_c, and that the MCT glass transition is possibly avoided in colloidal systems.

Several simulation studies address the use of MC simulations to investigate the dynamics in colloidal systems. MC algorithms which use only physically meaningful moves (i.e. particle displacement moves) are considered an easier-to-use substitute for Brownian dynamics (BD) simulations [123]. Given the diffusive nature of the dynamics in colloidal suspensions, algorithms simulating stochastic dynamics may be considered more appropriate to study the dynamics in colloidal systems than algorithms using deterministic Newtonian dynamics (ND) [124]. In order to use the standard MC algorithm to study dynamic processes, the MC timescale needs to be linked to the physical timescale [123, 124]. Sanz and Marenduzzo [123] reported for a hard-sphere-like and a repulsive Yukawa system that rescaling the MC time with the acceptance probability gives good agreement with BD results for the long-time self-diffusion coefficient. It should be remarked here that MC simulations do not take into account hydrodynamics and that the role of hydrodynamic interactions is different for molecular systems compared to colloidal systems.

Standard MC algorithms seem to be very suitable to study the slow dynamics close to the glass transition [122, 128]. Berthier and Kob [122] showed for a Lennard-Jones system that a standard MC algorithm is much more efficient than stochastic dynamics and BD algorithms, all three of which simulate stochastic dynamics. In addition, they showed that an optimal maximum displacement can be chosen (0.15 $\times$ particle diameter), which minimises the structural relaxation time. Furthermore, in this context we would like to mention again the work of Brambilla et al. [128], who investigated the slow dynamics in hard-sphere suspensions with DLS experiments and MC simulations and employed an MC algorithm with a fixed maximum displacement (0.1 $\times$ small particle diameter). Despite the fact that they used a single scaling factor for all volume fractions to map the MC timescale on the experimental timescale, they report good agreement between MC results and experimental DLS results: in both cases the same scaling behaviour of the structural relaxation time τ_α was found with virtually the same volume fraction at which τ_α diverged. Rescaling of MC time thus seems to be less important in the slow-dynamics regime close to the glass transition in order to reproduce the scaling behaviour of τ_α with volume fraction.

For molecular glasses, the concept of fragility is used to describe the nature of the divergence of the relaxation time with temperature, when approaching the glass transition. Close to the glass transition, the relaxation time in fragile glass-forming systems is very sensitive to changes in the temperature, whereas strong glass-formers are much less sensitive to a temperature change [136]. This is commonly shown by plotting the data on a rescaled Arrhenius plot, plotting the viscosity or

structural relaxation time on a logarithmic scale versus T_g/T (the inverse absolute temperature $1/T$ rescaled by glass transition temperature T_g); the slope of the curve at $T_g/T = 1$ is a measure for the fragility [136]. Mattsson et al. [129] reported on the fragility of a colloidal glass-forming system (microgels), for which the fragility was found to vary and was not restricted to the fragile behaviour seen in hard-sphere systems. They argue that the density for colloidal systems plays a role similar to $1/T$ in molecular systems, because the dependence of the long-time structural relaxation time in their systems can be described by the Vogel-Fulcher-Tammann (VFT) equation, but with $1/T$ replaced by the density; a physical interpretation is not given and seems not obvious. In analogy to the Arrhenius plot for molecular glass-formers, the authors plotted their data on a semilogarithmic plot with the structural relaxation time on a logarithmic scale versus the system's density, rescaled by a glass transition density; the slope of the curve at the glass transition density was taken as a measure for the fragility (see Ref. [137] for a recent discussion of the interpretation of this fragility). Using microgel suspensions of varying elasticity, they showed that softer particles were stronger glass-formers than more rigid particles [129].

In this chapter we studied the slow dynamics in systems interacting through a hard-core repulsive Yukawa potential. The range of the potential in these systems is controlled by the Debye screening length κ^{-1}, which can be varied experimentally by adjusting the salt concentration [39]. We performed Monte Carlo simulations on systems with a contact value of the Yukawa potential $\beta\bar{\epsilon}$ corresponding to a dimensionless surface potential $\beta e\psi_0 \approx 2$, a value which is experimentally relevant [39]. To address the dynamics in these systems, we calculated self-intermediate scattering functions and the mean square displacement.

We show that the obtained relaxation times τ_α and self-diffusion coefficients D_L could be fitted with a power law ($\tau_\alpha \propto D_L^{-1} \propto (\eta_c - \eta)^{-\gamma}$), as predicted by mode-coupling theory (MCT) [138]. The fits provided us with an exponent γ and a glass transition volume fraction η_c. In addition, τ_α and D_L could be fitted with the Vogel-Fulcher-Tammann (VFT) equation, from which we obtained a higher glass transition volume fraction η_0. Our results indicated that the systems with longer-range potentials also were stronger glass-formers. This suggests the possibility to adjust the fragility of experimentally obtained colloidal glasses by changing the salt concentration.

The remainder of this chapter is organised as follows. In Section 4.2 we describe the simulation details and data analysis. In Section 4.3 we report and discuss the results. Finally, in Section 4.4 we present the conclusions and outlook.

4.2 Computational methods

4.2.1 Simulation details

We used the same model as in Chapter 3 (Section 3.2.1), in which the particles interact through a hard-core repulsive Yukawa potential with a fixed contact value of the potential.

We performed NVT Monte Carlo simulations, keeping the number of particles $N = 2000$, the volume of the cubic box V and the absolute temperature T constant. A polydispersity of $s = 0.13$ was used to prevent crystallisation. Polydisperse initial configurations were obtained by placing N particles at random positions in the box and subsequently assigning diameters randomly according to a log-normal distribution (see Chapter 3). If overlap occurred each particle was assigned a new diameter. We made not more than 10^6 attempts to generate non-overlapping configurations. It should be noted that above a certain polydispersity this procedure does not result in non-overlapping initial configurations. We used a contact value of $\beta\bar{\epsilon} = 81$, which corresponds to an experimentally relevant surface potential $\beta e\psi_0 \approx 2$ (for $\lambda_B/\bar{\sigma} = 0.01$), and three values of $\kappa\bar{\sigma}$ (2.5, 3.3 and 10). The pair potential was taken to be pairwise additive and we used a cut-off of $4.10\,\bar{\sigma}$. In Chapter 3 we found no significant differences in our results for larger values of this cut-off distance. The maximum displacement of the particles was set to $0.1\,\bar{\sigma}$. We performed mostly long simulation runs of 2×10^6 Monte Carlo cycles (MC cycles) and sometimes for the lower volume fractions short runs of 5×10^4 MC cycles, where one MC cycle means on average one displacement per particle. For each state point results were averaged over five independent runs.

4.2.2 Data analysis

Self-intermediate scattering function

To measure structural relaxations, we calculated the self-part of the intermediate scattering function (or self-intermediate scattering function; SISF), given by [122, 128]

$$F_s(q,t) = \left\langle \frac{1}{N} \sum_{i=1}^{N} \exp[i\mathbf{q} \cdot (\mathbf{r}_i(t) - \mathbf{r}_i(0))] \right\rangle, \tag{4.1}$$

where $\mathbf{q}$ is the wave vector, with absolute value $q = |\mathbf{q}|$ (the wave number), and $\mathbf{r}_i(t)$ the position of particle i at time t (in units of MC cycles). The sum runs over all particles N in the system. The angular brackets indicate an ensemble average.

The total length of the simulation run (2×10^6 and 5×10^4 MC cycles for the long and short runs, respectively) was in each case ten times the length of the

time range for which the SISF was evaluated (2×10^5 and 5×10^3 MC cycles, respectively). The equilibration time was 1×10^5 MC cycles for the long MC runs (on the same order as the largest τ_α) and 1×10^4 MC cycles for the short MC runs. The SISF was averaged over the remaining part of the run.

We used a reduced wave number $qa = 7.0$, close to the location of the first peak of the structure factor, with $a = \rho^{-1/3}$ the characteristic distance between the particles and $\rho = N/V$ the particle number density. To compare the effect of the chosen qa value, we also calculated $F_\mathrm{s}(q,t)$ for slightly higher values $qa = 8.0$ and $qa = 9.0$.

Mean square displacement

We calculated the mean square displacement (MSD) of the particles, given by [122]

$$\frac{\Delta^2 r(t)}{\bar{\sigma}^2} = \frac{1}{\bar{\sigma}^2}\left\langle \frac{1}{N}\sum_{i=1}^{N} |\mathbf{r}_i(t) - \mathbf{r}_i(0)|^2 \right\rangle, \tag{4.2}$$

where $\mathbf{r}_i(t)$ is the position of particle i at time t (in units of MC cycles). The sum runs over all particles N in the system. The angular brackets indicate an ensemble average. The MSD was averaged over the same part of the runs as the SISF (see above).

Structural relaxation time from SISF

The long-time decay of the SISF was fitted with a stretched exponential function (Kohlrausch function) [136]:

$$F_\mathrm{s}(q,t) = A\exp[-(t/\tau)^\beta]\,, \tag{4.3}$$

with fit parameters τ (the relaxation time), β (the stretching exponent) and A (the plateau value prior to decay). The average structural relaxation time τ_α was calculated through [129]

$$\tau_\alpha = \frac{\tau}{\beta}\Gamma\left(1/\beta\right)\,, \tag{4.4}$$

where Γ is the gamma-function.

Long-time self-diffusion coefficient from MSD

The long-time self-diffusion of the MSD was fitted with

$$\frac{\Delta^2 r(t)}{\bar{\sigma}^2} = 6D_\mathrm{L}t\,, \tag{4.5}$$

with fit parameter D_{L} (the long-time self-diffusion coefficient). For the long MC runs we fitted the last 1×10^4 cycles of the range for which the MSD was calculated; for the short runs we fitted the last 5×10^2 cycles of the MSD-range.

Glass transition volume fraction

The relaxation times τ_α for three different qa values, and the self-diffusion coefficient D_{L}, were fitted with

$$\tau_\alpha \propto D_{\mathrm{L}}^{-1} \propto (\eta_{\mathrm{c}} - \eta)^{-\gamma}\,, \tag{4.6}$$

with fit parameters γ and η_{c} (the volume fraction where τ_α or D_{L}^{-1} diverges, or the glass transition volume fraction).

In addition, τ_α and D_{L} were fitted with the Vogel-Fulcher-Tammann (VFT) equation:

$$\tau_\alpha \propto D_{\mathrm{L}}^{-1} \propto \exp\left[\frac{B\eta}{\eta_0 - \eta}\right], \tag{4.7}$$

with fit parameters B and η_0 (the volume fraction where τ_α or D_{L}^{-1} diverges, or the glass transition volume fraction). This VFT equation for colloidal systems is obtained from the VFT equation for molecular systems [136] by replacing T with $1/\eta$ [129]. Replacing T with $1/\eta$ in the VFT equation for molecular systems is not obvious, but nonetheless yields an equation that provides a good description of the dependence of τ_α on η (see e.g. Refs. [129] or [128] for a similar expression).

Crystalline fraction

The crystalline fraction was calculated according to the method described in Chapter 3 (Section 3.2.2), which makes use of correlations between bond-orientational order parameters.

4.3 Results and discussion

4.3.1 Self-intermediate scattering functions

Figs. 4.1a–c show the SISFs for three systems with $\beta\bar{\epsilon} = 81$ and $\kappa\bar{\sigma} = 2.5$, 3.3 and 10, calculated for $qa = 7.0$ for various volume fractions η. In all cases we observe two indications of an approach towards glassy behaviour: the development of a plateau at higher volume fractions and a two-step decay of the SISF [133, 139]. The first decay, from unity to the plateau value, known as the β-relaxation, is commonly associated with the motion of the particles within a cage formed by

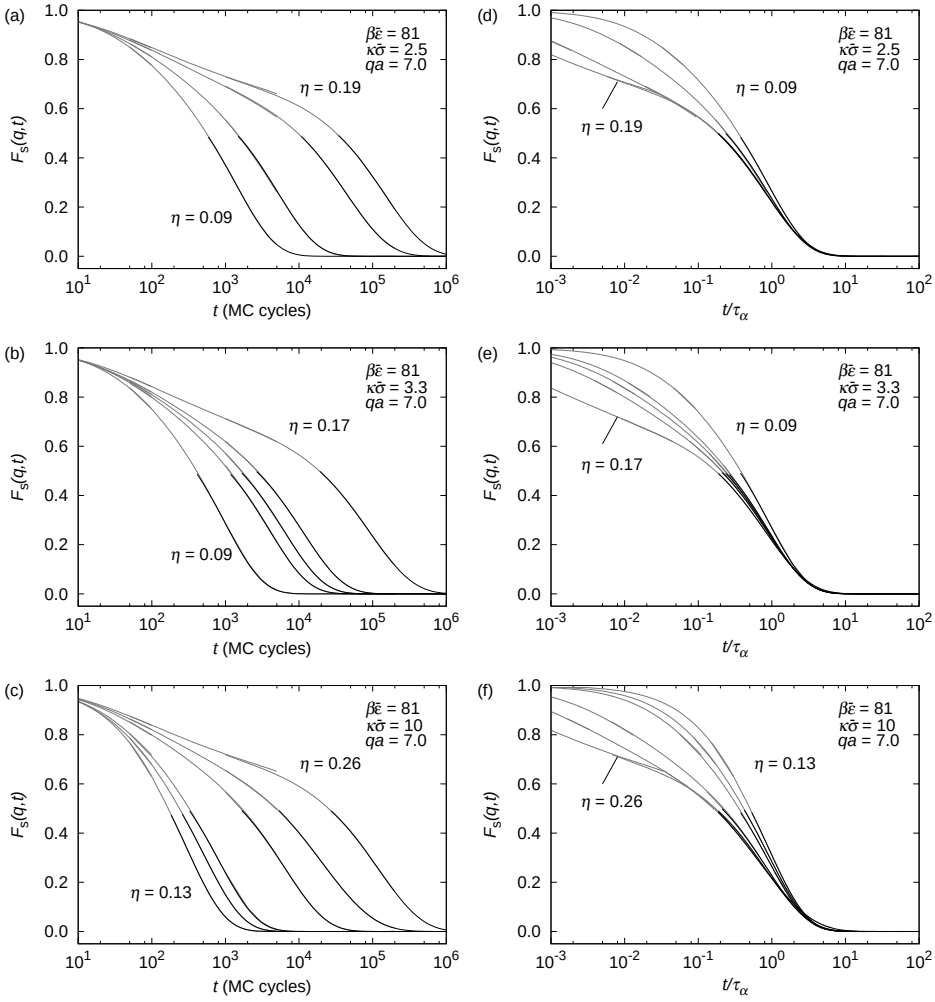

Figure 4.1: Self-intermediate scattering functions $F_\mathrm{s}(q,t)$ with $qa = 7.0$ (Eq. 4.1) for three different systems with $\beta\bar{\epsilon} = 81$ and (a) $\kappa\bar{\sigma} = 2.5$ ($\eta = 0.09$, 0.13, 0.17, 0.19), (b) $\kappa\bar{\sigma} = 3.3$ ($\eta = 0.09$, 0.13, 0.14, 0.15, 0.17) and (c) $\kappa\bar{\sigma} = 10$ ($\eta = 0.13$, 0.17, 0.19, 0.24, 0.25, 0.26). The black dashed lines are stretched exponential fits (Eq. 4.3) of the long-time decay of $F_\mathrm{s}(q,t)$. (d)–(f) show the same data scaled with the structural relaxation time τ_α obtained from the stretched exponential fit (Eqs. 4.3 and 4.4).

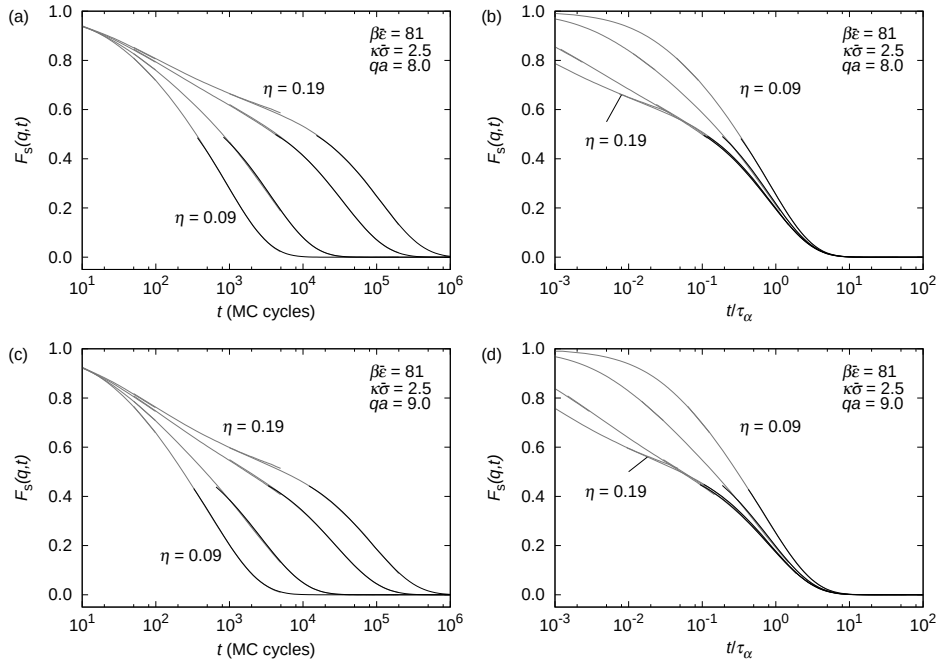

Figure 4.2: Same as Figs. 4.1a and d, but with $qa = 8.0$ and $qa = 9.0$.

their nearest neighbours. The second decay, from the plateau value to zero, is called the α-relaxation, and is caused by particles escaping from their cage [139].

The long-time decay of the SISFs could be well fitted with a stretched exponential function (Eq. 4.3) with fit parameters τ (the relaxation time), β (the stretching exponent) and A (the plateau value prior to decay). The average structural relaxation time τ_α was calculated from Eq. 4.4. Both A and β increased for smaller η, i.e. the decay increasingly resembled a single-exponential decay.

Figs. 4.1d–f show the same SISFs as in Figs. 4.1a–c plotted versus rescaled time t/τ_α. In each panel, the long-time part of the curves scale quite well. The plots give an indication for the colloidal analogue of the time-temperature superposition principle [133, 136, 140]. For smaller η overlap is obtained over a shorter rescaled time range, more towards the end of the curve.

To investigate the effect of qa on the relaxation behaviour, we calculated the SISFs for two additional qa values ($qa = 8.0$ and 9.0). Figs. 4.2a and c show the SISFs for the system with $\beta\bar{\epsilon} = 81$ and $\kappa\bar{\sigma} = 2.5$, calculated for $qa = 8.0$ and 9.0, respectively; Figs. 4.2b and d show the corresponding rescaled SISFs. For all $\kappa\bar{\sigma}$, the results with $qa = 8.0$ and 9.0 were qualitatively the same as the results with $qa = 7.0$. The difference was mainly in the relaxation time τ_α and plateau value A of the stretched exponential fit to the SISFs, both of which decreased with increasing qa.

4.3.2 Mean square displacement

Figs. 4.3a–c show the MSD for three systems with $\beta\bar{\epsilon} = 81$ and $\kappa\bar{\sigma} = 2.5$, 3.3 and 10 for the same values of η as in Fig. 4.1. In all cases a slowing down is observed with increasing volume fraction. The black dashed line indicates a slope of unity.

For two of the lowest η for which we performed long MC runs of 2×10^6 MC cycles, namely $\eta = 0.09$ for $\kappa\bar{\sigma} = 3.3$ and $\eta = 0.19$ for $\kappa\bar{\sigma} = 10$, the long-time part ($t = 1 \times 10^3$–2×10^5) does not overlap with the intermediate-time part ($t = 5 \times 10^1$–5×10^3) of the MSD. The intermediate-time part, which was averaged over configurations closer to the end of the simulation run, lies below the long-time part. This indicates that the translational motion of the particles later in the simulation run was smaller than earlier in the run. It might be that size segregation was taking place, and that the motion of particles decreased as particles found a more favourable local environment. This might eventually lead to crystallisation. Therefore, we checked the crystalline fraction f_X in the system at different stages of the simulation run (after 1×10^4, 5×10^4 and (for the long runs) 2×10^6 MC cycles), and found it to be always below 0.01, and mostly below 0.005. We did not find a systematic increase of the crystalline fraction in time, which indicates that no extensive crystallisation took place. However,

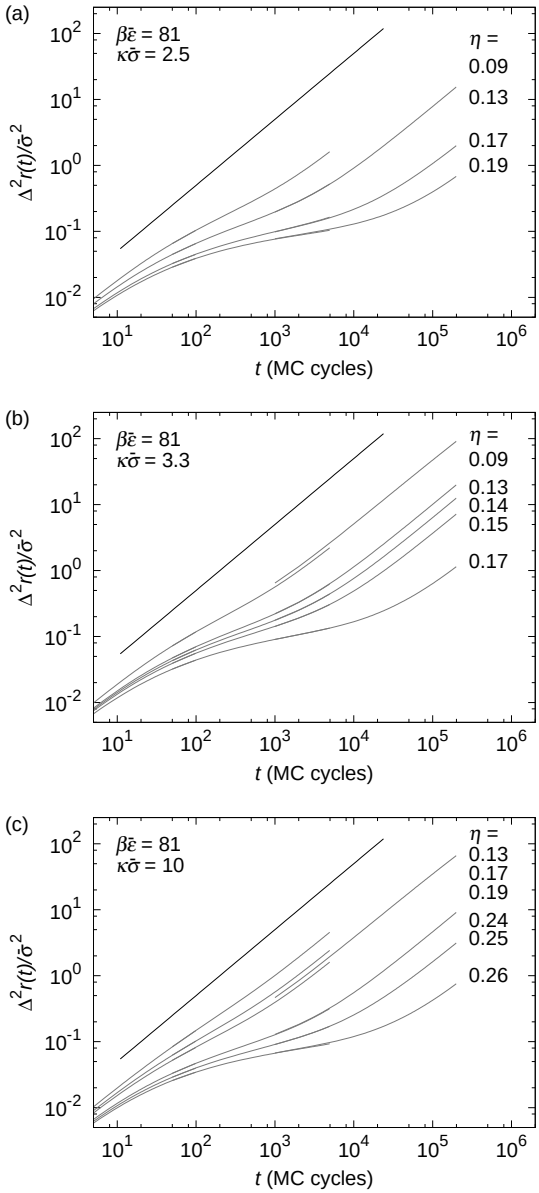

Figure 4.3: Mean square displacement $\Delta^2 r(t)$ (Eq. 4.2) for three different systems with $\beta\bar{\epsilon} = 81$ and (a) $\kappa\bar{\sigma} = 2.5$, (b) $\kappa\bar{\sigma} = 3.3$ and (c) $\kappa\bar{\sigma} = 10$. In three cases short simulation runs were performed and therefore the curves span a shorter t range, namely in (a) for $\eta = 0.09$ and in (c) for $\eta = 0.13$ and 0.17. The black dashed lines have a slope of unity.

Table 4.1: Fit parameters from power-law and VFT fits for the three systems used in this work, each with contact value of the pair potential $\beta\bar{\epsilon} = 81$, but with a different inverse screening length $\kappa\bar{\sigma}$. We report: (i) the exponent γ from a fit with the power law in Eq. 4.6; (ii) the corresponding glass transition volume fraction η_c at which τ_α and D_L^{-1} diverge; (iii) the parameter B from a fit with the VFT equation in Eq. 4.7; (iv) the corresponding glass transition volume fraction η_0 at which τ_α and D_L^{-1} diverge; and (v) the freezing volume fraction η_f for the monodisperse system from Ref. [28] with the corresponding stable crystal structure (body-centred-cubic (bcc) or face-centred-cubic (fcc)).

$\beta\bar{\epsilon}$	$\kappa\bar{\sigma}$	γ	η_c	B	η_0	η_f
81	2.5	5.2 ± 0.6	0.26 ± 0.01	6.1 ± 0.9	0.37 ± 0.02	0.10 (bcc)
81	3.3	2.77 ± 0.06	0.1927 ± 0.0008	2.3 ± 0.1	0.240 ± 0.002	0.11 (bcc)
81	10	2.1 ± 0.1	0.265 ± 0.001	0.88 ± 0.05	0.291 ± 0.002	0.21 (fcc)

this does not exclude size segregation or ordering of the particles more subtle than crystallisation. We observed that the very small but non-zero crystalline fraction ($f_X < 0.01$) appeared above the monodisperse crystal-fluid transition η_f (see Table 4.1), whereas below η_f, f_X was almost strictly zero. This suggests that local variations in polydispersity enable a small degree of crystallisation in some places, as we saw in Chapter 3. The mismatch of the two parts of the MSD curve is absent for higher η. Possibly, here the presence of crystalline particles had no visible effect on the MSD curve, as the long-time self-diffusion coefficient is smaller at higher η. Further research is needed to find the cause of the mismatch. We believe that the slight mismatch has no significant effect on the analysis below.

4.3.3 Glass transition

The SISFs were fitted with stretched exponential functions (Eq. 4.3), from which we obtained a value for the long-time relaxation time τ_α (Eq. 4.4). The long-time diffusive part of the MSD was fitted with a linear function (Eq. 4.5), from which we obtained a value for the long-time self-diffusion coefficient D_L. For each of the three $\kappa\bar{\sigma}$ values we were unable to determine D_L from the MSD for the system with the highest volume fraction (i.e. $\eta = 0.19$, 0.17 and 0.26 for $\kappa\bar{\sigma} = 2.5$, 3.3 and 10, respectively), because the long-time diffusive part was not reached within the t range for which the MSD was calculated.

We fitted τ_α and D_L according to the power law in Eq. 4.6 with fit parameters γ and η_c. We also fitted τ_α and D_L according to the VFT equation (Eq. 4.7) with fit parameters B and η_0. The values for the three τ_α values (at $qa = 7.0$, 8.0 and 9.0) and D_L for each system could be well fitted with a single set of fit parameters

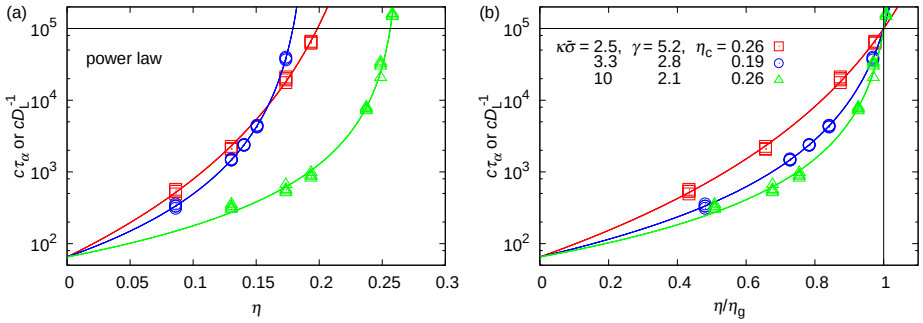

Figure 4.4: (a) Plot of $c\tau_\alpha$ (corresponding to $qa = 7.0$, 8.0 and 9.0) and cD_{L}^{-1} versus η for three different systems with $\beta\bar{\epsilon} = 81$ and with $\kappa\bar{\sigma} = 2.5$, 3.3 and 10 (open symbols). (b) The same data depicted as $c\tau_\alpha$ versus η/η_{g} with $\eta_{\mathrm{g}} \equiv \eta(c\tau_\alpha = 10^5)$ the volume fraction above which the rescaled relaxation time is no longer accessible. The solid lines are given by fits to the power law in Eq. 4.6. The constants c rescale the fits in the limit $\eta = 0$ on the fit for $c\tau_\alpha$ with $qa = 7.0$ and $\kappa\bar{\sigma} = 10$; data points have been rescaled by the same c as the corresponding fit. The unit of time is MC cycles.

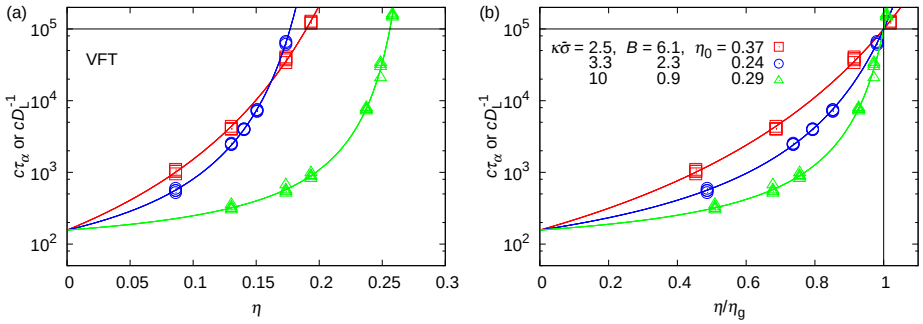

Figure 4.5: The same data as Fig. 4.4, but for fits with the VFT equation (Eq. 4.7). (a) Plot of $c\tau_\alpha$ (corresponding to $qa = 7.0$, 8.0 and 9.0) and cD_{L}^{-1} versus η for three different systems with $\beta\bar{\epsilon} = 81$ and with $\kappa\bar{\sigma} = 2.5$, 3.3 and 10 (open symbols). (b) The same data depicted as $c\tau_\alpha$ versus η/η_{g} with $\eta_{\mathrm{g}} \equiv \eta(c\tau_\alpha = 10^5)$ the volume fraction above which the rescaled relaxation time is no longer accessible. The solid lines are given by fits to the VFT equation in Eq. 4.7. The constants c rescale the fits in the limit $\eta = 0$ on the fit for $c\tau_\alpha$ with $qa = 7.0$ and $\kappa\bar{\sigma} = 10$; data points have been rescaled by the same c as the corresponding fit. The unit of time is MC cycles.

γ and η_c, and B and η_0. The proportionality constants depended on the quantity that was fitted. In Table 4.1 we report for each system the fit parameters γ, η_c, B and η_0. Figs. 4.4a and 4.5a show the corresponding fits on a semilogarithmic plot. The fits and data points for τ_α and D_L^{-1} have been rescaled by constants c in such a way that in the limit $\eta = 0$ the curves fall onto the fit for τ_α with $qa = 7.0$ and $\kappa\bar{\sigma} = 10$.

We see that the data are well fitted both by the power law (Eq. 4.6; Fig. 4.4a) and the VFT equation (Eq. 4.7; Fig. 4.5a). For the data with $\kappa\bar{\sigma} = 10$ the VFT equation (Eq. 4.7) seems to give a slightly better fit. The glass transition volume fractions obtained from the power-law fit (η_c) are much lower than those obtained from the VFT fit (η_0). A similar observation was made in Ref. [128] in hard-sphere systems for fits with the same power law and a slightly modified VFT equation. We do not have data above η_c and therefore we do not know if the divergence at η_c is avoided, as was found for hard spheres in Ref. [128].

In Table 4.1 we also give the freezing volume fraction η_f for the monodisperse system and the corresponding stable crystal structure (body-centred-cubic (bcc) or face-centred-cubic (fcc)), obtained from Ref. [28]. For our polydisperse systems, the freezing volume fraction is expected to be somewhat higher (see Chapter 3). We see that $\eta_0 > \eta_c > \eta_f$, or that the glass transition was located in the part of the phase diagram where the crystal is stable. The ratio η_0/η_f or η_c/η_f is smaller for shorter-range potentials. In accordance with this trend, the ratio η_c/η_f for hard spheres ($\eta_c = 0.59$, $\eta_f = 0.55$ [128]) is indeed smaller than for our system with the shortest-range potential ($\kappa\bar{\sigma} = 10$). We note that while η_f decreases monotonically with increasing range of the potential, η_c and η_0 do not.

Both γ and B increased with increasing range of the potential (decreasing $\kappa\bar{\sigma}$). The lowest value of γ seems on the low side compared to the value for hard-sphere systems, $\gamma \approx 2.6$ [128, 141], as it does not follow the trend of increasing γ with increasing range of the potential. In Ref. [138] it is pointed out that fitting Eq. 4.6 with both η_c and γ as fit parameters cannot be guaranteed to give the correct result, since deviations from Eq. 4.6 are expected for low and high η. The values for η_c and γ in Table 4.1 should therefore be regarded with caution. Unfortunately, we did not have a sufficient number of data points to test whether a different fit range would yield different values of γ and η_c. Comparison with a theoretical prediction from MCT for our systems could be helpful.

4.3.4 Fragility

To reveal differences in fragility between the systems, it is instructive to rescale the plots in Figs. 4.4a and 4.5a with η_g (or T_g for molecular glass-formers), where the volume fraction η_g, defined as $\eta(c\tau_\alpha = 10^5)$, is the volume fraction above which

the rescaled relaxation time is no longer accessible in experiments and simulations [129, 136, 142]. Figs. 4.4b and 4.5b show the same data as Figs. 4.4a and 4.5a, but with the volume fraction rescaled as η/η_g.

The slope of the $c\tau_\alpha$-versus-η/η_g curve at $\eta = \eta_g$ is a measure for the fragility of the glass-forming system [129, 136, 142]. Systems that show a gradual increase of τ_α on approach to η_g (small slope) are called strong glass-formers, while systems that exhibit a rapid increase of τ_α on approach to η_g (large slope) are called fragile glass-formers. For the VFT equation (Eq. 4.7) this slope is determined by B, with smaller B yielding a larger slope [129, 136, 142]. For our systems the slope at $\eta = \eta_g$ increases with increasing range of the potential, which indicates that longer-range systems are stronger glass-formers. This resembles the results in Ref. [129], where it was found that suspensions of softer microgel particles resulted in stronger glass-formers than suspensions of more rigid particles. However, we emphasise that the interparticle interactions in our systems (hard-core Yukawa interactions) are very different from the interactions between the deformable particles in Ref. [129]. We note that data points for hard spheres, for which $\gamma \approx 2.6$ [128, 141], would fall in between the curves for $\kappa\bar{\sigma} = 10$ and $\kappa\bar{\sigma} = 3.3$. As suggested above (Section 4.3.3), this might be due to the fit range that we used. Due to lack of data points, it is not clear whether a different fit range would preserve the trend of decreasing fragility with increasing range of the potential.

For our charged colloidal suspensions, the range of the potential is determined by the Debye screening κ^{-1}, which is related to the monovalent salt concentration c_s in the suspension through $\kappa = \sqrt{8\pi\lambda_B c_s}$, with λ_B the Bjerrum length (see also Section 3.2.1). This suggests that in an experimental system the fragility can be adjusted by changing the salt concentration in the suspension.

4.4 Conclusions

We investigated the slow dynamics in hard-core repulsive Yukawa fluids in three systems with $\beta\bar{\epsilon} = 81$ (corresponding to dimensionless surface potential $\beta e\psi_0 \approx 2$) and $\kappa\bar{\sigma} = 2.5$, 3.3 and 10. To study the dynamics in the systems, we calculated self-intermediate scattering functions (SISFs) at three different values of q, one of which is close to the first peak of the structure factor, for a range of volume fractions η. The long-time relaxation of the SISF was fitted with a stretched exponential function, from which we obtained a structural relaxation time τ_α. We also calculated the mean square displacement (MSD), from which a value for the long-time self-diffusion coefficient D_L was obtained.

The structural relaxation time τ_α and the inverse self-diffusion coefficient D_L^{-1} could be well fitted both by the power law $\tau_\alpha \propto D_L^{-1} \propto (\eta_c - \eta)^{-\gamma}$, predicted by mode-coupling theory (MCT), and by the Vogel-Fulcher-Tammann (VFT) equa-

tion $\tau_\alpha \propto D_{\mathrm{L}}^{-1} \propto \exp\left[B\eta/(\eta_0 - \eta)\right]$, with η_0 much larger than η_{c}. We found that γ and B, as well as the relative distance between the monodisperse freezing volume fraction η_{f} and the glass transition volume fraction η_{c} or η_0, increased with increasing range of the potential (larger Debye screening length $(\kappa\bar{\sigma})^{-1}$). In addition, our results indicated that with increasing range of the potential the system became a stronger glass-former. This suggests the possibility to tune the fragility of an experimental system by changing the salt concentration (and thus $(\kappa\bar{\sigma})^{-1}$) in the suspension.

More data points would result in more reliable estimates for fit parameters γ and η_{c}, and B and η_0. The power-law scaling of τ_α and D_{L} is one of the predictions of MCT and the values for the exponents γ that we found are not unrealistic in the context of MCT [143]. Therefore, it would be interesting to compare γ and η_{c} with theoretical predictions from MCT or with results from experimental systems that interact through an effective hard-core Yukawa potential. It would be most interesting to test the possibility that the fragility in an experimental system can be adjusted by changing the salt concentration.

4.5 Acknowledgements

I would like to thank Michiel Hermes for providing the self-intermediate scattering function code and helpful discussions.

5

Expansion of charged colloids after centrifugation: formation and crystallisation of long-range repulsive glasses

We studied long-range repulsive glasses formed in suspensions of sterically stabilised charged colloidal poly(methyl methacrylate) particles ($\sigma = 2.23$ µm) with low polydispersity (3.6%) in the low-polar solvent cyclohexyl bromide ($\epsilon_r = 7.92$). Particle interactions were described by a long-range repulsive Yukawa potential. Glasses were obtained upon compression of the suspensions by centrifugation from a body-centred-cubic-crystalline structure at low initial volume fraction ($\eta \approx 0.02$) to a close-packed amorphous structure ($\eta \approx 0.64$). Subsequent expansion of the sediment in gravity resulted in long-range repulsive glassy structures with volume fractions $\eta = 0.16$–0.64. The presence of small clusters (mostly dumbbells; clustered fraction $f_{cl} \geq 0.12$) formed by centrifugation prevented the glasses from crystallising for several weeks, while the sediment was still expanding. We used confocal microscopy to obtain three-dimensional data sets of the system and quantitatively analysed the structure of the glasses. The structure of the glasses was found to be remarkably similar to that of hard-sphere glasses, despite the much longer-range interaction potential. After more than ten weeks the clustered fraction decreased due to spontaneous dissociation of the clusters, and finally bulk crystallisation of the glasses was observed into face-centred-cubic crystals with a volume fraction around 0.22.

5.1 Introduction

Colloidal systems are excellent model systems to study the behaviour of liquids, crystals, glasses and gels [1]. Experimental research on colloidal glasses has mainly been carried out in hard-sphere model systems [22, 127, 144–147]. Hard spheres exhibit a glass transition at a volume fraction $\eta \approx 0.56$–0.58, which was first found in systems of poly(methyl methacrylate) (PMMA) particles suspended in a decalin/carbon disulphide mixture [9], and later investigated quantitatively by dynamic light scattering [22, 127, 128] and in 3D real-space studies [11, 145, 146].

Few experimental studies exist that focus on the glass transition in systems of charged colloidal spheres with a significant double layer compared to the particle size. For example, in early work by Sirota et al. X-ray scattering revealed a glass phase for $\eta > 0.20$ in a system of monodisperse charge-stabilised polystyrene colloidal spheres suspended in a methanol/water mixture [30]. Later, Härtl et al. found a glass transition at $\eta = 0.22$ in a suspension of colloids made of polymerised perfluorobutylacrylate in a glycerol/water mixture. They used static and dynamic light scattering to measure intermediate scattering functions, and found agreement with mode-coupling theory [130]. Beck et al. applied static and dynamic light scattering to study a system of surface-functionalised silica colloids suspended in a glycerol/water mixture, for which a glass transition was found at $\eta = 0.18$. Furthermore, MCT was found to correctly predict the nonergodicity parameters from the fitted experimental static structure factors, as well as to correctly describe the intermediate scattering functions near the glass transition [131]. Recently, for the above-mentioned PMMA model system long-range repulsive interactions have become available even for micrometre-sized colloids [19].

This work is a quantitative 3D real-space study on the structure of long-range repulsive glasses formed in suspensions of sterically stabilised and charged colloidal particles with a double layer of the same size or larger than the particle size. More specifically, we employed a technique that dates back to Hachisu and Takano, who used it to speed up the equilibration time to achieve a sedimentation equilibrium for charged polystyrene particles in water under normal gravity conditions. First, the system was compressed to a metastable state by centrifugation and subsequently the sediment expanded towards an equilibrium state [148]. These authors used charged particle systems with added salt to achieve thin double layers compared to the particle size, thus approximating a hard-sphere potential. The method was extended by Van Duijneveldt et al. to charged silica particles with a longer double layer that were dispersed in a refractive-index-matching mixture of toluene and ethanol [149]. Those authors centrifuged a dispersion of silica particles with a diameter of 700 nm into an amorphous glassy state ($500g$, 30 min; with g the gravitational acceleration) and had the system expand over several weeks.

The original system crystallised into a face-centred-cubic (fcc) crystal at a volume fraction of 0.155. After a few hours of expansion, crystallisation was observed in the top of the sediment, while most of the sediment remained glassy. Even after several weeks, during which the top crystalline part grew to 2.3 mm in size (initial sediment length 1.7 cm), the bottom part remained amorphous. The crystal grown during the expansion was randomly stacked.

In the research presented in this chapter we are extending these experiments on compressed particle systems to long-range repulsive systems in which even for micrometre-sized particles double layers can be still significantly larger than the particle size; body-centred-cubic (bcc) crystals are observed as the equilibrium phase if the next-nearest-neighbour interactions become sufficiently important [19]. The sterically stabilised PMMA particles that we used are similar to those of several other studies; cyclohexyl bromide is a common (co)solvent as this solvent almost index-matches the particles [19, 39, 46, 121, 150–152]. We intended to study the glass transition for long-range repulsive systems, which has hardly been investigated experimentally, and wanted to compare the long-range repulsive glasses with hard-sphere glasses also made by sedimentation in a similar way as presented before [11]. We expected the amorphous sediment to expand and crystallise or form re-entrant liquid phases, which were observed on several occasions before for this model system at higher volume fractions and low salt concentrations [86, 150]. The re-entrant melting behaviour was likely caused by a reduction of the particle charge at higher volume fractions [46, 121], causing the particles to enter a regime of interparticle interaction parameters for which there is no crystal phase at higher volume fractions; this was recently explored theoretically [29]. However, instead we observed that a significant fraction of the particles ($f_{\mathrm{cl}} \geq 0.12$) formed clusters during the compression by centrifugation. These clusters mainly consisted of two particles (so-called dumbbells), but nonetheless completely frustrated crystallisation. Only when after 81 days of expansion the repulsive interactions became stronger than the attractions and the particle clusters disappeared, did the system fully crystallise. Finally, it is relevant to mention that although it was found that a pairwise-additive interaction potential could describe the particle interactions at a range of volume fractions for parameters close to those studied here [39], other studies strongly indicate that a pair interaction alone does not give a good description [151–154].

This chapter is organised as follows. In Section 5.2 we describe the model system, experimental procedure and data analysis, in Section 5.3 we discuss the results, and in Section 5.4 we present our conclusions.

5.2 Experimental methods

5.2.1 Model system

We used poly(methyl methacrylate) spheres (PMMA; density $d_{\mathrm{PMMA}} = 1.19$ g cm^{-3}; dielectric constant $\epsilon_{\mathrm{r}} = 2.6$; refractive index $n_{\mathrm{D}}^{25} = 1.492$ [18]), sterically stabilised by a covalently bonded layer of a graft copolymer consisting of poly(12-hydroxystearic acid) (PHSA) grafted onto a PMMA backbone [84]. The particles were synthesised by dispersion polymerisation [83, 85] and labelled with the fluorescent dye 7-nitrobenzo-2-oxa-1,3-diazol (NBD), by covalent incorporation into the PMMA [83]. The average diameter σ of the particles was 2.23 µm and the polydispersity 3.6%, as determined by scanning electron microscopy (SEM). To determine the average diameter and size polydispersity from the SEM images we measured ~ 100 particles using the program iTEM (Olympus Soft Imaging Solutions GmbH). The particles were suspended in cyclohexyl bromide (CHB; Acros Organics; density $d_{\mathrm{CHB}} = 1.336$ g cm^{-3} [18]; dielectric constant $\epsilon_{\mathrm{r}} = 7.92$ [69]; refractive index $n_{\mathrm{D}}^{25} = 1.4935$ [18, 69]), which nearly matched the refractive index of the PMMA particles ($n_{\mathrm{D}}^{25} = 1.492$). This solvent is known to decompose in time, a process which generates H^+ and Br^- ions (see Ref. [86] and chapter 2 of Ref. [18]). To reduce the ionic strength, we cleaned the solvent before use [87], by bringing it into contact first with activated alumina ($\mathrm{Al_2O_3}$; 58 Å, ~ 150 mesh, Sigma-Aldrich) and then with molecular sieves (4 Å, 10–18 mesh, Acros Organics). The conductivity of CHB after the cleaning steps was 5.2 pS cm^{-1} (Scientifica 627 conductivity meter). We measured the electrophoretic mobility of the particles at a volume fraction $\eta = 0.031$ (as described in Chapter 2; see also Ref. [46]) and from this calculated an average charge number $Z = 609 \pm 22$ per particle. In Section 5.3.4 we will discuss the system parameters further.

The pair interaction in a system of charged colloidal particles is commonly described by a hard-core repulsive Yukawa (screened Coulomb) potential [15, 16, 31, 39]:

$$\beta u_{ij}(r) = \begin{cases} \beta\epsilon_{ij} \dfrac{\exp\left[-\kappa(r-\sigma_{ij})\right]}{r/\sigma_{ij}} & r \geq \sigma_{ij} \\ \\ \infty & r < \sigma_{ij} \end{cases}, \tag{5.1}$$

with $\sigma_{ij} = (\sigma_i + \sigma_j)/2$ and the contact value of the potential between two colloids i and j:

$$\beta\epsilon_{ij} = \frac{Z_i Z_j}{(1+\kappa\sigma_i/2)(1+\kappa\sigma_j/2)} \frac{\lambda_{\mathrm{B}}}{\sigma_{ij}}, \tag{5.2}$$

where r is the centre-to-centre distance between particles i and j, Z_i (Z_j) and σ_i (σ_j) are the charge number and diameter of colloid i (j), $\beta = 1/(k_{\mathrm{B}}T)$, with k_{B}

the Boltzmann constant, and T the absolute temperature. The Bjerrum length is given by

$$\lambda_{\mathrm{B}} = \frac{e^2}{4\pi\epsilon_{\mathrm{r}}\epsilon_0 k_{\mathrm{B}} T}\,, \tag{5.3}$$

with e the elementary charge, ϵ_{r} the relative dielectric constant of the solvent and ϵ_0 the dielectric permittivity of vacuum. The Bjerrum length represents the distance at which the electrostatic interaction energy between two monovalent ions is equal to the thermal energy $k_{\mathrm{B}}T$. The inverse Debye screening length is given by

$$\kappa = \sqrt{8\pi\lambda_{\mathrm{B}} c_{\mathrm{s}}}\,, \tag{5.4}$$

with c_{s} the concentration of the monovalent salt. The Debye screening length κ^{-1} indicates the thickness of the electrical double layer surrounding a colloidal particle and is a measure for the interaction range between two colloids. When the refractive index of the solvent closely matches that of the particles, as is the case in our experimental system, the Van der Waals interactions are much smaller than $k_{\mathrm{B}}T$ and can be neglected.

For monodisperse systems, $\sigma_{ij} = \sigma$, and the contact value of the potential between two colloids simplifies to

$$\beta\epsilon = \frac{Z^2}{(1+\kappa\sigma/2)^2}\frac{\lambda_{\mathrm{B}}}{\sigma}\,. \tag{5.5}$$

The electrostatic surface potential ψ_0 for an isolated particle can be approximated at low ψ_0 by [12]

$$\beta e\psi_0 = \frac{Z}{1+\kappa\sigma/2}\frac{2\lambda_{\mathrm{B}}}{\sigma}\,. \tag{5.6}$$

Combining Eqs. 5.5 and 5.6 yields the relation between ϵ and ψ_0:

$$\beta\epsilon = \frac{(\beta e\psi_0)^2}{4}\frac{\sigma}{\lambda_{\mathrm{B}}}\,. \tag{5.7}$$

The hard-sphere system that we used for comparison consisted of 1.37 µm core-shell silica particles (determined by static light scattering (SLS); polydispersity $\approx 3\%$) with a 434 nm core labelled with the fluorescent dye fluorescein isothiocyanate (FITC) [11], suspended in a mixture of dimethyl sulphoxide (DMSO) and deionised water (8.2% water by weight); the refractive index closely matched that of the particles. We compared the radial distribution function $g(r)$ for experimentally obtained glassy structures to the $g(r)$ for computer-generated glassy structures; we found very good agreement, with the effective hard-sphere diameter only 3.6% larger than the diameter obtained from SLS. The double layer was thus

thin compared to the particle diameter and we assumed the interactions could be described by a hard-sphere potential, similar to Ref. [11].

5.2.2 Compression by centrifugation and confocal microscopy

We prepared suspensions with an initial volume fraction $\eta \approx 0.02$, which were transferred to a borosilicate glass capillary with inner dimensions 5 cm × 1.0 mm × 0.10 mm ($x \times y \times z$; VitroCom), mounted on a microscope glass slide. The suspension occupied approximately two-thirds of the capillary. The remaining part was filled with deionised water (milli-Q water, resistivity = 18.2 MΩ cm, Millipore), which acted as a sink for ions from the suspension, thus keeping the ionic strength low and the Debye screening length large. Both ends of the capillary were sealed with UV-curing optical adhesive (Norland no. 68).

We centrifuged the samples for 15–110 minutes at 15–107g (Eppendorf Centrifuge 5810), keeping the water phase on top. During centrifugation the particles were compressed on the water-CHB interface (PMMA has a lower density than CHB), where they formed a sediment; a schematic overview of the sample is given in Fig. 5.1. The centrifugal field was directed along the long axis of the capillaries. After centrifugation the capillaries were stored vertically, with gravity pointing along the long axis.

We used confocal microscopy (Nikon C1 confocal microscope) with a 100× NA 1.4 oil immersion objective, in fluorescence mode with 488 nm excitation, to obtain three-dimensional stacks of images (typical stack: 256 × 256 × 129–184 pixels ($x \times y \times z$); pixel size was in most cases 0.25 or 0.33 µm in xy and 0.27 or 0.39 µm in z; ∼ 1.7 frames per second). Stacks were taken at several distances from the water-CHB interface, and at least 15 µm from the walls of the capillary to avoid wall-induced effects. During the measurements the capillaries were also kept in a vertical position, on a microscope frame tilted 90 degrees with respect to gravity.

The hard-sphere silica system underwent a similar procedure. We constructed sample cells with inner dimensions ∼ 2 cm × 6 mm × 150–180 µm, by glueing three strips of glass cut from a coverslip (thickness 130–160 µm, no. 1 coverslip, Menzel) in a U-shape onto a microscope glass slide using 2-component epoxy adhesive (Bison), and sticking a second coverslip on top. The glue was left to harden for at least 24 hours. The sample cells were filled from a Pasteur pipette with the suspension of silica in DMSO/water ($\eta \approx 0.10$) and centrifuged for at least 10 minutes at 9–2012g (Hettich Rotina 46 S centrifuge). After centrifugation, the open end was sealed with epoxy adhesive. We used a Leica TCS NT confocal microscope to image the samples (typical stack: 512 × 512 × 100 pixels ($x \times y \times z$);

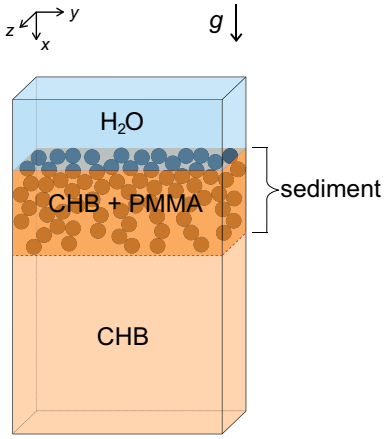

Figure 5.1: Schematic overview of the sample after centrifugation (not drawn to scale). The glass capillary contained a water phase on top of a suspension of PMMA particles in CHB. The centrifugal field was pointing down (direction indicated by arrow next to g), but the particles sedimented upwards (creamed) and were compressed on the water-CHB interface by the centrifugal field, where they formed a sediment. After centrifugation the capillaries were stored vertically, with gravity pointing down (direction indicated by arrow next to g).

pixel size was 0.10 µm in xy and 0.20 µm in z; image stacks were taken at least 20 µm from the sample cell wall).

5.2.3 Data analysis

We obtained the positions of the particles using algorithms similar to those described in Refs. [88] and [155]. For subsequent data analysis we used all particles contained in a rectangular box with boundaries half a particle diameter from the edges of the image stack.

From the particle coordinates we calculated the radial distribution function $g(r)$, which describes the average positional order in the system. The radial distribution function gives the probability of finding a particle at a distance r from a given particle relative to the same probability in an uncorrelated configuration, or ideal gas, with the same number density. The quantity $4\pi r^2 \rho g(r)\,\mathrm{d}r$ is the number of particles found in a spherical shell of radius r and thickness $\mathrm{d}r$ around a given particle, where ρ is the average number density in the system [2]. We calculated the normalised probability distribution of pair distances for our system and corrected for the finite size of the box by dividing by the normalised probability distribution

of pair distances that was calculated for an uncorrelated (ideal gas) configuration contained in a box of the same spatial dimensions (see also Ref. [39]).

The local bond-orientational order was examined as follows. For each particle i we defined a set of $2l+1$ bond-orientational order parameters [34, 35]

$$q_{lm}(i) = \frac{1}{N_\mathrm{b}(i)} \sum_{j=1}^{N_\mathrm{b}(i)} Y_{lm}(\theta_{ij}, \phi_{ij}) \,, \tag{5.8}$$

where $N_\mathrm{b}(i)$ is the number of neighbours of particle i, θ_{ij} and ϕ_{ij} are the inclination and azimuth angles of the bond $\mathbf{r}_{ij} = \mathbf{r}_i - \mathbf{r}_j$ (where $\mathbf{r}_i$ ($\mathbf{r}_j$) denotes the position of particle i (j)) connecting the centres of particle i and its neighbour j, and $Y_{lm}(\theta_{ij}, \phi_{ij})$ are the spherical harmonics (with $m = -l, -l+1, \ldots, l-1, l$). The sum runs over all neighbours of particle i. The neighbours of particle i were defined as all particles within a certain cut-off distance r_c from particle i.

We used these sets of bond-orientational order parameters to calculate three different rotational invariants: $\hat{w}_l$, $\bar{q}_l$ and $\bar{w}_l$, as described below.

The local bond-orientational order parameter $\hat{w}_l$ was calculated in the following way [34]:

$$\hat{w}_l(i) = \frac{\displaystyle\sum_{m_1+m_2+m_3=0} \begin{pmatrix} l & l & l \\ m_1 & m_2 & m_3 \end{pmatrix} q_{lm_1}(i) q_{lm_2}(i) q_{lm_3}(i)}{\left(\displaystyle\sum_{m=-l}^{l} |q_{lm}(i)|^2 \right)^{3/2}} \,, \tag{5.9}$$

where $q_{lm}(i)$ is defined in Eq. 5.8 and the coefficient in the numerator is a Wigner $3j$ symbol [156]; the integers m_1, m_2 and m_3 run from $-l$ to $+l$, provided $m_1 + m_2 + m_3 = 0$. $\hat{w}_l$ is one of the order parameters defined by Steinhardt et al. (denoted by them as $\hat{W}_l$) [34]. For hard-sphere glasses, the distribution of $\hat{w}_6$ was reported in Ref. [11] (denoted in Ref. [11] as W_6), enabling us to compare the structure of our long-range repulsive glasses to that of hard-sphere glasses.

Due to thermal fluctuations, the distributions of the Steinhardt order parameters can be rather broad, making it difficult to determine the type of local environment for each individual particle. Instead, we followed the method of Lechner and Dellago [35]. They averaged the sets of bond-orientational order parameters from Eq. 5.8 over the central particle and its nearest neighbours. The distributions of these averaged order parameters are much narrower than those of the Steinhardt order parameters, and very suitable to distinguish between disordered and crystalline particle environments, as well as, in the latter case, to determine the type of crystalline environment.

So, we averaged each of the members of the set from Eq. 5.8 over the central particle and its neighbours, to obtain for each particle i a set of *averaged* bond-orientational order parameters

$$\bar{q}_{lm}(i) = \frac{1}{N_\mathrm{b}(i)+1} \sum_{j=0}^{N_\mathrm{b}(i)} q_{lm}(j)\,, \tag{5.10}$$

where the sum runs over all neighbours of particle i plus particle i itself. From these sets of averaged bond-orientational order parameters, we obtained the averaged local bond-orientational order parameters [35]

$$\bar{q}_l(i) = \sqrt{\frac{4\pi}{2l+1} \sum_{m=-l}^{l} |\bar{q}_{lm}(i)|^2} \tag{5.11}$$

and

$$\bar{w}_l(i) = \frac{\displaystyle\sum_{m_1+m_2+m_3=0} \begin{pmatrix} l & l & l \\ m_1 & m_2 & m_3 \end{pmatrix} \bar{q}_{lm_1}(i)\bar{q}_{lm_2}(i)\bar{q}_{lm_3}(i)}{\left(\displaystyle\sum_{m=-l}^{l} |\bar{q}_{lm}(i)|^2\right)^{3/2}}\,, \tag{5.12}$$

where $\bar{q}_{lm}(i)$ is defined in Eq. 5.10 and the coefficient and sum in the numerator are the same as in Eq. 5.9.

Finally, we looked at the fraction of crystalline particles in the system. Crystalline particles were identified by calculating the correlation between the sets of bond-orientational order parameters for each pair of neighbouring particles, given by

$$c_l(ij) = \frac{\displaystyle\sum_{m=-l}^{l} q_{lm}(i) q^*_{lm}(j)}{\left(\displaystyle\sum_{m=-l}^{l} |q_{lm}(i)|^2\right)^{1/2} \left(\displaystyle\sum_{m=-l}^{l} |q_{lm}(j)|^2\right)^{1/2}}\,, \tag{5.13}$$

where $q^*_{lm}(j)$ is the complex conjugate of $q_{lm}(j)$, and $q_{lm}(i)$ and $q_{lm}(j)$ are defined in Eq. 5.8. A neighbour j to particle i was defined as a connected neighbour, if $c_l(ij)$ exceeded a threshold value c_c. Particles with more than a certain number n_c of connected neighbours were defined as crystalline particles [36]. The crystalline fraction is then $f_\mathrm{X} = N_\mathrm{X}/N$, with N_X the number of crystalline particles and N the total number of particles in a certain volume of the sample. For our analysis

we chose $l = 6$, $r_c = 1.5\rho^{-1/3}$ (with $\rho = N/V$ the number density of the particles, and $\rho^{-1/3}$ the characteristic interparticle distance), $c_c = 0.6$ and $n_c = 8$.

Instead of using a cut-off distance, which is always arbitrary, to define the nearest neighbours of a particle, it is possible to use the Voronoi construction to define neighbours. To this end, the Voronoi cell for each particle is calculated, containing all points in space that are closer to that particle than to any other particle. Particles that share a Voronoi face can now be defined as nearest neighbours. This method was used in Ref. [11] for hard-sphere glasses to calculate the $\hat{w}_6$ distribution (as mentioned above). The distribution of the number of faces per Voronoi cell $P(n_n)$ (which is the same as the number of neighbours per particle) and the distribution of number of edges per Voronoi face $P(n_e)$ were also calculated. We employed the Voronoi construction to define neighbours for some of our data sets in order to compare with Ref. [11].

The Steinhardt bond order parameters (in our case, $\hat{w}_l$, defined in Eq. 5.9) depend on the arrangement of the nearest neighbours of the central particle, i.e. the first-neighbour-shell particles. In our analysis, we calculated $\hat{w}_l$ for particles that were at least a distance r_c from the box boundaries, thus ensuring that we did not miss out some of the neighbours. When we used the Voronoi construction to define neighbours, we included only the $\hat{w}_l$ values of particles that were fully surrounded by neighbours, i.e. particles that did not share a Voronoi face with the box boundary. The averaged bond order parameters ($\bar{q}_l$, $\bar{w}_l$), as well as the crystallinity calculated through the bond order correlation method, depend also on the position of the second-neighbour-shell particles. Therefore, $\bar{q}_l$, $\bar{w}_l$ and the crystallinity were only calculated for particles that were at least a distance $2r_c$ from the box boundaries. In the Voronoi case, we included only the values of particles whose neighbours were fully surrounded by neighbours.

We used a distance criterion to identify particles that were part of a cluster: particles that had at least one neighbour at a distance $r < r_{cl}$ were defined as clustered particles. The *clustered* fraction is then $f_{cl} = N_{cl}/N$, with N_{cl} the number of clustered particles, i.e. particles part of a cluster, and N the total number of particles in a certain volume of the sample. We chose r_{cl} between the main peak of the $g(r)$ and the small peak at smaller distance close to the main peak, which resulted in $r_{cl} = 1.1\sigma$. With increasing volume fraction the probability to find two non-clustered particles separated by a distance $r < r_{cl}$ increases. For denser systems, it was therefore not possible to find the clustered fraction via this distance analysis procedure, and we did not plot f_{cl} for configurations with $\eta > 0.30$, a value chosen somewhat arbitrarily.

5.3 Results and discussion

We imaged the samples with confocal microscopy, obtaining $\sim$ 20 three-dimensional data sets along the entire height of the sediment (typical spacing between data sets was 100 µm). We centrifuged samples at different speeds (15–107g) and followed them a few days to a week. We found no qualitative dependence of the resulting structures on the centrifugation speed. Two samples (centrifuged at 15g for 110 minutes and at 42g for 40 minutes) were followed during a much longer time period (2–3 months). Both samples had not fully sedimented after centrifugation was stopped and showed similar behaviour in time, including particle clustering. Below, we describe the behaviour of one of these samples (centrifuged at 15g), which we analysed in detail.

Section 5.3.1 gives an overview of the expansion and contraction of the sediment in time and the resulting volume fraction profiles of the sediment. In Section 5.3.2 we describe the formation and crystallisation of long-range repulsive glassy structures and show the correlation between the presence of glassy structures and clustered particles. In Section 5.3.3 the structural analysis of the glassy parts is described in detail and the structure is compared to that of hard-sphere glasses. In Section 5.3.4 we report on the structural analysis of the crystalline parts and the crystal symmetries that were identified. Finally, in Section 5.3.5, we describe additional experiments we performed to investigate the mechanism of clustering and declustering and we discuss a possible origin of the attractions responsible for cluster formation.

5.3.1 Expansion and contraction of the sediment

The sample was imaged directly after centrifugation ($t = 0$ days after compression by centrifugation) and subsequently after 1, 2, 4, 7, 14, 21, 35, 49, 64 and 81 days. We calculated the volume fraction η in each of the data sets from the number of particles N found by the tracking routine, the average particle diameter σ and the volume of the box V in which the particles were contained, through $\eta = N\pi\sigma^3/(6V)$. The left part of Fig. 5.2 shows the volume fraction profiles (volume fraction η versus distance x from the water-CHB interface) for different times t. We show the results of six different measurement days.

A centrifugal field or (after centrifugation) gravity caused the particles to migrate towards the water-CHB interface, which was located at $x = 0$ mm. Directly after centrifugation ($t = 0$ days), the particles that were furthest from the interface were still moving towards the interface, because, as was mentioned above, the sample had not been fully compressed during centrifugation; this caused the total height of the sediment to decrease. Here, the total height of the sediment is

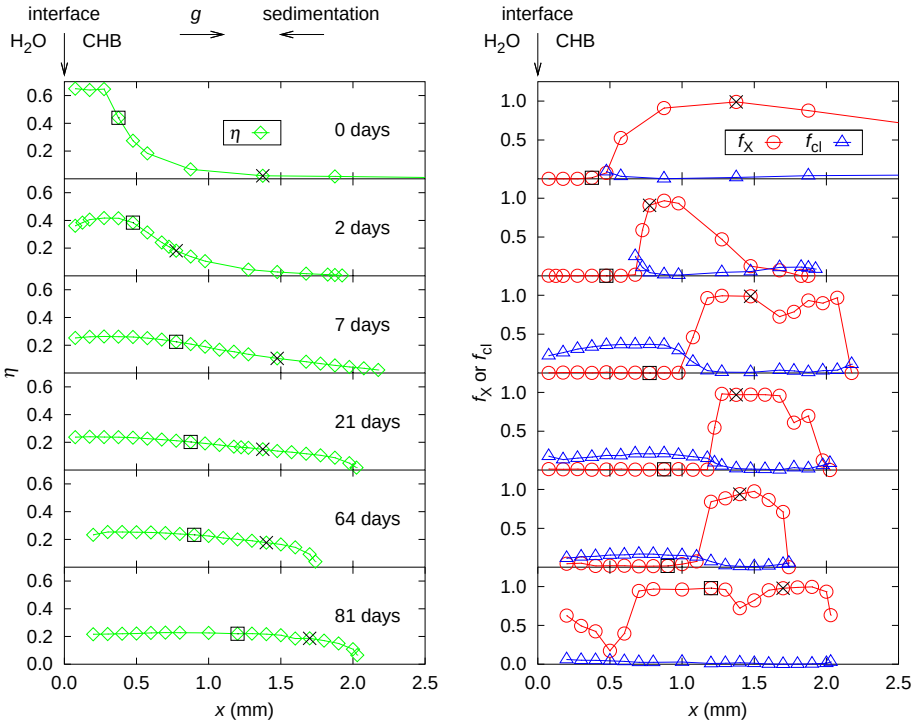

Figure 5.2: Volume fraction η (left), and crystalline fraction $f_{\rm X}$ and clustered fraction $f_{\rm cl}$ (right) plotted versus the distance from the water-CHB interface x for different waiting times (t = 0–81 days). Black squares and black crosses indicate respectively an initially (at t=0 days) glassy and initially crystalline spot in the sediment; the position of these spots changed in time due to expansion and contraction of the sediment. The configurations correspond to data points in Figs. 5.3b (squares) and 5.3c (crosses). At the top of the figure we indicate the position of the water-CHB interface (at $x = 0$ mm), the direction of gravity (g) and the direction of sedimentation of the particles.

the distance from the interface beyond which virtually no particles can be found. In Fig. 5.2 the total height of the sediment at $t = 0$ days is beyond the scale of the graph. After 2 days the total height reached a value slightly less than 2 mm (Fig. 5.2, left, second panel from top), after which it started to increase. Meanwhile, the dense part of the sediment, close to the interface, which had been compressed by the centrifugal field, started to expand and particles migrated away from the interface. These particles had been forced into a close-packed and amorphous configuration by the centrifugal field. Without the presence of this field, the dense part of the sediment expanded due to the repulsive interactions between the charged particles. This effect caused the total height of the sediment to reach a maximum value at $t = 7$ days. For $t = 7$–64 days, the total height slowly decreased again. Presumably, this was due to an increasing concentration of background ions and thus decreasing Debye screening length, most likely caused by slow decomposition of the solvent CHB, a process which generates ions (H^+ and Br^-, as mentioned above). Apparently, the uptake of ions by the water phase was not sufficient to keep the ionic strength constant. See below (Section 5.3.4) for estimates of the decrease of $(\kappa\sigma)^{-1}$ as a result of the increase in ionic strength, which was initially low enough to allow parts of the system to crystallise with bcc symmetry.

This sequence of events is consistent with the values for the maximum volume fraction found in the sediment. The maximum volume fraction was $\eta = 0.64$ at $t = 0$ days, and reached a temporary minimum at $t = 14$ days, $\eta = 0.24$ (not shown), expansion of the dense part of the sediment being the dominant effect. After that it increased slowly and continuously to $\eta = 0.25$ at $t = 64$, presumably due to a decrease in screening length. In time the volume fraction profile flattened out to an almost horizontal line at $t = 81$ days (Fig. 5.2, left, bottom panel).

At $t = 81$ days we found an increased total height and a decreased maximum volume fraction ($\eta = 0.23$). On this measurement day we observed large droplets of water ($\sim$ 5–40 µm) in the CHB phase close to the water-CHB interface. Since the droplets contained no particles, they pushed the particles away from the interface, increasing the height of the sediment. The decreased volume fraction suggests that the Debye screening length also increased.

5.3.2 Formation and crystallisation of glassy structures

For each data set, we calculated the crystalline fraction f_X and the clustered fraction f_{cl} (the fraction of particles that was part of a cluster), using the methods described in Section 5.2.3. The right part of Fig. 5.2 shows the crystalline fraction f_X and clustered fraction f_{cl} versus distance x from the water-CHB interface for different times after centrifugation was stopped. In addition, Fig. 5.3a shows

the number of particles, number of crystalline particles and number of clustered particles in the entire sediment, obtained by integrating the volume fraction profiles in Fig. 5.2 over the volume of the suspension in the capillary and dividing by the volume of a single particle $v = \pi\sigma^3/6$.

We expect the number of particles in the system to stay constant. This was indeed the case for $t = 4$–64 days, as indicated by the dashed black line through the green diamonds in Fig. 5.3a. For $t < 4$ days not all particles were correctly identified by the tracking routine due to the high densities of the system close to the water-CHB interface. For $t = 81$ days, the number of particles was overestimated due to the presence of particle-free droplets of water in the CHB phase, as mentioned above.

Before centrifugation, we checked the sample ($\eta \approx 0.02$), and found it was fully crystalline with the crystal phase being bcc. We discuss the symmetries of the crystalline parts in more detail in a separate section below (Section 5.3.4). After centrifugation, we found subsequently (moving through the sediment away from the interface) a glassy part adjacent to the interface (with $f_X < 0.05$), a crystalline part and a fluid part (Fig. 5.2, right). The system stayed like this until $t = 64$ days. During this time period no extensive crystallisation took place, as we can see from the fact that the total number of crystalline particles hardly changed (Fig. 5.3a), comprising $\sim 25\%$ of the total number of particles in the sediment (indicated by the dashed black line through the red circles in Fig. 5.3a). The number of clustered particles during the same period decreased, but from $t = 21$ days only very slowly, reaching a kind of plateau with a value corresponding to $\sim 13\%$ of the total number of particles (indicated by the dashed black line through the blue triangles in Fig. 5.3a). At $t = 81$ days we found that the number of clustered particles ($\sim 3\%$ of the particles) was much lower than before, while a significant part of the sample had crystallised ($\sim 88\%$ of the particles were crystalline) (these numbers were calculated using the total number of particles in the sample indicated by the dashed black line in Fig. 5.3a).

From the right part of Fig. 5.2 we see that the clusters were not evenly distributed across the sediment. In general, f_{cl} was high in places where f_X is low, and vice versa, i.e. the glassy part contained more clusters than the crystalline part. As mentioned above, the clustered fraction f_{cl} is not plotted for the denser part of the sediment ($\eta > 0.30$) at $t = 0$ and 2 days, since we could not use a distance criterion to correctly identify clusters in denser systems. The slight increase in f_{cl} on the low-density side of the sediment is not real, but due to particles that were erroneously found twice by the tracking routine, and therefore can be ignored.

To quantify the difference between a typical glassy and typical crystalline configuration, we depicted in Figs. 5.3b and c in more detail the behaviour of η, f_X and f_{cl} in time for two particular spots in the sample: one located in the part

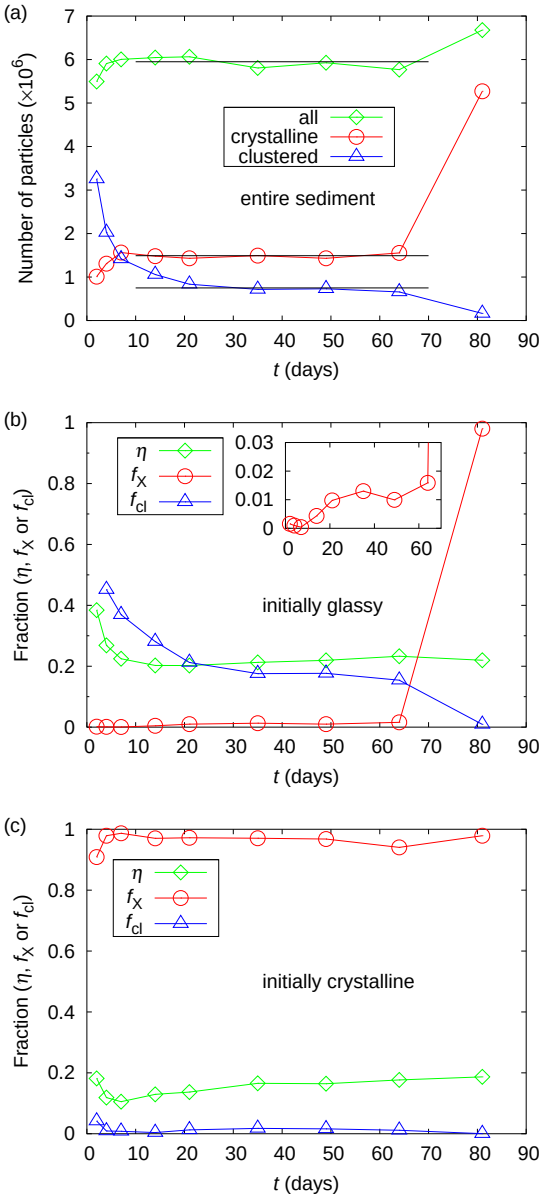

Figure 5.3: (a) Number of particles, number of crystalline particles and number of clustered particles in the entire sediment as a function of waiting time t. (b) Volume fraction η, crystalline fraction f_{X} and clustered fraction f_{cl} as a function of waiting time t for an initially (at $t = 0$ days) glassy spot in the sediment (black squares in Fig. 5.2). The inset shows f_{X} at a different scale. (c) The same, but for an initially crystalline spot (black crosses in Fig. 5.2).

of the system that was initially glassy (Fig. 5.3b and black squares in Fig. 5.2), the other from the part of the system that was initially crystalline (Fig. 5.3c and black crosses in Fig. 5.2). From the integrated volume fraction profiles we were able to locate approximately the same spot in the sample for each measurement day. The spots were located by counting particles starting from the low-density side of the sediment: on each measurement day approximately the same number of particles could be found on the low-density side of the indicated spot. The clustered fraction in the initially glassy configuration decreased from $f_{\rm cl} = 0.45$ at $t = 4$ days to $f_{\rm cl} = 0.15$ at $t = 64$ days, while in the initially crystalline configuration $0.00 \leq f_{\rm cl} \leq 0.02$. At $t = 81$ days, when the initially glassy configuration had crystallised, $f_{\rm cl}$ had dropped to 0.01. During the first 64 days the crystalline fraction in the initially glassy configuration increased very slowly from $f_{\rm X} = 0.00$ to $f_{\rm X} = 0.02$ (as shown in the inset of Fig. 5.3b), before making a large jump to $f_{\rm X} = 0.98$ at $t = 81$ days. Clearly, the crystalline configurations contain significantly fewer clusters ($\sim$ a few percent) than the glassy configurations ($\sim$ tens of percents), regardless of the initial structure of the crystalline configuration.

From these observations we conclude that a clustered fraction $f_{\rm cl}$ above a certain threshold value prevented crystallisation. When the particles were pressed together by the centrifugal field, clusters were formed in the dense part of the sediment. After centrifugation, when the sample was kept in gravity, the dense part of the sediment expanded and subsequently, during a long time, the number of clusters decreased. Finally, after 64–81 days, the clusters almost completely disappeared by spontaneous dissociation. In order to elucidate the mechanism of clustering and the subsequent declustering we investigated this phenomenon separately, as described in Section 5.3.5. Up to $t = 64$ days the $f_{\rm cl}$ was sufficiently high to allow only a very small fraction of the particles to become crystalline. At some point during the time period $t = 64$–81 days, when $f_{\rm cl}$ dropped below a threshold value (which must be somewhere between 0.15 and 0.01), crystallisation was no longer frustrated, and almost the entire system was able to crystallise. The lowest $f_{\rm cl}$ observed for a glass (structure with $f_{\rm X} < 0.05$) was 0.12; so, apparently, $f_{\rm cl} = 0.12$ was sufficient to frustrate crystallisation.

We looked in more detail at the size of the clusters present in the sample. We calculated the cluster size distributions, and found that most of the clusters were dumbbells, the fraction in the glassy parts of the sample increasing from $\sim 75\%$ at $t = 7$ days to $\sim 86\%$ at $t = 64$ days. Only a small number of clusters consisted of more than four particles, their fraction decreasing from $\sim 3\%$ to $\sim 1\%$ during the same period.

Fig. 5.4 shows a glassy part of the sample at $t = 21$ days, for which we indicated the clusters found by our distance criterion. We recorded a sequence of 25 images with time step $\Delta t = 120$ s. In Fig. 5.4 the first frame of the movie is shown (top

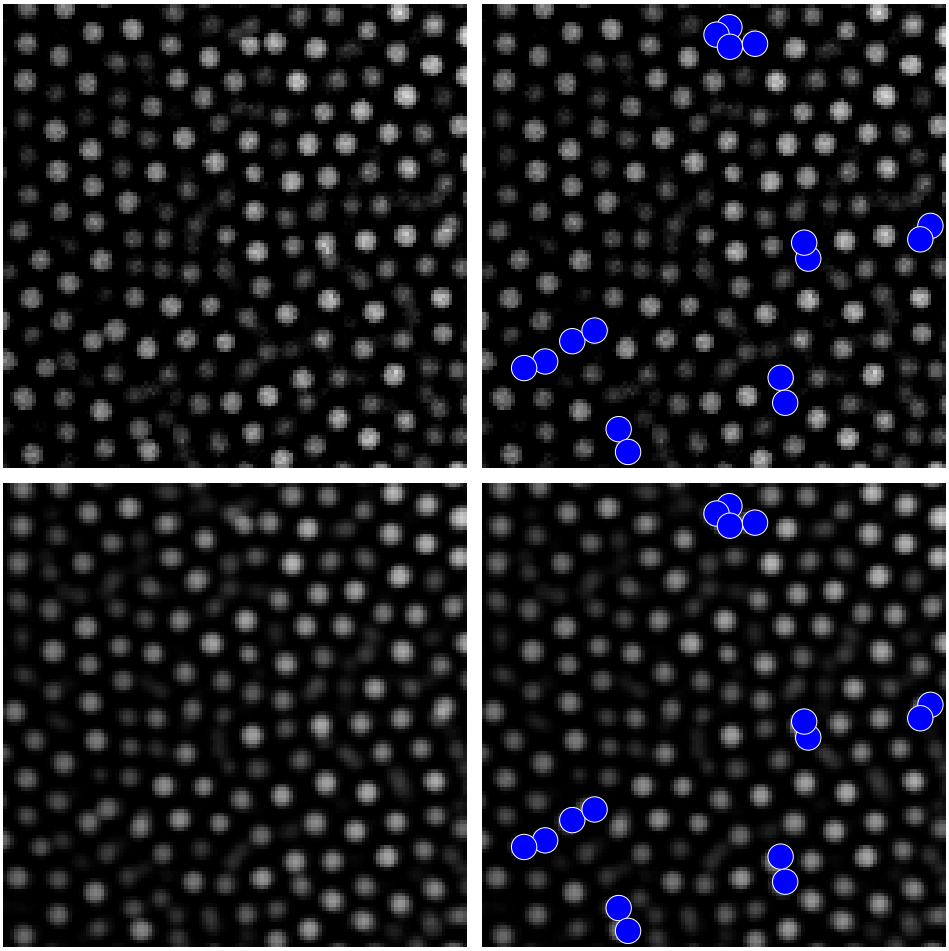

Figure 5.4: Long-term structural arrest in a glassy part of the sample at $t = 21$ days with $\eta = 0.17$, $f_X = 0.01$ and $f_{cl} = 0.15$. Top images: first frame of a series of 25 confocal images (42.5 µm × 42.5 µm) taken at the same position in the sample, but at different points in time. Bottom images: average intensity of the entire image series. Images were taken with a time step $\Delta t = 120$ s. Each image is shown twice, on the right we indicated the clustered particles (blue circles) found by distance analysis of a three-dimensional data set, taken at the same xy position in the sample. The corresponding movie is available in the supplementary information [95].

left), as well as the average intensity of the 25 images (bottom left). It is clear from the average intensity that the system was dynamically arrested, as the particle positions hardly changed over the course of 48 minutes. We obtained the locations of the clusters from a three-dimensional data set taken at the same xy position; the clustered particles that are part of clusters for which more than one member is visible in the image, are indicated by blue circles (Fig. 5.4, right). The clustered particles can also be recognised in the corresponding movie from the correlated motion of the particles (see movie in the supplementary information [95]). From the motion of the particles one identifies the same clusters as found by the distance criterion we used. The movie shows that the particles were able to move over small distances (cage-rattling motion), but almost all remained confined to the cage formed by their neighbours on the timescale of the movie.

5.3.3 Structural analysis of the glasses

Fig. 5.5 shows the radial distribution function $g(r)$ for three long-range repulsive glasses (corresponding to the data points in Fig. 5.3b at $t = 7$, 21 and 64 days). For comparison, we also show the $g(r)$ determined experimentally in a glassy system of silica spheres, which interact as effective hard spheres (see Section 5.2.1). The radial distribution functions for the long-range repulsive glasses have been rescaled, such that their maxima and minima coincide with those of the hard-sphere glass. For the hard-sphere glass we found a split second peak, similar as found before for hard-sphere glasses [11, 157–159]. The left and right subpeaks correspond to different local particle arrangements; both correspond to a pair of particles that are in each other's second-neighbour shell, but have either three first neighbours (left subpeak) or one first neighbour (right subpeak) in common [160]. Their relative heights vary according to the local structure, which depends on the system's characteristics, e.g. its polydispersity and the type of particles [160, 161]. For the long-range repulsive glasses, we found a second peak with a shoulder to its right. The small peak to the left of the main peak, present for the long-range repulsive glasses, is due to the clustered particles.

Fig. 5.6a shows the $\hat{w}_6$ probability distribution for the three long-range repulsive glasses and the hard-sphere glass. The distributions were calculated using the Voronoi construction to define the neighbours (see Section 5.2.3) in order to make a comparison with the structure of hard-sphere glasses as published in Ref. [11]. The same distributions calculated using a cut-off of $1.5\rho^{-1/3}$ to define the neighbours were very similar to the distributions shown in Fig. 5.6a; using those instead would not change the conclusions.

Despite the large difference in volume fraction and particle interactions between the long-range repulsive and hard-sphere glasses, the local bond-orientational order

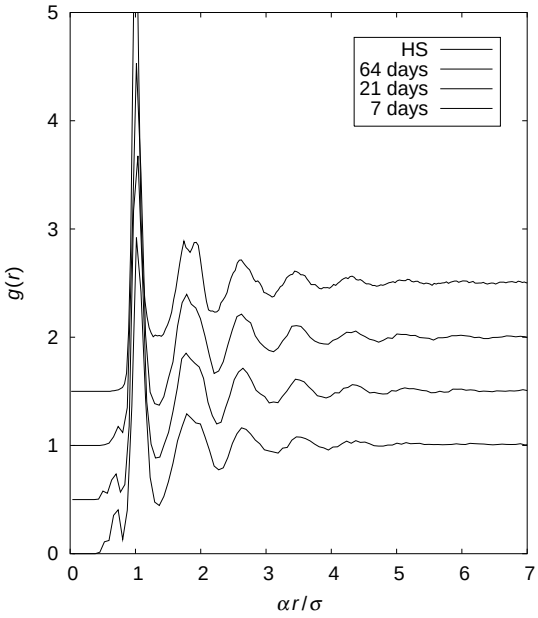

Figure 5.5: Radial distribution function $g(r)$ for three long-range repulsive glasses (corresponding to the data points in Fig. 5.3b; $t = 7$ days, $\eta = 0.22$, $f_{\rm X} = 0.00$, $f_{\rm cl} = 0.37$; $t = 21$ days, $\eta = 0.20$, $f_{\rm X} = 0.01$, $f_{\rm cl} = 0.21$; $t = 64$ days, $\eta = 0.23$, $f_{\rm X} = 0.02$, $f_{\rm cl} = 0.15$). The $g(r)$ for a hard-sphere glass is also shown for comparison ($\eta = 0.64$, $f_{\rm X} = 0.01$). The radial distribution functions for the long-range repulsive glasses have been rescaled, with $\alpha = 0.70$, 0.67 and 0.70, respectively, for $t = 7$, 21 and 64 days; for the hard-sphere glass $\alpha = 1$.

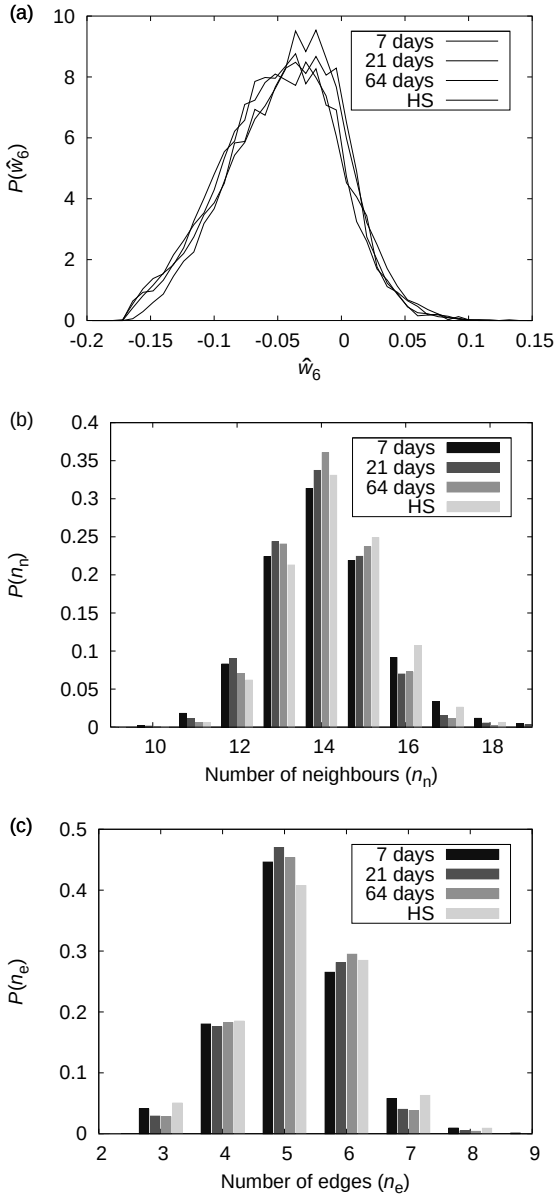

Figure 5.6: (a) Probability distribution of the bond-orientational order parameter $\hat{w}_6$, (b) probability distribution of the number of Voronoi neighbours per particle n_n and (c) probability distribution of the number of edges surrounding a Voronoi face n_e, for three long-range repulsive glasses and a hard-sphere glass (corresponding to the data points in Fig. 5.3b; for details see Fig. 5.5).

is remarkably similar. The distributions fall on top of each other within error. The differences between the long-range repulsive glasses at different waiting times were similar to the differences between two glasses from the same sample, imaged at the same day. Also, the difference between the long-range repulsive glasses and the hard-sphere glass is in the same range. We find good correspondence with the $\hat{w}_6$ distribution for the hard-sphere glass from literature [11].

In Fig. 5.6b we plotted the probability distribution $P(n_\mathrm{n})$ for the number of neighbours surrounding a particle. Since we used here the Voronoi construction to define the neighbours, this is the same as the number of faces of the Voronoi cell in which the particle is contained. Fig. 5.6c depicts the probability distribution $P(n_\mathrm{e})$ for the number of particles surrounding a bond, which is the same as the number of edges of the Voronoi face corresponding to this bond. These distributions are again very similar for the long-range repulsive glasses and the hard-sphere glass, and also very similar to the same distributions in Ref. [11].

Fig. 5.7 illustrates crystallisation in a long-range repulsive glass at one particular spot in the sediment, indicated in Fig. 5.2 by black squares. The configurations at $t = 21$ and 64 days were glassy; they correspond to the glasses in Figs. 5.5 and 5.6 at the same waiting times. At $t = 81$ days the system had crystallised. For comparison the hard-sphere glass is shown as well. On the left the colour of the particles is related to the bond-orientational order parameter $\bar{q}_6$: particles with low $\bar{q}_6$ are purple, particles with high $\bar{q}_6$ are red. On the right the particles were given a colour according to their crystallinity: crystalline particles are red and drawn at full size, fluid particles are cyan and (for clarity) drawn with a size equal to half their actual diameter. The $\bar{q}_6$ order parameter is a good measure for local bond order, it tends to higher values when the local order resembles bcc or fcc crystalline order and to lower values when the local order is glass- or fluid-like [36]. $\bar{q}_6$ includes the averaged bond order of the central particle and the particles in its first-neighbour shell (Section 5.2.3, Eq. 5.11), thereby directly depending on the positions of the particles in the second-neighbour shell. To average out the effect of thermal fluctuations [35], it was necessary to use the $\bar{q}_6$ instead of the more local q_6 order parameter, which depends only on the position of the particles in the first-neighbour shell. The reconstructions show that each glass (long-range repulsive and hard-sphere) had regions of high and low local bond order, and that, as expected, the regions containing crystalline particles had the highest local bond order. The reconstructions illustrate that the number of crystalline particles in the long-range repulsive glass very slowly increased in time until $t = 64$ days, and that the system at $t = 81$ days was almost fully crystalline. The local bond order in the long-range repulsive glasses closely resembled the local bond order in the hard-sphere glass.

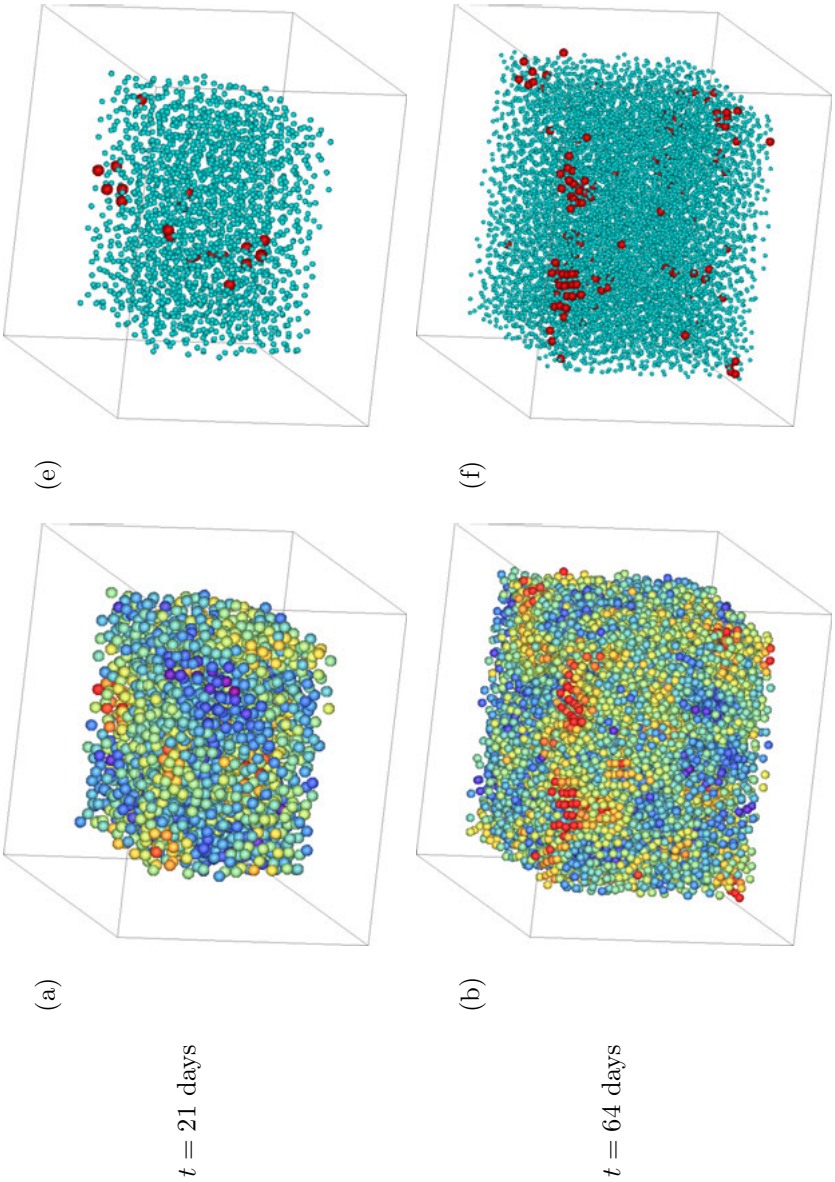
(e)
(f)
(a)
(b)
$t = 21$ days
$t = 64$ days

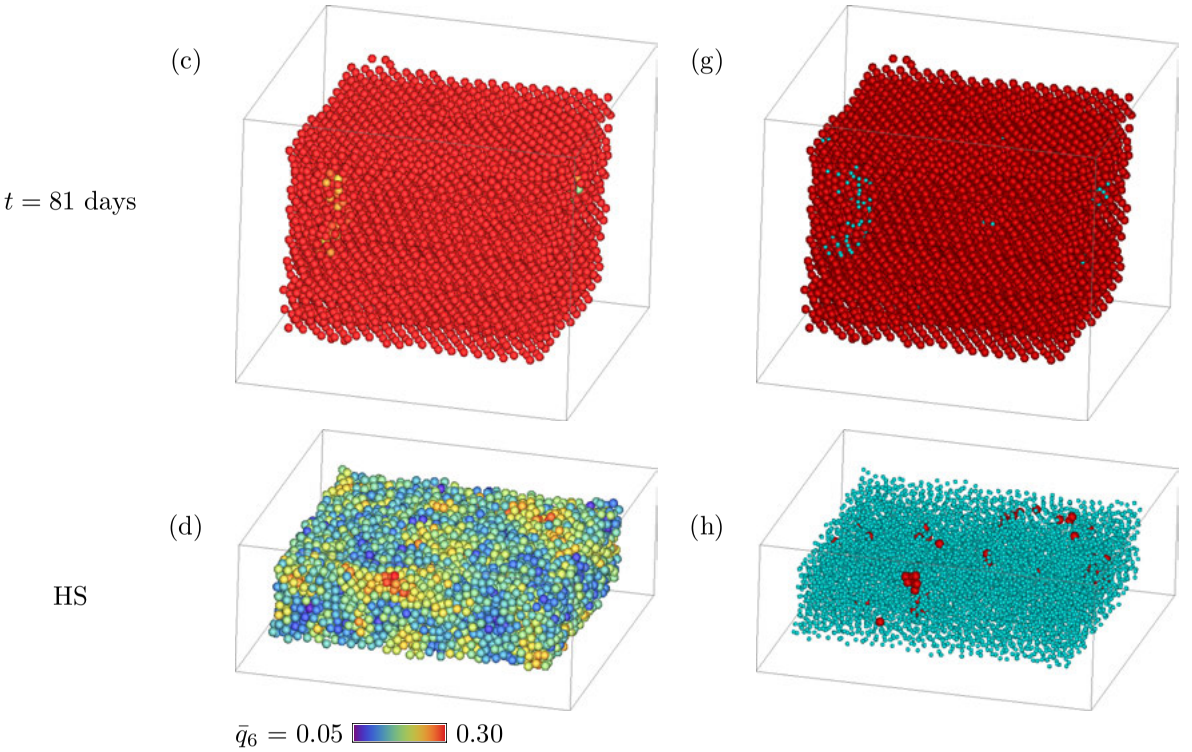

Figure 5.7: 3D reconstructions showing crystallisation in an initially glassy part of the sample at $t = 21$, 64 and 81 days and a hard-sphere glass (long-range repulsive configurations corresponding to the data points in Fig. 5.3b; $t = 81$ days, $\eta = 0.22$, $f_X = 0.98$, $f_{cl} = 0.01$; for details of the glassy configurations see Fig. 5.5). (a)–(d) Colour according to local bond order parameter $\bar{q}_6$; purple = low $\bar{q}_6$, red = high $\bar{q}_6$. (e)–(h) Same configurations as (a)–(d) but now red particles are crystalline, cyan particles are non-crystalline. For clarity, the diameter of the non-crystalline particles is equal to half the actual diameter.

5.3.4 Structural analysis of the crystals

The equilibrium phase diagram for colloidal systems interacting through a hard-core repulsive Yukawa pair potential contains two crystal phases; these are the body-centred-cubic (bcc) and the face-centred-cubic (fcc) crystal phase [26–28]. On going from low to high volume fraction, it is possible to find (i) a fluid phase followed by an fcc crystal phase (for small screening lengths) or (ii) a fluid phase, followed by a bcc crystal phase and then an fcc crystal phase (for larger screening lengths). The phases are separated by relatively narrow coexistence regions. In more recent work Yukawa phase diagrams were calculated under the constant-potential assumption and charge-regulation conditions [29], instead of for a fixed contact value of the interaction potential as before [26–28]. Again, the phase diagram contained fluid, bcc and fcc regions, but the crystals were stable in a much smaller part of the phase diagram. Discharging of the colloids with increasing volume fraction and decreasing salt concentration gave rise to a re-entrant fluid phase at high volume fraction and a stable fluid phase across the entire volume fraction range at low salt concentration.

For some combinations of Yukawa parameters the difference in free energy between an fcc crystal and a hexagonal-close-packed (hcp) crystal is very small [162], and it is not uncommon to find a random stacking of close-packed layers under conditions where the equilibrium crystal phase is fcc [117, 149, 163, 164]. This structure is referred to as the random-hexagonal-close-packed (rhcp) crystal.

The phase behaviour is determined by system parameters Z and $(\kappa\sigma)^{-1}$, and we can extract rough estimates for the system parameters from the observed phase behaviour.

We used the bond order parameter $\bar{w}_6$ to distinguish between particles that are in an fcc or hcp environment and particles that are in a bcc environment (similar to Ref. [35]). In an ideal crystal with only one type of lattice site, $\bar{w}_6$ will have the same value as $\hat{w}_6$, which is negative for fcc and hcp crystals (-0.0131 and -0.0124, respectively), and positive for bcc crystals (0.0131) [34]. On this basis we assumed that crystalline particles which had $\bar{w}_6 < 0$ were in an fcc, hcp or intermediate environment and crystalline particles which had $\bar{w}_6 > 0$ were in a bcc environment. In the following we will refer to fcc, hcp and in-between particles simply as fcc. The $\bar{w}_6$ distributions that we calculated for our crystalline systems indeed showed peaks close to one or both of these values, representing the most crystalline particles in the system. As mentioned above, we used $\bar{w}_6$ instead of $\hat{w}_6$ to reduce the effect of thermal fluctuations.

Up to $t = 7$ days the crystalline particles were predominantly bcc (Fig. 5.8a). At $t = 14$ and 21 days we found a mixture of bcc and fcc regions (Fig. 5.8b). The crystalline regions adjacent to the bulk glass phase (on the left side of the

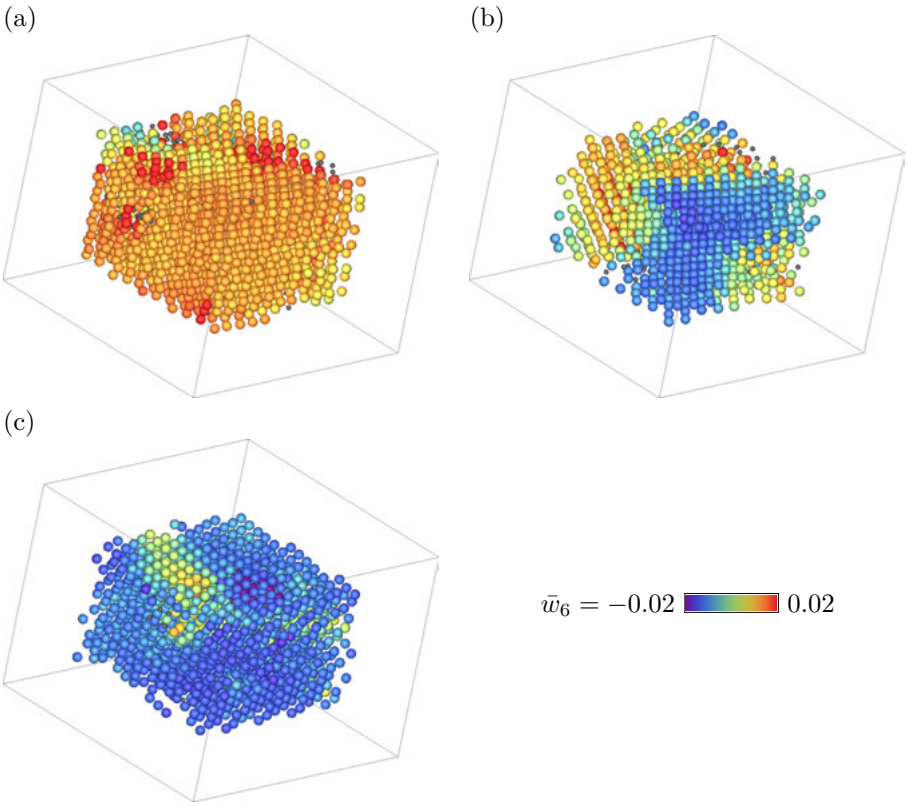

Figure 5.8: Crystalline configurations from Fig. 5.3c at (a) $t = 2$ days ($\eta = 0.18$, $f_{\mathrm{X}} = 0.91$, $f_{\mathrm{cl}} = 0.04$), (b) $t = 14$ days ($\eta = 0.13$, $f_{\mathrm{X}} = 0.97$, $f_{\mathrm{cl}} = 0.004$) and (c) $t = 35$ days ($\eta = 0.17$, $f_{\mathrm{X}} = 0.97$, $f_{\mathrm{cl}} = 0.02$). For the crystalline particles, the colour indicates value of bond order parameter $\bar{w}_6$; bcc-like particles are orange and fcc-like particles are blue; non-crystalline particles are grey and reduced in size (to half the actual diameter).

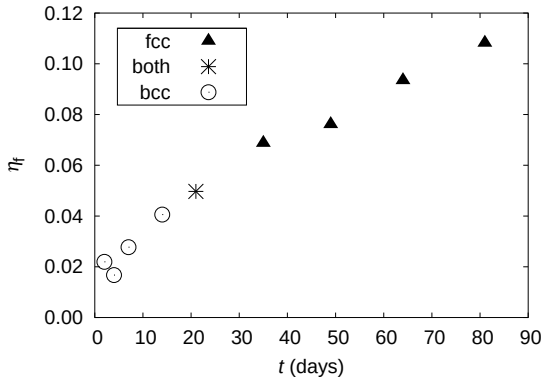

Figure 5.9: Freezing volume fraction η_f as a function of time t.

profiles in Fig. 5.2) or surrounding crystal defects, tended to contain more bcc particles. From $t = 35$ to 81 days the crystalline particles were predominantly fcc (Fig. 5.8c), except in a small region close to the bulk glass phase, where the majority of crystalline particles was bcc-like.

At each point in time after centrifugation the sample displayed fluid-crystal coexistence close to one end of the sediment (furthest from the water-CHB interface). In Fig. 5.9 we plotted the volume fraction at the fluid-crystal boundary (the freezing volume fraction η_f). We left out the data points for $t < 2$ days, because the particles were then still migrating towards the interface. We also indicated the crystalline environment of the majority of particles found close to the fluid interface. We found a fluid-bcc transition for $t \leq 14$ days and a fluid-fcc transition for $t \geq 35$ days.

The sample was crystalline across a broad volume fraction range (from η_f up to $\eta = 0.16$–0.21, where the system was glassy). For all waiting times the structure of the crystalline regions (bcc, mixed or fcc) was quite homogeneous across almost the entire crystalline part of the sediment. A systematic dependence of the crystal symmetry on the local volume fraction was not found. Most inhomogeneous with regard to crystal symmetry was the sample at $t = 14$ days, for which we found a fluid-bcc coexistence, but at higher volume fraction a mixture of bcc and fcc regions (Fig. 5.8).

Somewhere between $t = 14$ and 35 days the system changed from having a fluid-bcc to having a fluid-fcc transition, and therefore must have passed a triple point where the three phases (fluid, bcc and fcc) coexisted. We estimated the volume fraction of this triple point to be $\eta_t \approx 0.05$ and to occur around $t = 21$ days. The triple point of hard-core repulsive Yukawa systems can be well mapped onto

the triple point of point Yukawa systems [25, 28]. The value η_t is determined by a unique combination of particle surface potential ψ_0 (or charge number Z) and Debye screening length $(\kappa\sigma)^{-1}$. We calculate at the triple point: $(\kappa\sigma)^{-1} \approx 0.3$ and $\beta e\psi_0 \approx 2$, corresponding to a charge number of $Z \approx 8 \times 10^2$ [25, 28]. The increase of η_f in time and the change from fluid-bcc to fluid-fcc coexistence indicate a change of the particle interactions. When we assume a constant $(\kappa\sigma)^{-1} \approx 0.3$, the surface potential $\beta e\psi_0$ has to change from ~ 7 to ~ 1 in order to access the range of freezing volume fractions $\eta_f = 0.02$–0.11; corresponding charge numbers would be $Z \approx 3 \times 10^3$–4×10^2. When we assume the surface potential $\beta e\psi_0 \approx 2$ to be constant, the screening length $(\kappa\sigma)^{-1}$ has to vary between ~ 0.8 and ~ 0.1. These limiting values for $\beta e\psi_0$ and $(\kappa\sigma)^{-1}$ were calculated from the fit to the fluid-bcc phase boundary, given in Ref. [28] (see also Ref. [25]). In reality, presumably a combination of these two effects occurred.

We can use results from Ref. [29] to narrow down the estimate for $(\kappa\sigma)^{-1}$ in our system. Interactions are determined by $\beta\epsilon$ and $(\kappa\sigma)^{-1}$ (Eq. 5.1). For our system, $\beta e\psi_0 = 2$ and $\lambda_B/\sigma = 0.0032$, so, from Eq. 5.7, $\beta\epsilon = 3.1 \times 10^2$. In Ref. [29], with $\lambda_B/\sigma = 0.005$, $\beta\epsilon = 3.1 \times 10^2$ corresponds to $\beta e\psi_0 = 2.5$. In figures 3b and c of Ref. [29] the constant-potential and charge-regulated phase diagrams are plotted for $\beta e\psi_0 = 2$ and $\beta e\psi_0 = 3$; the phase diagram for $\beta e\psi_0 = 2.5$, which would correspond to our system, is intermediate between these two. The constant-potential phase diagram shows that for $\eta = 0.3$ the maximum $(\kappa\sigma)^{-1}$ at which the crystal still exists is ~ 0.6 and ~ 1.0, for $\beta e\psi_0 = 2$ and 3, respectively. For the charge-regulated phase diagram these values for the maximum $(\kappa\sigma)^{-1}$ at which the crystal still exists are higher. This means that even for the highest $(\kappa\sigma)^{-1}$ we estimated for our system ($(\kappa\sigma)^{-1} = 0.8$) no re-entrant melting is yet expected. However, for high $\beta e\psi_0$ and/or high η interactions are better described by an effective screening length. When we consider the phase diagram for $\beta e\psi_0 = 2$ plotted in terms of the effective screening length, as depicted in figure 5 of Ref. [29], we see that for $\eta = 0.3$ the maximum *effective* screening length at which the crystal still exists is ~ 0.4 for $\beta e\psi_0 = 2$ (the plot for $\beta e\psi_0 = 3$ is not shown, but the value for the effective screening length is presumably slightly larger than for $\beta e\psi_0 = 2$). As we did not observe re-entrant melting in our system, this finding indicates an upper limit for $(\kappa\sigma)^{-1}$. We conclude that the lowest $\eta_f = 0.02$ was at least partly due to a higher $\beta e\psi_0$ on the colloids. Below (Section 5.3.5) we argue that the assumption of a decreasing $(\kappa\sigma)^{-1}$ is necessary in order to account for the spontaneous cluster dissociation that was observed.

We note that close to the bulk glass phase we observed bcc crystals for samples with a fluid-fcc coexistence (for $t = 35$–81 days, as mentioned above). However, for $(\kappa\sigma)^{-1}$ below that of the triple point, bcc crystals do not exist across the entire volume fraction range [28, 29]. The observation of bcc crystals (close to the

bulk glass phase) and a fluid-fcc transition in the same sample, could be explained by slightly changing particle interactions as a function of distance from the water-CHB interface and/or a stabilisation of the bcc crystals with respect to fcc crystals by the adjacent amorphous bulk glass phase.

5.3.5 Origin of the attractions

To understand the origin of the cluster formation and the subsequent disappearance of the clusters better, we performed additional experiments. Instead of concentrating the system by centrifugation, we used an external electric field to bring particles into contact and observed the system after switching off the field.

When an electric field is applied to a colloidal suspension in which the dielectric constant of the particles is different from that of the suspending medium (here: at 1 MHz, $\epsilon_r = 2.6$ for PMMA, $\epsilon_r = 7.92$ for CHB), the particles acquire a dipole moment, causing them to align in strings parallel to the E-field. The total interaction between particles is a sum of the hard-core repulsive Yukawa interaction and an induced long-range dipolar interaction [19, 150, 155, 165–167].

Upon application of an AC external electric field (root-mean-square amplitude $E_{rms} = 0.4$ V µm^{-1}, frequency $f = 1$ MHz) to a suspension of our PMMA particles in CHB ($\eta \approx 0.02$), the particles assembled into strings parallel to the E-field direction (see Fig. 5.10a). We note that at some places inside the strings a small separation can be seen between two particles within the same string (Fig. 5.10b), due to the strong repulsive electrostatic force between particles. After a waiting time of 10 minutes, during which the E-field was on, we switched off the field and followed the breaking up of strings using confocal microscopy. Figs. 5.10c and d show this process for two different strings (lengths of five and four particles, respectively), located at different places in the sample, as indicated by the white rectangles in Fig. 5.10b. In the first series (Fig. 5.10c) the top particle of a string of five particles separated from the rest 45 seconds after switching off the E-field. A second particle (the bottom one) in the string separated after more than 2 minutes of observation. In the second series (Fig. 5.10d) a string of four particles divided into two dumbbells 81 seconds after the field was turned off. We could not follow the separation of the particles in the remaining dumbbells because the particles moved out of the plane of observation. After a long waiting time (one day in this case), all clusters had disappeared and only single particles were observed in the sample.

We seek the origin of the attractive interactions between the particles in the attractions between PMMA chains that also keep an uncross-linked particle together (mostly Van der Waals attractions). We think these attractions come into play when PMMA chains are brought into direct contact as the particles are pressed

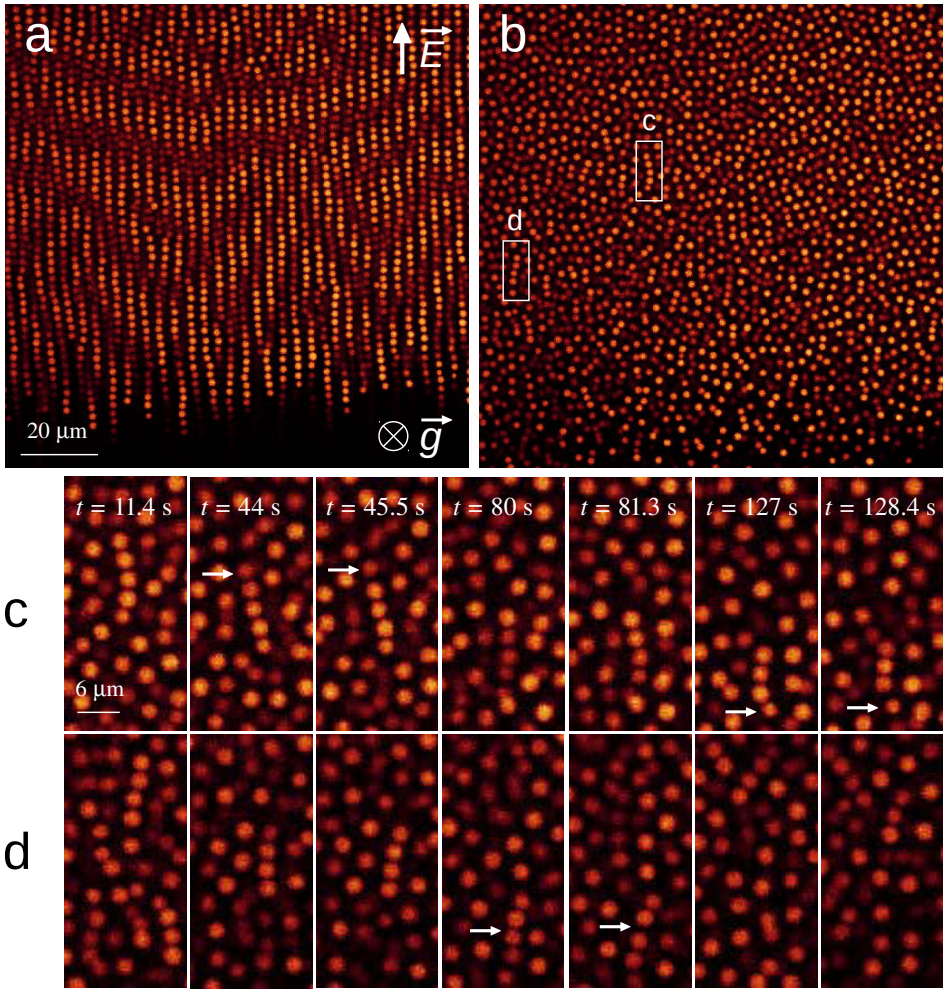

Figure 5.10: Confocal images of PMMA particles (σ = 2.23 µm) in CHB forming strings under an AC electric field. (a) PMMA strings after 10 minutes of waiting time. (b) The sample after switching off the E-field: small strings persisted for a certain time before breaking. Series (c) and (d) show the breaking process for two different strings of lengths five and four particles, respectively (indicated by the white rectangles in image (b)). In series (c) the top particle of the string separated from the rest 45 seconds after switching off the E-field, as indicated by the white arrows. A second particle (the bottom one) in the string separated after more than 2 minutes of observation. In series (d) the string divided into two dumbbells 81 seconds after the field was turned off. The corresponding movies are available in the supplementary information [95].

together by the centrifugal or electric field and are thus responsible for cluster formation in our systems.

The E-field experiments described in this section demonstrate that pressing particles together results in the formation of clusters and that, with time, the clusters spontaneously dissociate. The difference in timescale on which the clusters disappear (minutes to hours for the E-field versus several months for the centrifugation experiments) could be due to many different parameters, such as the force with which the particles were pressed together, the duration of the compression, the details of the particle interactions at close contact and further away, and the volume fraction ($\eta = 0.02$ versus up to $\eta = 0.64$).

The centrifugal field exerts a force of approximately 1×10^{-13} N on each particle (calculated from: particle volume $\times$ effective density $\times$ acceleration $= \pi\sigma^3/6 \times (d_{\mathrm{CHB}} - d_{\mathrm{PMMA}}) \times 15g$, with $\sigma = 2.23$ µm, $d_{\mathrm{CHB}} = 1.336$ g cm^{-3}, $d_{\mathrm{PMMA}} = 1.19$ g cm^{-3} and $g = 9.8$ m s^{-2}). Apparently, this field is sufficiently strong to push the particles not only through the double layer but also through the steric stabilising layer. The former is understandable as the force from the long-range repulsive potential at a distance of 10 nm between the surfaces of the two spheres is 1×10^{-12} N for interaction parameters of $(\kappa\sigma)^{-1} = 1.0$ and $\beta e\psi_0 = 2.0$, and several layers of particles are pressing down on the densest part of the sediment where the clusters are formed. With time, as the ionic strength increases and the double layer becomes more compressed, the repulsive potential becomes steeper and the resulting forces become strong enough to break up the clusters. For a double-layer thickness of $(\kappa\sigma)^{-1} = 0.1$ the repulsive forces at the same surface-to-surface interparticle distance of 10 nm, which is approximately twice the thickness of the steric stabilising layer, has increased to 6×10^{-12} N. We note that assuming a constant $(\kappa\sigma)^{-1}$ and decreasing ψ_0 to account for the observed range of freezing volume fractions would result in a decreasing force with time and would not explain the cluster dissociation.

5.4 Conclusions

Compression by centrifugation of a dilute suspension ($\eta \approx 0.02$) of charged PMMA colloids in CHB resulted in the formation of long-range repulsive glasses at volume fractions $\eta \gtrsim 0.16$. Crystallisation of the long-range repulsive glasses was prevented by the presence of small clusters (mostly dumbbells), which were formed during the centrifugation step. Spontaneous dissociation of the clusters brought the number of clustered particles down. For more than two months, the number of crystalline particles in the system ($\sim 25\%$ of the total number of particles) did not change, while the number of clustered particles decreased but settled at $\sim 13\%$. Only after $t = 81$ days did we find extensive crystallisation in the formerly glassy

parts of the system, with $\sim 88\%$ of the total number of particles crystalline and $\sim 3\%$ clustered.

A clustered fraction f_{cl} of 0.12 was sufficiently high to completely frustrate crystallisation in our system. In Chapter 3 we describe research where we used computer simulations to investigate the effect of size polydispersity in systems with $\beta e\psi_0 \approx 2$ and $(\kappa\sigma)^{-1} = 0.1$–$0.4$, comparable to the system used in the current chapter. We found that a polydispersity s of 0.13 frustrated crystallisation in parts of the system; for $s = 0.15$ this effect was stronger, resulting in a lower overall crystalline fraction. The non-crystalline parts were found to be glassy, judged from the very slow dynamics that they exhibited. We calculated the polydispersity separately for the crystalline and glassy parts; interestingly, the glassy parts had a higher polydispersity than the crystalline parts. This is similar to the results in the current work: the glassy parts have a higher f_{cl} than the crystalline parts. The difference is that in Chapter 3 crystallisation was frustrated by size polydispersity, while in the current work it is due to the presence of small clusters.

The system parameters changed in time causing the system to pass the fluid-bcc-fcc triple point around $t = 21$ days with $\eta_{\mathrm{t}} \approx 0.05$. From this we obtained rough estimates for the Debye screening length $(\kappa\sigma)^{-1} \approx 0.3$ and surface potential $\beta e\psi_0 \approx 2$ (charge number $Z \approx 8 \times 10^2$). To account for the observed range of freezing volume fractions $\eta_{\mathrm{f}} = 0.02$–0.11, we must assume that either the screening length or the surface potential (or both) have changed during the waiting period of 81 days.

Finally, it is truly surprising that we did not find any significant changes in the structure of the glass, despite the large range of volume fractions and changing system parameters. We compared to hard-sphere data, and found good agreement between the local bond-orientational order in the long-range repulsive glasses and the hard-sphere glass.

5.5 Acknowledgements

I am grateful to Djamel El Masri for performing the experiments described in Section 5.3.5. I would like to thank Gulşen Heessels-Gürboğa for synthesis of the PMMA particles, Johan Stiefelhagen for help with the locking procedure and Michiel Hermes for sharing his code for obtaining particle coordinates.

5.6 Appendix

5.6.1 High-density crystal phase and size segregation in uncompressed sample

To verify our hypothesis that crystallisation was frustrated by the presence of clusters, we prepared a sample of our PMMA particles ($\sigma = 2.23$ µm) in CHB in the same way as described in Section 5.2, but with a much higher volume fraction $\eta \approx 0.30$; as before, the sample was stored and imaged vertically with the water phase on top, but note that this time the sample was not centrifuged. This uncompressed sample should contain almost no clusters and thus, according to our hypothesis, be crystalline. As expected, only very few clusters were present and as a result the sample was indeed almost fully crystalline (Fig. 5.11a).

Interestingly, this sample provided us with a good example of size segregation, with a resulting polydisperse glass phase. In some places we found a crystal phase with low size polydispersity adjacent to a glass phase with high size polydispersity (Fig. 5.11b). Apparently, a small fraction of smaller particles was present in this sample, which mostly ended up in a polydisperse glass phase; some can also be found in the crystal (Fig. 5.11a). The smaller particles were formed by secondary nucleation during the particle synthesis and were not completely removed in this sample; these particles were not present in the samples described in the main text. The particles in the glass phase had a very low mobility and were not fluid-like.

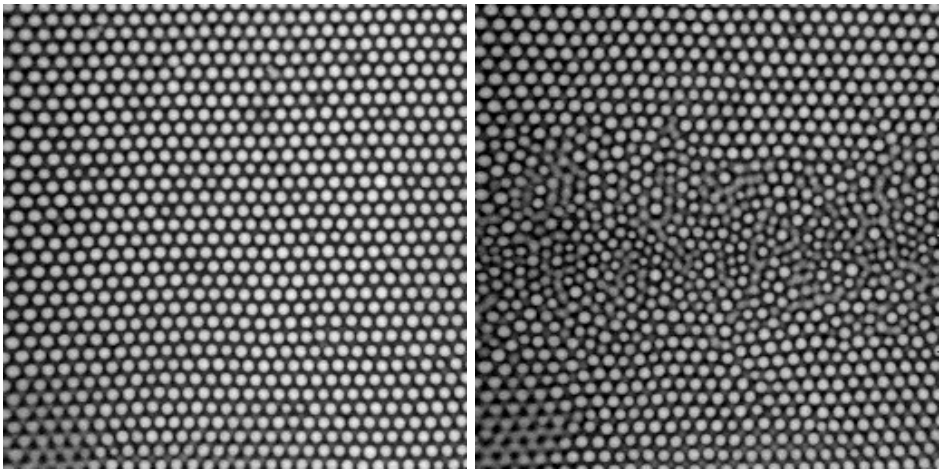

Figure 5.11: Crystal phase and polydisperse glass phase in a sample with initial volume fraction $\eta \approx 0.30$. When the sample was imaged a few hours after preparation, most of the sample was fully crystalline (left image). In some places size segregation took place, resulting in a crystal phase with low size polydispersity adjacent to a glass phase with high size polydispersity (right image). Both images (84.9 µm × 84.9 µm; taken $\sim$ 1 hour after sample preparation) were taken at the same xy position in the sample (2.1 mm from the water-CHB interface (x), in the middle of the width of the capillary (y)), but at a different z position: 25 µm (left image) and 40 µm (right image) from the front wall of the capillary. See Fig. 5.1 for a sample overview with x, y and z directions.

6

Experimental observation of the colloidal Brazil-nut effect in binary suspensions of long-range repulsive charged colloids

We studied experimentally the equilibrium sedimentation profiles in binary mixtures of micrometre-sized charged colloids (poly(methyl methacrylate); PMMA), which were dispersed in a low-polar solvent (cyclohexyl bromide; CHB) in order to arrive at double-layer thicknesses that are larger than the particle size. In a well-tuned experimental system we observed the colloidal Brazil-nut effect, an ordering of the particles contrary to what would be expected on the basis of their buoyant mass: in equilibrium the larger (heavier) particles stayed further from the surface onto which the particles sedimented than the smaller (lighter) particles. Our findings are in agreement with results from computer simulations and density-functional theory, predicting for long-range repulsive systems the Brazil-nut effect when the mass-per-charge for the heavier colloids is smaller than the mass-per-charge for the lighter colloids.

6.1 Introduction

When binary granular mixtures are shaken, under certain conditions larger particles in the mixture move to the top, while smaller particles travel downwards. This well-known phenomenon has been named the Brazil-nut effect, referring to the large Brazil nuts rising to the top of a mixture of nuts of different sizes when it is shaken [168, 169].

Density-functional theory [33, 170–172] and computer simulations [33, 172, 173] predict a *colloidal* Brazil-nut effect in binary mixtures of charged colloids at low salt concentrations, containing a lighter (1) and a heavier (2) colloidal species. By definition, the Brazil-nut effect occurs when $h_2 > h_1$, i.e. the mean height of the heavier colloids h_2 is larger than the mean height of the lighter colloids h_1. The colloidal phenomenon was named after the granular Brazil-nut effect only because a similar effect occurs: heavier particles float on top of the lighter ones. The colloidal Brazil-nut effect, however, has a different physical origin than its granular analogue, and is, contrary to the granular Brazil-nut effect, an equilibrium phenomenon.

The colloidal Brazil-nut effect finds its origin in the entropic lift effect [174] that causes the extended sedimentation profiles in suspensions of charged colloids at low salt concentrations [92, 118, 174, 175]. In the ideal-gas limit, when interparticle interactions can be neglected, the equilibrium sedimentation profile in a suspension of uncharged colloidal particles is well described by the barometric distribution. However, the situation is very different for a suspension consisting of charged colloids in a solvent at low salt concentrations [174]. For that type of system, the equilibrium sedimentation profile is much more extended than the barometric profile, i.e. the colloids reside at much higher altitudes than expected on the basis of their buoyant mass. This phenomenon is caused by delocalisation of the counterions, which is favourable as it increases the entropy of the system, and results in a charge separation in the system, inducing a macroscopic electric field. The colloids are pulled downwards by gravity and lifted upwards by the electric field. Adding salt reduces this lift effect, as in that case coions are available to maintain local charge neutrality, and the macroscopic electric field is reduced [174].

For an ideal-gas system, the equilibrium sedimentation profile in a *single-component* suspension of charged colloids at low salt concentrations can be analytically described by three regimes, namely, a barometric regime at low densities, a linear regime at intermediate densities, and an exponential regime with a large decay length at high densities [174]. The sedimentation profile is most conveniently

described in terms of the scaled colloid density y, defined by

$$y = \frac{Z\rho}{2c_\mathrm{s}} = \frac{3\eta Z}{c_\mathrm{s}\pi\sigma^3} = 24\eta\frac{\lambda_\mathrm{B}}{\sigma}\frac{Z}{(\kappa\sigma)^2}, \tag{6.1}$$

with σ the diameter and Z the charge number of the colloids, c_s the salt concentration, ρ the number density and $\eta = \pi\sigma^3\rho/6$ the volume fraction of the colloids, λ_B the Bjerrum length, given by

$$\lambda_\mathrm{B} = \frac{e^2}{4\pi\epsilon_\mathrm{r}\epsilon_0 k_\mathrm{B}T}\,, \tag{6.2}$$

with e the elementary charge, ϵ_r the dielectric constant of the solvent, ϵ_0 the dielectric permittivity of vacuum, k_B the Boltzmann constant and T the absolute temperature, and κ the inverse Debye screening length, given by

$$\kappa = \sqrt{8\pi\lambda_\mathrm{B}c_\mathrm{s}}\,. \tag{6.3}$$

The equilibrium sedimentation profile as a function of height z is then described by

$$y(z) = \begin{cases} y_0^{(1)}\exp\left(-\dfrac{z}{L}\right) & y < Z^{-1} \\ y_0^{(2)} - \dfrac{z}{ZL} & Z^{-1} < y < 1 \\ y_0^{(3)}\exp\left(-\dfrac{z}{(Z+1)L}\right) & y > 1 \end{cases}, \tag{6.4}$$

where L is the gravitational length, given by

$$L = \frac{k_\mathrm{B}T}{mg}\,, \tag{6.5}$$

with m the buoyant mass of the colloids and g the gravitational acceleration. For convenience, we take in this chapter the buoyant mass m and the height z to be positive, even for the case that the particles float; the wall towards which the particles sediment is located at $z = 0$. Regime 1, at low densities, is the familiar barometric regime: an exponentially decaying profile with the gravitational length L as decay length. Regime 2, at intermediate densities, is a linear regime, with slope $y'(z) = -1/(ZL)$. Regime 3, at high densities, is another exponential regime, with a larger decay length $(Z+1)L$.

The lift effect resulting in extended sedimentation profiles was found in the theoretical approach in Ref. [174] for an ideal-gas system in which interactions between the colloids were ignored. Later, the lift effect was confirmed in simula-

tions and theory that included colloid-colloid interactions. These studies used the primitive model [176, 177], which includes colloids and ions as separate species, or an effective one-component approach in which colloids interact through an effective screened Coulomb potential [177, 178] and ions are only taken into account through the Debye screening length. Agreement between the theory of Ref. [174] and experiments was found in Ref. [92]. The experiments in Refs. [118, 179] agreed with Ref. [119], which took into account charge regulation.

For mixtures of charged colloids, which contain more than one colloidal species, the same lift effect was found as in monodisperse suspensions [33, 170, 171]. In addition, the colloidal species were found to separate into layers, such that colloids with the same mass-per-charge m_i/Z_i (or the same value of Z_iL_i) are found at the same height [170]. Particles with the lowest m_i/Z_i are furthest from the surface onto which the particles sediment. From this ordering according to m_i/Z_i it follows that the Brazil-nut effect occurs for $Z_2/Z_1 \gtrsim m_2/m_1$, or $m_2/Z_2 \lesssim m_1/Z_1$, i.e. the mass-per-charge for the heavier colloids (2) is smaller than for the lighter colloids (1). The lift effect as well as the segregation into layers according to $\sim Z_iL_i$, which were found in Refs. [33, 170] for an ideal-gas system, have also been produced using an effective one-component approach [172] and primitive model simulations [173], both of which include interparticle interactions. In Ref. [172] reasonable agreement between theory and effective colloids-only simulations was found at low salt concentrations (in Ref. [172], for $\kappa\sigma \lesssim 1$–2), but not at high salt concentrations. The authors suggest that this is probably due to the fact that short-range correlations, which are more important in the high-salt case, are not described well by the theory. In Ref. [173] quantitative agreement was found between the Poisson-Boltzmann theory of Ref. [170] and primitive model simulations for low colloidal charge and low volume fraction (0.0095). Deviations between theory and simulations were found for higher volume fraction (0.115), with simulations yielding more extended density profiles. This was likely due to excluded volume effects, which were included in the simulations but not in the theory. Qualitative agreement was preserved: the lift effect resulting in sedimentation profiles more extended than expected on the basis of the buoyant mass of the particles was found, as well as the layering phenomenon with an ordering of colloidal species according to their mass-per-charge. We note that the effective colloids-only simulations in Ref. [172] did not result in more extended density profiles than obtained from the theory for both colloidal species; rather, for the higher-charged particles the simulations yielded a less extended profile than the theory, while for the lower-charged species the profile was more extended in the simulations than in the theory. Primitive model simulations [180] showed that in order to describe a binary charged colloidal mixture by an effective Yukawa potential, nonadditivity needs to be included. The sign of the nonadditivity was found to depend on the

system parameters, in particular charge asymmetry. While Refs. [33, 170] found the crossover to the Brazil-nut regime at $Z_2/Z_1 \approx m_2/m_1$ (for $m_2/m_1 = 1.5$ at $Z_2/Z_1 \approx 1.5$ [33] and $Z_2/Z_1 \approx 1.6$ [170]), in Ref. [172] the crossover was observed at a slightly higher charge ratio Z_2/Z_1 with respect to the mass ratio m_2/m_1 (for a system with $\kappa\sigma = 1.2$ and $m_2/m_1 = 2.0$ at $Z_2/Z_1 \approx 2.6$). In Ref. [172] the exact location of the crossover depended on the system parameters (the inverse screening length $\kappa\sigma$ and the buoyant masses of the particles).

In simulations and density-functional theory [181] the Brazil-nut effect was found in a two-dimensional binary mixture of particles with a long-range repulsive dipolar interaction. The more repulsive particles were surrounded by a zone from which the less repulsive particles were depleted. The buoyancy principle was still found to be valid when applied effectively, using the mass per volume of a particle plus its depletion zone. This result is in agreement with experimental findings in Ref. [182] on sedimentation in charged colloidal mixtures. However, in this experimental work no Brazil-nut effect was observed, presumably because the system parameters were not in the Brazil-nut regime. In Ref. [181] the depletion zone around the more repulsive particles resulted in an effective attraction of these particles to the hard bottom wall of the container, creating a layer of more repulsive particles on the container wall.

We observed the colloidal Brazil-nut effect in an experimental system of charged colloids in a low-polar solvent at low salt concentrations. We studied four binary systems, with different charge and mass ratios. Our findings support the prediction that in order for the Brazil-nut effect to occur, the mass-per-charge for the large colloids should be smaller than for the small colloids ($m_\mathrm{L}/Z_\mathrm{L} \lesssim m_\mathrm{S}/Z_\mathrm{S}$) [33, 170, 172, 173].

This chapter is organised as follows. In Section 6.2 we describe the model system, experimental procedure and data analysis, in Section 6.3 we discuss the results, and in Section 6.4 we present our conclusions.

6.2 Experimental methods

6.2.1 Model system

We used poly(methyl methacrylate) spheres (PMMA; density $d_\mathrm{PMMA} = 1.19$ g cm^{-3}; dielectric constant $\epsilon_\mathrm{r} = 2.6$; refractive index $n_\mathrm{D}^{25} = 1.492$ [18]), synthesised by dispersion polymerisation and sterically stabilised by a so-called comb-graft steric stabilising layer formed by poly(12-hydroxystearic acid) (PHSA) grafted onto a backbone of PMMA (PHSA-*g*-PMMA) [83]. We used four types of particles, of different average diameter and labelled with either the red fluorescent dye rhodamine isothiocyanate (RITC) or the green fluorescent dye 7-nitrobenzo-

2-oxa-1,3-diazol (NBD). The two smaller particles had average diameters of 1.30 and 1.58 µm, polydispersities of 4.0% and 3.5%, respectively, and were labelled with RITC, the two larger particles had average diameters of 1.98 and 2.87 µm, polydispersities of 3.5% and 2.4%, respectively, and were labelled with NBD. The average diameters and polydispersities were determined by static light scattering (SLS) for the two smaller particles and by scanning electron microscopy (SEM) for the two larger particles. To determine the average diameter and size polydispersity from the SEM images we measured ~ 100 particles from each batch using the program iTEM (Olympus Soft Imaging Solutions GmbH). We note that the SLS diameter is generally a few percent larger than the SEM diameter due to swelling of the particles as a result of solvent uptake. Some batches of particles underwent a so-called 'locking' procedure [85], in which the PMMA backbone of the steric stabiliser became covalently bonded to the particle surface; in the remainder of this chapter, these particles are referred to as 'locked'. In the case of 'unlocked' particles, the PHSA-*g*-PMMA stabiliser is simply adsorbed to the particle surface, but not covalently bonded to it. For more details the reader is referred to a recent work (Ref. [84]), investigating and characterising the PHSA-*g*-PMMA stabiliser and the chemistry involved in the locking step, which involves an additional heating step of the particles.

The particles were suspended in cyclohexyl bromide (CHB; Sigma-Aldrich; density $d_{\mathrm{CHB}} = 1.336$ g cm^{-3} [18]; dielectric constant $\epsilon_{\mathrm{r}} = 7.92$ [69]; refractive index $n_{\mathrm{D}}^{25} = 1.4935$ [18, 69]), which nearly matched the refractive index of the PMMA particles ($n_{\mathrm{D}}^{25} = 1.492$). This solvent is known to slowly and slightly decompose in time, a process which generates H^+ and Br^- ions [86]. To reduce the ionic strength, we cleaned the solvent before use [87], by bringing it into contact first with activated alumina ($\mathrm{Al_2O_3}$; 58 Å, ~ 150 mesh, Sigma-Aldrich) and then with molecular sieves (4 Å, 10–18 mesh, Acros Organics). The conductivity of CHB after the cleaning steps was on the order of 10 pS cm^{-1} (Scientifica 627 conductivity meter).

The pair interaction in a system of charged colloidal particles is commonly described by a hard-core repulsive Yukawa (screened Coulomb) potential [15, 16, 31, 39]:

$$\beta u_{ij}(r) = \begin{cases} \beta\epsilon_{ij} \dfrac{\exp\left[-\kappa(r-\sigma_{ij})\right]}{r/\sigma_{ij}} & r \geq \sigma_{ij} \\ \\ \infty & r < \sigma_{ij} \end{cases}, \tag{6.6}$$

with $\sigma_{ij} = (\sigma_i + \sigma_j)/2$ and the contact value of the potential between two colloids i and j:

$$\beta\epsilon_{ij} = \frac{Z_i Z_j}{(1+\kappa\sigma_i/2)(1+\kappa\sigma_j/2)} \frac{\lambda_{\mathrm{B}}}{\sigma_{ij}}, \tag{6.7}$$

where r is the centre-to-centre distance between particles i and j, Z_i (Z_j) and σ_i (σ_j) are the charge number and diameter of colloid i (j), λ_B is the Bjerrum length (Eq. 6.2), κ is the inverse Debye screening length (Eq. 6.3), and $\beta = 1/(k_B T)$. When the refractive index of the solvent closely matches that of the particles, as is the case in our experimental system, the Van der Waals interactions are much smaller than $k_B T$ and can be neglected.

6.2.2 Electrophoresis measurements

We measured the electrophoretic mobility μ of the particles at a volume fraction $\eta \approx 0.01$–0.02 using the method described in Chapter 2 (see also Ref. [46]). We used the theoretical work by Carrique et al. [89] (see also Ref. [46]) to calculate the electrostatic surface potential ψ_0 and charge number Z from the mobility. In this work a Kuwabara cell model is used to calculate ψ_0 and Z from the measured mobility μ for any given screening length κ^{-1} and volume fraction η by numerically solving the full Poisson-Boltzmann equation. An estimate for κ^{-1} was obtained from the measured conductivity of the solvent CHB (see below, Section 6.3.1). Details can be found in Chapter 2.

6.2.3 Sample preparation and confocal microscopy

We prepared suspensions with an overall volume fraction of $\bar{\eta} = 0.02$ or 0.07 and containing only one type of PMMA particle; note that upon sedimentation the local volume fraction η will be different from the overall volume fraction. We mixed equal volumes of the two suspensions and then transferred the resulting binary suspension to a borosilicate glass capillary (inner dimensions 5 cm × 1.0 mm × 0.10 mm ($x \times y \times z$); VitroCom) by dipping the capillary into the suspension. We also made samples by first dipping the capillary into one of the suspensions and then into the second suspension, adding an approximately equal volume of the second suspension; mixing of the two suspensions took place during the filling step across a distance of a few micrometres and afterwards by particle diffusion. The suspension occupied approximately two-thirds of the capillary; the remaining part was left empty (containing only air). The capillary was mounted on a microscope glass slide and both ends of the capillary were sealed with UV-curing optical adhesive (Norland no. 68), which also attached the capillary to the microscope glass slide. After curing the sample was turned upside down (i.e. with the capillary below the microscope glass slide), a step which caused the two particle species to mix by forming swirls while they sedimented to the opposite wall of the capillary (see e.g. Refs. [183–185]). The capillary was left to equilibrate for 1–2 days in this horizontal position with the z axis parallel to gravity, as shown in Fig. 6.1.

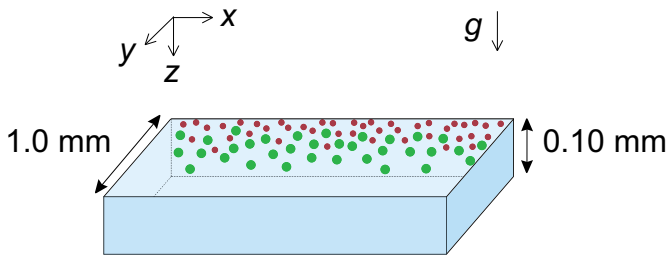

Figure 6.1: Schematic overview of the sample. x, y and z directions are indicated, as well as the direction of gravity (g). In reality particles were present across the entire width (y) of the capillary, but for clarity the particles are shown here only against the back wall (xz).

We used confocal microscopy (Nikon C1 or Leica SP2 confocal microscope) with a 63× NA 1.4 oil immersion objective (Leica), in fluorescence mode with 543 nm (RITC) and 488 nm (NBD) excitation and sequential scanning mode, to obtain three-dimensional stacks of images (typical stack: $128 \times 64 \times 300$ pixels ($x \times y \times z$); pixel size was in most cases 0.20 or 0.23 µm in xy and 0.23 or 0.24 µm in z; $\sim$ 2.7 or 6.2 frames per second). Fig. 6.1 is a schematic overview of the capillary with x, y and z directions and the direction of gravity (g) indicated. Stacks were taken at several positions along the length (x direction) of the capillary.

6.2.4 Data analysis

We obtained the positions of the particles using an algorithm as described in e.g. Refs. [11, 155], which is an extension to 3D of the 2D method described in Ref. [88].

From the particle coordinates we calculated the number density profile $\rho_i(z)$ (number density as a function of the distance z from the top wall of the capillary; see Fig. 6.1) for each type of particle i. In order to improve statistics, we averaged the profiles from 7 independent 3D stacks. We excluded particles that were adsorbed to the glass wall.

In order to quantify the colloidal Brazil-nut effect, we can define, after Ref. [33, 170], for each density profile $\rho_i(z)$ for colloid i a mean height

$$h_i = \frac{\int_0^\infty z\rho_i(z)\,\mathrm{d}z}{\int_0^\infty \rho_i(z)\,\mathrm{d}z}\,, \quad i = \mathrm{L,S}. \tag{6.8}$$

The colloidal Brazil-nut effect is defined as $h_L > h_S$, with h_L and h_S the respective mean heights of the large and small colloids.

6.3 Results and discussion

6.3.1 System parameters

Debye screening length

The conductivity of CHB after the cleaning steps was on the order of 10 pS cm^{-1}, which corresponds to an ionic strength of $c_s = 2.4 \times 10^{-10}$ mol L^{-1} (the ionic strength reduces for this case of a monovalent salt to the salt concentration c_s; note that the total ion concentration is $2c_s$). We used Walden's rule to obtain an estimate for the ionic molar conductances for H^+ and Br^- in CHB, which were needed in order to estimate the ionic strength from the measured conductivity. A Debye screening length $\kappa^{-1} \approx 6$ µm followed from Eq. 6.3. This calculation is described in more detail in Chapter 2.

It is possible that κ^{-1} was lower in the samples for which we observed the Brazil-nut effect (see Section 6.3.2). This might be due to an increase of the ionic strength in time due to decomposition of CHB (see Section 6.2.1).

Electrostatic surface potential and charge number

From the measured electrophoretic mobilities we obtained an estimate for the electrostatic surface potential ψ_0 and charge number per particle Z (see Chapter 2 for details on the procedure); the results are given in Table 6.1. In Chapter 2 we found that the surface potential for locked particles was higher than for unlocked particles and that the charge increased quadratically with the particle diameter. In Ref. [46] it was found for locked PMMA particles (diameter ≈ 1 µm) in a mixture of CHB and *cis*-decalin that at higher volume fractions ($\eta \gtrsim 0.04$; depending on the system) the charge decreased significantly (for $\eta \approx 0.13$ the charge was a factor of 1.5–2.0 lower than for $\eta \approx 0.02$). At low volume fractions ($\eta \lesssim 0.04$; depending on the system) the charge was approximately constant.

In order to calculate the surface potential and the charge number from the measured electrophoretic mobility we needed a value for the Debye screening length; we took $\kappa^{-1} \approx 6$ µm, which was obtained from the conductivity of CHB directly before use, as described above. We did not measure the electrophoretic mobility for the unlocked particles U29 and U13. As the surface potential seemed approximately independent of the particle diameter (Chapter 2), we assumed that the surface potentials of the particles U29 and U13 were similar to the surface

Table 6.1: Summary of the system parameters for the four binary systems. We report, for each particle, the average diameter σ as determined by static light scattering (SLS) or scanning electron microscopy (SEM), the type of fluorescent dye used to label the particle, whether the particle is locked or unlocked, and the dimensionless electrostatic surface potential $\beta e\psi_0$ as determined by electrophoresis ($T = 298$ K) and the charge on the particle Z, assuming a Debye screening length $\kappa^{-1} \approx 6$ µm; for each binary system, we give the mass ratio m_L/m_S, the charge ratio Z_L/Z_S between the large and small particles, and indicate whether we observed the colloidal Brazil-nut effect (BN) for that system. Values preceded by $\sim$ are estimates; see text for details.

Binary system	Particle	$\frac{\sigma}{\mu m}$	Dye	Locked?	$\beta e\psi_0$	$\frac{Z}{10^2}$	$\frac{m_L}{m_S}$	$\frac{Z_L}{Z_S}$	BN
1	U20	1.98	NBD	no	3.3	2.9	2.0	1.2	no
	U16	1.58	RITC	no	3.9	2.5			
2	L20	1.98	NBD	yes	4.2–5.7	4.5–7.9	2.0	1.8–3.2	yes
	U16	1.58	RITC	no	3.9	2.5			
3	U29	2.87	NBD	no	~ 3.6	~ 6.7	11	~ 4.7	no
	U13	1.30	RITC	no	~ 3.6	~ 1.4			
4	L29	2.87	NBD	yes	3.8–5.9	9.1–15.7	11	~ 6.4–11	no
	U13	1.30	RITC	no	~ 3.6	~ 1.4			

potentials on the particles U20 and U16, namely $\beta e\psi_0 \approx 3.6$. From this we calculated for particles U29 and U13 the charge numbers $Z_i = 6.7 \times 10^2$ and 1.4×10^2, respectively.

The charge numbers of the particles in the samples for which we observed the Brazil-nut effect might have been different from the charge numbers obtained from electrophoresis, due to charge regulation and differences in ionic strength, volume fraction and/or number ratio between the two species (see Section 6.3.2).

6.3.2 Colloidal Brazil-nut effect

Microscopic observations

We made four binary systems; their properties are summarised in Table 6.1. For each binary system we calculated the ratio m_L/m_S between the buoyant mass of the large particles m_L and that of the small particles m_S. We approximated this ratio by assuming the mass ratio is proportional to the volume ratio of the particles: $m_L/m_S = \sigma_L^3/\sigma_S^3$, with σ_L and σ_S the diameters of the large and small particles, respectively. This relation is exact for monodisperse particles of homogeneous mass density and provides a good estimate for our slightly polydisperse systems. We note that the diameters for the two smaller particles (1.30 and 1.58 µm) were

obtained by SLS and that corresponding SEM diameters are usually a few percent smaller [46, 83]. Also, the swelling of the particles due to solvent uptake depends on the solvent [46]. Using slightly different diameters for calculating the mass ratio would give a slightly different mass ratio, but would not change the conclusions in this work.

We also calculated the charge (number) ratio $Z_\mathrm{L}e/(Z_\mathrm{S}e) = Z_\mathrm{L}/Z_\mathrm{S}$, with e the elementary charge, $Z_\mathrm{L}e$ and $Z_\mathrm{S}e$ the respective charges of the large and small particles, and Z_L and Z_S the corresponding charge numbers. In choosing the particles for the binary mixtures, we exploited our observation that the locking state had a profound influence on the charge of the particles. Locked particles were generally crystalline at $\eta = 0.02$. In contrast, the same particles in the unlocked state at the same volume fraction ($\eta = 0.02$) were mostly fluid. For locked particles the equilibrium fluid-crystal coexistence is thus found at a lower volume fraction ($\eta < 0.02$) than for unlocked particles ($\eta > 0.02$). Assuming a similar value for the Debye screening length in the suspensions, this phase behaviour indicates that locked particles carry a higher charge than the same particles in the unlocked state. Electrophoresis measurements (Table 6.1) confirmed this hypothesis.

First, we consider binary systems 1 and 2, both of which have a mass ratio $m_\mathrm{L}/m_\mathrm{S} = 2.0$. According to the theoretical prediction in Refs. [33, 170], the occurrence of the Brazil-nut effect is expected for $Z_\mathrm{L}/Z_\mathrm{S} \gtrsim m_\mathrm{L}/m_\mathrm{S}$. Ref. [172] shows that when particle-particle interactions were taken into account, the crossover from the Brazil-nut to the non-Brazil-nut regime shifted to a higher charge ratio. For example, for a system comparable to our systems and with $m_\mathrm{L}/m_\mathrm{S} = 2.0$ the crossover was found at $Z_\mathrm{L}/Z_\mathrm{S} \approx 2.6 > m_\mathrm{L}/m_\mathrm{S}$. Since our system parameters were not very far from those in Ref. [172], this value is probably a reasonable estimate for our systems as well. For system 1, $Z_\mathrm{L}/Z_\mathrm{S} = 1.2$, which is smaller than $m_\mathrm{L}/m_\mathrm{S}$, and the Brazil-nut effect was not observed, in agreement with the predictions from theory and simulations. For system 2, $Z_\mathrm{L}/Z_\mathrm{S}$ varies between 1.8 and 3.2, depending on the sample. The charge ratio was close to that at which the crossover to the Brazil-nut effect is predicted: for $Z_\mathrm{L}/Z_\mathrm{S} \approx m_\mathrm{L}/m_\mathrm{S} = 2.0$ [33, 170] or, more likely, for $Z_\mathrm{L}/Z_\mathrm{S} \approx 2.6 > m_\mathrm{L}/m_\mathrm{S}$ (note that the crossover value depends on the system parameters, such as the inverse screening length $\kappa\sigma$, the buoyant masses m_L and m_S of the particles [172], and presumably also on the charges Z_L and Z_S of the particles). This means only slight changes in the charge ratio would be sufficient to change the system's behaviour from Brazil-nut to non-Brazil-nut. Indeed, we found that this system in some cases did and in other cases did not display the Brazil-nut effect, again in agreement with the theory and simulations.

Next, we consider binary systems 3 and 4, both of which have a mass ratio $m_\mathrm{L}/m_\mathrm{S} = 11$. Our estimates for the charge ratio $Z_\mathrm{L}/Z_\mathrm{S}$ are ~ 4.7 for system 3 and $\sim$ 6.4–11 for system 4. For the Brazil-nut effect to occur, the ratio $Z_\mathrm{L}/Z_\mathrm{S}$

should be at least 11 [33, 170], but probably larger [172]. The observations for systems 3 and 4 (no Brazil-nut effect) are thus also consistent with theory and simulations.

Fig. 6.2 shows confocal images that were taken for a sample with overall volume fraction $\bar{\eta} = 0.02$ containing system 2, which exhibited the Brazil-nut effect. The sample was prepared by adding two single-species suspensions separately to the capillary (see Section 6.2.3). Images were taken a few hours after sample preparation; since preparation the sample had been kept in the same position as during imaging. Images were taken approximately in the middle of the 5 cm long capillary, where both large (green) and small (red) particles were present in significant amounts.

Fig. 6.2a is an xz cross section of the capillary. The green particles at the top of the image are adsorbed to the top wall of the capillary; the bottom wall is not visible in the image. Gravity points downwards; the particles, however, sediment upwards, as they have a lower mass density ($d_{\mathrm{PMMA}} = 1.19$ g cm^{-3}) than the solvent ($d_{\mathrm{CHB}} = 1.336$ g cm^{-3}). We see that the large green particles ($L_{\mathrm{L}} = 0.71$ µm) are further from the top wall than the small red particles ($L_{\mathrm{S}} = 1.39$ µm); thus, the particles are not ordered such that the particles having the smallest gravitational length (largest mass) are closest to the wall, which is what would be expected for uncharged particles. Theory that ignores colloid-colloid interactions [33, 170], predicts that charged particles are ordered according to their mass-per-charge m_i/Z_i, with particles with the lowest mass-per-charge furthest from the wall towards which the particles sediment (here: the top wall). Results for low salt concentrations from simulations using the primitive model [173] or an effective screened Coulomb potential [172], which take into account colloid-colloid interactions, were in reasonable agreement with the theory. Since in the present case the large green particles are furthest from the top wall, it must be that $m_{\mathrm{L}}/Z_{\mathrm{L}} \lesssim m_{\mathrm{S}}/Z_{\mathrm{S}}$, and $Z_{\mathrm{L}}/Z_{\mathrm{S}} \gtrsim m_{\mathrm{L}}/m_{\mathrm{S}}$ or $Z_{\mathrm{L}}/Z_{\mathrm{S}} \gtrsim 2.0$–$2.6$ [33, 170, 172, 173], in agreement with the electrophoresis results in Table 6.1.

Figs. 6.2b–f are xy confocal images, taken parallel to the top wall of the capillary, spaced 12 µm apart, starting 8 µm from the top (Fig. 6.2b). Again, it is clear that the small red particles are closer to the top wall than the large green particles. Furthermore, the small particles have a smaller interparticle spacing than the large particles, consistent with a higher charge on the large particles.

Density profiles

As described above, for system 2 we observed the Brazil-nut effect in some of our samples. Fig. 6.3 shows two density profiles for two samples containing system 2, at two different overall volume fractions, $\bar{\eta} = 0.02$ (Fig. 6.3a) and $\bar{\eta} = 0.07$ (Fig. 6.3b).

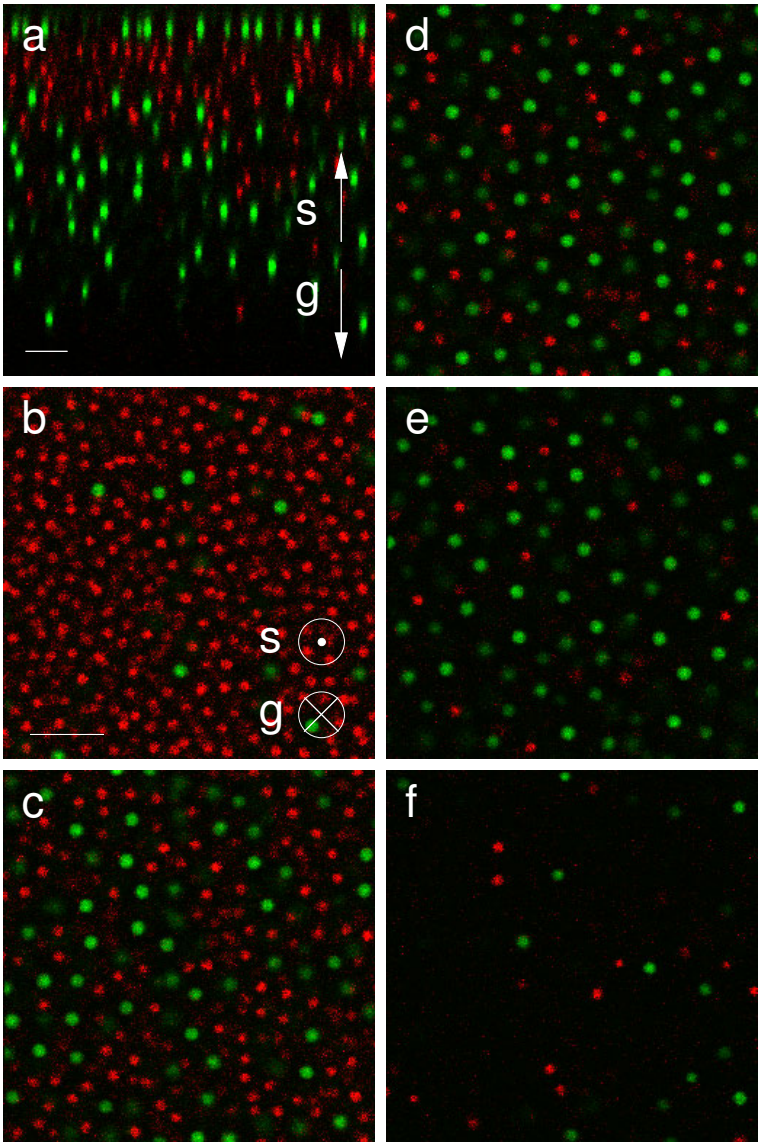

Figure 6.2: Colloidal Brazil-nut effect in a binary suspension of large (green) and small (red) particles (corresponding to system 2 in Table 6.1; overall volume fraction $\bar{\eta} = 0.02$). Gravity (g) points downwards, but direction of sedimentation (s) is upwards, as mass density of the PMMA particles is lower than that of the solvent CHB. (a) xz confocal image showing that the large (green) particles stay underneath the small (red) particles. (b)–(f) Sequence of xy confocal images taken from top to bottom (spaced 12 µm apart; first one taken 8 µm from the top). Scale bars indicate 10 µm. See Fig. 6.1 for an overview of the capillary.

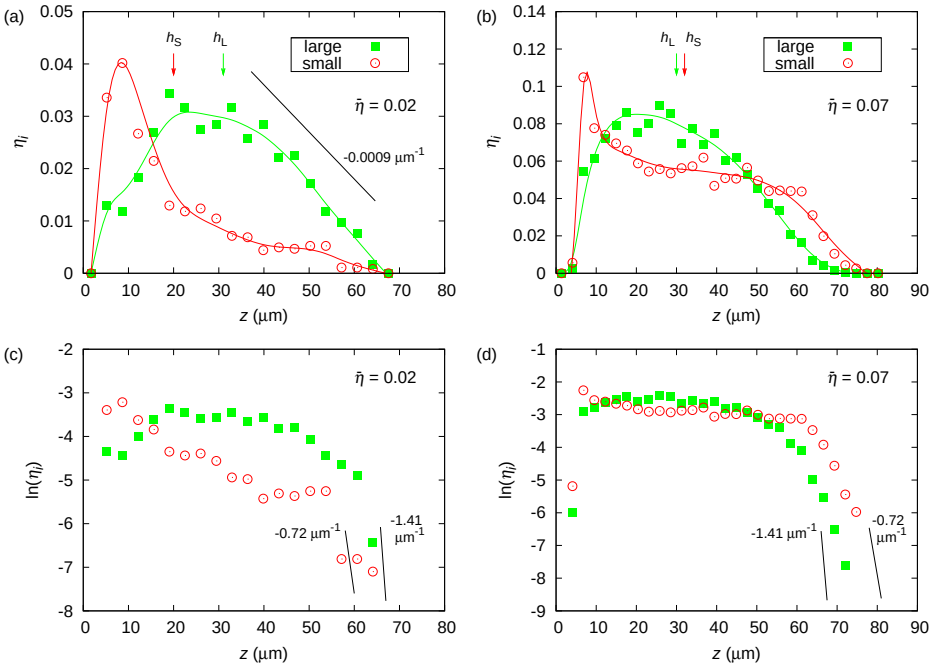

Figure 6.3: Density profiles (volume fraction η_i versus distance z from the top wall of the capillary) for large (green) and small (red) particles in two systems (corresponding to system 2 in Table 6.1) with overall volume fractions (a) $\bar{\eta} = 0.02$ and (b) $\bar{\eta} = 0.07$. The solid lines through the data points are meant to guide the eye. The data points are an average of 7 stacks. The arrows indicate the mean heights h_L and h_S of the large and small particles (Eq. 6.8). The straight solid line and label indicate the slope $\eta_L'(z)$, from which we tried to obtain $Z_L/(\kappa\sigma_L)$ (Eq. 6.9) [170]. (c) and (d) show the same data on a semilogarithmic plot ($\ln(\eta_i)$ versus z). The solid lines and their labels indicate the slopes $\ln(\eta_i(z))' = -1/L_i$ expected theoretically [33, 174] (see Eq. 6.4), calculated from $L_L = 0.71$ µm and $L_S = 1.39$ µm. See Fig. 6.1 for an overview of the capillary; the wall onto which the particles sediment is located at $z = 0$.

The density profiles were calculated through $\eta_i(z) = \pi\sigma_i^3\rho_i(z)/6$, where $\eta_i(z)$ and $\rho_i(z)$ are the volume fraction and the number density as a function of the distance from the wall z. Images were taken two and one days, respectively, after sample preparation; since preparation the samples had been kept in the same position as during imaging. We excluded particles that were adsorbed to the wall from our analysis. We note that in Ref. [181] an attraction was found of the large particles to the hard wall onto which they sediment, resulting in the formation of a boundary layer of large particles along the wall. In our case, the (positively charged) particles were attracted to the (negatively charged) wall by electrostatic interactions. As we cannot distinguish this electrostatic attraction from the attraction in Ref. [181], it is not possible for us to establish if the boundary layering effect observed in Ref. [181] also occurred in our samples.

We calculated the mean height h_i for each species, given by Eq. 6.8. For the $\bar{\eta} = 0.02$ sample we found $h_\mathrm{L} = 31$ µm and $h_\mathrm{S} = 20$ µm (as indicated in Fig. 6.3a); for the $\bar{\eta} = 0.07$ sample we found $h_\mathrm{L} = 30$ µm and $h_\mathrm{S} = 32$ µm (as indicated in Fig. 6.3b). The gravitational lengths for the two species were $L_\mathrm{L} = 0.71$ µm and $L_\mathrm{S} = 1.39$ µm. For uncharged colloids in the dilute limit a barometric profile is expected, with $h_i = L_i$ [170]; at higher densities, hard-core interactions would yield a more extended profile, but one would expect h_i to be on the order of L_i [172, 173]. For our systems the profiles were far more extended, with $h_i \gg L_i$, as would be expected for charged particles [172, 173].

The Brazil-nut effect is defined as the situation where $h_\mathrm{L} > h_\mathrm{S}$. For the $\bar{\eta} = 0.02$ sample, clearly $h_\mathrm{L} > h_\mathrm{S}$, as was already found qualitatively in the confocal microscopy images. Therefore, this is a good example of the Brazil-nut effect. For the $\bar{\eta} = 0.07$ sample we found $h_\mathrm{L} \approx h_\mathrm{S}$: this sample is approximately at the transition between Brazil-nut effect and no Brazil-nut effect. From these observations we conclude that in the $\bar{\eta} = 0.02$ sample, it must be that $Z_\mathrm{L}/Z_\mathrm{S} \gtrsim 2.0$–$2.6$, while in the $\bar{\eta} = 0.07$ sample, most likely $Z_\mathrm{L}/Z_\mathrm{S} \approx 2.0$–$2.6$ [33, 170, 172, 173]. Here we assumed that the crossover between the Brazil-nut and non-Brazil-nut regimes occurs at $Z_\mathrm{L}/Z_\mathrm{S} \approx m_\mathrm{L}/m_\mathrm{S} = 2.0$, which was predicted theoretically for an ideal-gas system [33, 170] at low salt concentrations, or at a crossover charge ratio $Z_\mathrm{L}/Z_\mathrm{S} \approx 2.6$, which was found for a system similar to our systems in Ref. [172] in simulations using an effective-potential approach. Since the exact value depends on the system parameters the range 2.0–2.6 should be taken as a rough estimate. We note that in the $\bar{\eta} = 0.07$ sample, where locally the volume fraction can be larger than 0.10, hard-core effects probably played a role.

In the $\bar{\eta} = 0.07$ sample corresponding to Fig. 6.3b the smaller particles are the dominant species close to the capillary wall (small z) and at the other end of the sediment (large z). A possible explanation could be that the charge on the particles was not constant, but depended on the volume fraction and/or the

number ratio of large and small particles. In Ref. [119] it was shown that the experimental results of Ref. [118] (sedimentation profiles in dispersions containing one colloidal species) were much better described when charge regulation was taken into account, resulting in a height-dependent charge. This was especially true for a large Debye screening length (on the order of or larger than the particle diameter), as was the case in our systems. Presumably, charge regulation also played a role in our systems. The charges thus might have been different from the charges obtained from electrophoresis measurements (Table 6.1). However, assuming that the Brazil-nut effect occurred for $Z_\mathrm{L}/Z_\mathrm{S} \gtrsim 2.0$–$2.6$ [33, 170, 172, 173], the charge ratio was still in the same range as obtained from electrophoresis results.

The $\bar{\eta} = 0.02$ sample corresponding to Fig. 6.3a was prepared from two single-component suspensions which were added separately to the capillary (see Section 6.2.3); mixing took place during the filling of the capillary across a distance of a few millimetres and by diffusion of the particles. As expected, this sample and other samples prepared in the same way were less homogeneous than samples prepared from a premixed binary suspension (see Section 6.2.3): the number ratio of the large and small particles varied between the data sets within the range 0.4–2.2 for the sample in Fig. 6.3a (separate suspensions), while it was in the range 0.5–0.6 for the sample in Fig. 6.3b (premixed binary suspension). Despite the locally varying number ratio for the sample in Fig. 6.3a, we observed the Brazil-nut effect for all data sets from this sample.

According to Ref. [170], the slope in the part of the sample where one species is dominant is given by the slope from the one-component approach [174], which, provided we are in the linear regime of the profile and we can neglect interparticle interactions, is given by

$$\eta'(z) = y'(z)\frac{\sigma}{24\lambda_\mathrm{B}}\frac{(\kappa\sigma)^2}{Z} = -\frac{\sigma}{24\lambda_\mathrm{B}L}\frac{(\kappa\sigma)^2}{Z^2}, \tag{6.9}$$

where we used $y'(z) = -1/(ZL)$, the slope from the linear regime (regime 2) in Eq. 6.4. The theoretical approach in Ref. [170] did not take into account interactions between the colloids. Nevertheless, reasonable to good agreement was found between the theory of Ref. [170] and simulations using an effective screened Coulomb potential [172] or the primitive model [173], both of which included interparticle interactions. We note, however, that in Ref. [172] effective-potential simulations yielded a slope for the higher-charged species which was larger than the slope obtained from the theory, while in Ref. [173] the profiles obtained from primitive model simulations were more extended (smaller slope) than those from the theory. In Ref. [92] good agreement was found between the one-component version of the theory [174] and experiments in one-component systems very similar to ours. Therefore, we tried if Eq. 6.9 yielded reasonable values for the parameters

in our binary systems. In the $\bar{\eta} = 0.07$ sample (Fig. 6.3b) there was no clear region where one species was dominant; in the $\bar{\eta} = 0.02$ sample (Fig. 6.3a) we can identify a linear part of the profile for the large particles in a region with predominantly large particles. We indicated the approximate steepness of this slope ($\eta_{\mathrm{L}}'(z) \approx -0.0009\ \mu\mathrm{m}^{-1}$) in Fig. 6.3a. This slope corresponds to a ratio $Z_{\mathrm{L}}/(\kappa\sigma_{\mathrm{L}}) \approx 1.4 \times 10^2$ (Eq. 6.9); this is much smaller than the value we find from the measured charge number ($Z_{\mathrm{L}} \approx 6.2 \times 10^2$, average of range in Table 6.1) and dimensionless screening length ($(\kappa\sigma_{\mathrm{L}})^{-1} \approx 6\ \mu\mathrm{m}/(2\ \mu\mathrm{m}) \approx 3$) obtained from the conductivity of CHB, which yield $Z_{\mathrm{L}}/(\kappa\sigma_{\mathrm{L}}) \approx 1.9 \times 10^3$. It is reasonable to assume a screening length smaller than the value corresponding to the initial conductivity of CHB, as the ionic strength in our systems increased due to decomposition of CHB (see Section 6.2.1). A screening length of order $(\kappa\sigma_{\mathrm{L}})^{-1} \approx 1$ would be in agreement with other experimental work on similar particles, where we estimated the screening length a few days after sample preparation from the phase behaviour of the suspension (Chapter 5); in that case the suspension was prepared using cleaned CHB with a similarly low conductivity as in the present work. However, assuming $Z_{\mathrm{L}}/(\kappa\sigma_{\mathrm{L}}) \approx 1.4 \times 10^2$ (from Eq. 6.9) would yield a value for the charge number $Z_{\mathrm{L}} \approx 1.4 \times 10^2$, which is much smaller than the values obtained from electrophoresis (Table 6.1). Even if we assume a smaller slope (e.g. $\eta_{\mathrm{L}}'(z) \approx -0.0003\ \mu\mathrm{m}^{-1}$; estimated after Ref. [172]), this would give $Z_{\mathrm{L}}/(\kappa\sigma_{\mathrm{L}}) \approx 2.3 \times 10^2$ and $Z_{\mathrm{L}} \approx 2.3 \times 10^2$, which is still quite small compared to the electrophoresis results. As mentioned above, the charge on the particles was likely subject to charge regulation, and therefore possibly different from the charges obtained from electrophoresis measurements. Given the uncertainty about the values of Z_{L} and $\kappa\sigma_{\mathrm{L}}$ in the binary mixtures, it is not clear if it is possible to obtain a reliable estimate of the system parameters from Eq. 6.9. Since the theory behind Eq. 6.9 [174] neglects interparticle interactions, which may influence the slope [172, 173], Eq. 6.9 might not be valid for our systems. Also, in Ref. [170] Eq. 6.9 could be applied to dilute mixtures in places where one species was dominant; however, the segregration into layers was in our case not as strong as in Refs. [170] and [172]. Finally, charge regulation likely played a role in our systems, which would make the assumption of constant charge invalid.

The length of the linear regime is on the order $Z_i L_i$ [174], which for the large particles ($L_{\mathrm{L}} = 0.71\ \mu\mathrm{m}$) is larger than the height of the capillary (0.10 mm) when $Z_{\mathrm{L}} > 1.4 \times 10^2$. Since the charge in our systems is presumably higher, this means we could not observe the slowly decaying exponential regime in our samples (a situation comparable to that in Ref. [92]) and we tried to apply Eq. 6.9 indeed in the linear regime.

In Figs. 6.3c and d the same profiles as in Figs. 6.3a and b are plotted on a semilogarithmic scale. We indicated with lines the expected slopes for the ba-

rometric regime of the profiles $\ln(\eta_i(z))' = -1/L_i$ (see Eq. 6.4). For system parameters $Z_L = 2.3 \times 10^2$ and $(\kappa\sigma_L)^{-1} \approx 1$ the barometric regime applies for $\eta_L(z) < 2 \times 10^{-4}$ (or $\ln(\eta_L(z)) < -8.5$; Eq. 6.4) [174]. Unfortunately, we do not have enough statistics in the barometric regime to see if the profiles agree with the theory.

It is possible that, due to charge regulation and differences in the ionic strength, the volume fraction and/or the number ratio between large and small particles, the charges on the particles were different from those measured in electrophoresis. Also, the Debye screening length was probably smaller than calculated from the initial conductivity of the solvent CHB, as the ionic strength in our systems is known to increase in time due to decomposition of CHB (see Chapter 2). Indeed, observations indicated that the system parameters were not constant. For example, we noticed that the large particles in the binary suspension seemed lower charged (fluid instead of crystalline, more sedimentation, smaller interparticle spacing) than in a suspension containing only large particles. Possibly, adsorbed ions moved from the large particles to the small particles, reducing the charge of the former and increasing the charge of the latter. This process would reduce the probability of observing the Brazil-nut effect, since that required the charge ratio Z_L/Z_S for this system to stay larger than $\sim$ 2.0–2.6 [33, 170, 172, 173]. In addition, we observed that after some time ($\sim$ days) the Brazil-nut effect disappeared. This indicates that the charges on the particles were changing in time (such that the charge ratio decreased, taking the system to the non-Brazil-nut regime, most likely for $Z_L/Z_S \lesssim$ 2.0–2.6 [33, 170, 172, 173]). Alternatively, a sufficient decrease of the Debye screening length would also result in a disappearance of the Brazil-nut effect (in Ref. [172] for $\kappa\sigma \gtrsim 2.4$, but this value depends on the system parameters m_L and m_S [172] and presumably also on Z_L and Z_S). Furthermore, the electrophoresis results in Table 6.1 indicate that the charge ratio was such, that slight changes in the charges on the particles could take the system from the Brazil-nut regime ($Z_L/Z_S \gtrsim$ 2.0–2.6) to the non-Brazil-nut regime ($Z_L/Z_S \lesssim$ 2.0–2.6), or vice versa. Indeed, sometimes we obtained a clear Brazil-nut effect (with $h_L > h_S$; Fig. 6.3a), while other samples contained a system at the transition between Brazil-nut effect and no Brazil-nut effect (for which $h_L \approx h_S$; Fig. 6.3b) or a system that showed no Brazil-nut effect. Probably, differences in the charge ratio as a result of varying ionic strength, volume fraction and/or number ratio between the samples were responsible for this diverse behaviour.

6.4 Conclusions

We observed experimentally the colloidal Brazil-nut effect in a binary suspension of charged particles (poly(methyl methacrylate); PMMA) in a low-polar sol-

vent (cyclohexyl bromide; CHB): in a well-tuned experimental system the large (heavier) particles stayed further from the surface onto which the particles sedimented than the small (lighter) particles. According to theory and simulations [33, 170, 172, 173] charged particles are ordered according to their mass-per-charge, rather than their mass, with particles with higher mass-per-charge closer to the surface onto which the particles sediment. This implies that in order for this Brazil-nut effect to occur the mass-per-charge for the large particles should be lower than for the small particles ($m_\mathrm{L}/Z_\mathrm{L} \lesssim m_\mathrm{S}/Z_\mathrm{S}$), or, put differently, the charge ratio between large and small particles should be larger than the mass ratio ($Z_\mathrm{L}/Z_\mathrm{S} \gtrsim m_\mathrm{L}/m_\mathrm{S}$). This is indeed what we found. We obtained the charges of the particles from electrophoresis measurements. For the three systems that did not display the Brazil-nut effect we found $Z_\mathrm{L}/Z_\mathrm{S} \lesssim m_\mathrm{L}/m_\mathrm{S}$, while for the system that in some cases did and other cases did not display the Brazil-nut effect, we found both $Z_\mathrm{L}/Z_\mathrm{S} \lesssim m_\mathrm{L}/m_\mathrm{S}$ and $Z_\mathrm{L}/Z_\mathrm{S} \gtrsim m_\mathrm{L}/m_\mathrm{S}$. Our observations are in agreement with results from theory and simulations for this system.

From the slope of the profile of the large particles in the linear regime we tried if it was possible to extract a value for the ratio $Z_\mathrm{L}/(\kappa\sigma_\mathrm{L})$ between the charge number Z_L of the large particles and the inverse dimensionless Debye screening length $\kappa\sigma_\mathrm{L}$. This ratio was much smaller (factor of ~ 10) than the ratio of independently obtained values for Z_L (from electrophoresis measurements) and $\kappa\sigma_\mathrm{L}$ (from conductivity measurements). The inverse screening length $\kappa\sigma_\mathrm{L}$ might have increased due to decomposition of the solvent CHB, which generates ions. Observations indicated that the charge on the particles in our systems was not constant, but subject to charge regulation, and therefore a function of ionic strength, volume fraction and/or number ratio between the two species. Therefore, the charge number Z_L might have been different from the values measured in electrophoresis measurements. Given the uncertainty about the values of Z_L and $\kappa\sigma_\mathrm{L}$ in the binary mixtures, it is not clear if the ratio obtained from the slope is reliable.

In future work it would be interesting to try to obtain system parameters through a direct comparison between experiments and theory or simulations, preferably using a constant-surface-potential or charge-regulation approach, instead of a constant-charge assumption. Varying the size ratio and/or charge ratio closer to the location of the expected crossover to the Brazil-nut regime (at $Z_\mathrm{L}/Z_\mathrm{S} \approx m_\mathrm{L}/m_\mathrm{S}$), would help to obtain a better estimate of this crossover location. However, the effects described in Chapter 2 for the same particles as were used in the present work demonstrate that the parameter space for observing the colloidal Brazil-nut effect may be limited if charge regulation is important, as is almost always the case in low-polar solvents. It was shown in Chapter 2 that if the charge density difference is too large, the charge on the higher-charged particle may induce oppositely charged patches on the other particle species, resulting in

string formation and other phenomena that frustrate the Brazil-nut effect. Adding salt would provide better control of the screening length and make it possible to test the effect of the screening length on the density profiles in a binary system.

6.5 Acknowledgements

I would like to thank Johan Stiefelhagen (RITC-labelled particles) and Gulşen Heessels-Gürboğa (NBD-labelled particles) for synthesising the PMMA particles. Johan Stiefelhagen is also thanked for his help with the locking procedure and useful discussions on PMMA synthesis.

References

[1] W. B. Russel, D. A. Saville and W. R. Schowalter, *Colloidal dispersions*, Cambridge University Press, Cambridge (1992).

[2] R. J. Hunter, *Foundations of colloid science*, Oxford University Press, Oxford, 2nd edn. (2001).

[3] I. W. Hamley, *Introduction to soft matter. Polymers, colloids, amphiphiles and liquid crystals*, John Wiley & Sons Ltd, Chichester (2000).

[4] R. Brown, *A brief account of microscopical observations made in the months of June, July and August, 1827, on the particles contained in the pollen of plants; and on the general existence of active molecules in organic and inorganic bodies*, Phil. Mag. **4**, 161–173 (1828).

[5] A. Einstein, *Über die von der molekularkinetischen Theorie der Wärme geforderte Bewegung von in ruhenden Flüssigkeiten suspendierten Teilchen*, Ann. Phys. **322**, 549–560 (1905).

[6] J. Perrin, *Mouvement brownien et réalité moléculaire*, Ann. Chim. Phys. **18**, 5–114 (1909).

[7] J. Perrin, *Les atomes*, Alcan, Paris (1913).

[8] P. N. Pusey, in *Liquids, freezing and the glass transition*, Editors: J.-P. Hansen, D. Levesque, and J. Zinn-Justin, North-Holland, Amsterdam (1991).

[9] P. N. Pusey and W. van Megen, *Phase behaviour of concentrated suspensions of nearly hard colloidal spheres*, Nature **320**, 340–342 (1986).

[10] Y. Monovoukas and A. P. Gast, *The experimental phase diagram of charged colloidal suspensions*, J. Colloid Interface Sci. **128**, 533–548 (1989).

[11] A. van Blaaderen and P. Wiltzius, *Real-space structure of colloidal hard-sphere glasses*, Science **270**, 1177–1179 (1995).

[12] R. J. Hunter, *Zeta potential in colloid science. Principles and applications*, Academic Press, London (1981).

[13] D. Frenkel and B. Smit, *Understanding molecular simulation: from algorithms to applications*, Academic Press, San Diego, 2nd edn. (2002).

[14] B. Derjaguin and L. Landau, *Theory of the stability of strongly charged lyophobic sols and of the adhesion of strongly charged particles in solution of electrolytes*, Acta Physicochim. URSS **14**, 633–662 (1941).

[15] E. J. W. Verwey and J. Th. G. Overbeek, *Theory of the stability of lyophobic colloids*, Elsevier, Amsterdam (1948).

[16] S. Alexander, P. M. Chaikin, P. Grant, G. J. Morales, P. Pincus and D. Hone, *Charge renormalization, osmotic pressure, and bulk modulus of colloidal crystals: theory*, J. Chem. Phys. **80**, 5776–5781 (1984).

[17] E. Trizac, L. Bocquet, M. Aubouy and H. H. von Grünberg, *Alexander's prescription for colloidal charge renormalization*, Langmuir **19**, 4027–4033 (2003).

[18] M. E. Leunissen, *Manipulating colloids with charges & electric fields*. PhD thesis, Utrecht University, The Netherlands (2007). A digital version of this thesis is available at http://www.colloid.nl.

[19] A. Yethiraj and A. van Blaaderen, *A colloidal model system with an interaction tunable from hard sphere to soft and dipolar*, Nature **421**, 513–517 (2003).

[20] P. N. Pusey, *The effect of polydispersity on the crystallization of hard spherical colloids*, J. Physique **48**, 709–712 (1987).

[21] W. G. Hoover and F. H. Ree, *Melting transition and communal entropy for hard spheres*, J. Chem. Phys. **49**, 3609—3617 (1968).

[22] P. N. Pusey and W. van Megen, *Observation of a glass transition in suspensions of spherical colloidal particles*, Phys. Rev. Lett. **59**, 2083–2086 (1987).

[23] M. O. Robbins, K. Kremer and G. S. Grest, *Phase diagram and dynamics of Yukawa systems*, J. Chem. Phys. **88**, 3286–3312 (1988).

[24] S. Sengupta and A. K. Sood, *Theory of liquid-bcc-fcc coexistence in charge-stabilized colloidal systems*, Phys. Rev. A **44**, 1233–1236 (1991).

[25] S. Hamaguchi, R. T. Farouki and D. H. E. Dubin, *Triple point of Yukawa systems*, Phys. Rev. E **56**, 4671–4682 (1997).

[26] E. J. Meijer and F. El Azhar, *Novel procedure to determine coexistence lines by computer simulation. Application to hard-core Yukawa model for charged-stabilized colloids*, J. Chem. Phys. **106**, 4678–4683 (1997).

[27] F. El Azhar, M. Baus, J.-P. Ryckaert and E. J. Meijer, *Line of triple points for the hard-core Yukawa model: a computer simulation study*, J. Chem. Phys. **112**, 5121–5126 (2000).

[28] A.-P. Hynninen and M. Dijkstra, *Phase diagrams of hard-core repulsive Yukawa particles*, Phys. Rev. E **68**, 021407 (2003).

[29] F. Smallenburg, N. Boon, M. Kater, M. Dijkstra and R. van Roij, *Phase diagrams of colloidal spheres with a constant zeta-potential*, J. Chem. Phys. **134**, 074505 (2011).

[30] E. B. Sirota, H. D. Ou-Yang, S. K. Sinha, P. M. Chaikin, J. D. Axe and Y. Fujii, *Complete phase diagram of a charged colloidal system: a synchrotron X-ray scattering study*, Phys. Rev. Lett. **62**, 1524–1527 (1989).

[31] M. E. Leunissen, C. G. Christova, A.-P. Hynninen, C. P. Royall, A. I. Campbell, A. Imhof, M. Dijkstra, R. van Roij and A. van Blaaderen, *Ionic colloidal crystals of oppositely charged particles*, Nature **437**, 235–240 (2005).

[32] P. Bartlett and A. I. Campbell, *Three-dimensional binary superlattices of oppositely charged colloids*, Phys. Rev. Lett. **95**, 128302 (2005).

[33] A. Esztermann and H. Löwen, *Colloidal Brazil-nut effect in sediments of binary charged suspensions*, Europhys. Lett. **68**, 120–126 (2004).

[34] P. J. Steinhardt, D. R. Nelson and M. Ronchetti, *Bond-orientational order in liquids and glasses*, Phys. Rev. B **28**, 784–805 (1983).

[35] W. Lechner and C. Dellago, *Accurate determination of crystal structures based on averaged local bond order parameters*, J. Chem. Phys. **129**, 114707 (2008).

[36] P. R. ten Wolde, M. J. Ruiz-Montero and D. Frenkel, *Numerical evidence for bcc ordering at the surface of a critical fcc nucleus*, Phys. Rev. Lett. **75**, 2714–2717 (1995).

[37] Ph. C. van der Hoeven and J. Lyklema, *Electrostatic stabilization in non-aqueous media*, Adv. Colloid Interface Sci. **42**, 205–277 (1992).

[38] I. D. Morrison, *Electrical charges in nonaqueous media*, Colloids Surf. A **71**, 1–37 (1993).

[39] C. P. Royall, M. E. Leunissen and A. van Blaaderen, *A new colloidal model system to study long-range interactions quantitatively in real space*, J. Phys.: Condens. Matter **15**, S3581–S3596 (2003).

[40] M. E. Leunissen, A. van Blaaderen, A. D. Hollingsworth, M. T. Sullivan and P. M. Chaikin, *Electrostatics at the oil-water interface, stability, and order in emulsions and colloids*, Proc. Natl. Acad. Sci. **104**, 2585–2590 (2007).

[41] B. P. Binks, *Particles as surfactants – similarities and differences*, Curr. Opin. Colloid Interface Sci. **7**, 21–41 (2002).

[42] B. Comiskey, J. D. Albert, H. Yoshizawa and J. Jacobson, *An electrophoretic ink for all-printed reflective electronic displays*, Nature **394**, 253–255 (1998).

[43] P. Jenkins, S. Basu, R. I. Keir, J. Ralston, J. C. Thomas and B. M. A. Wolffenbuttel, *The electrochemistry of nonaqueous copper phthalocyanine dispersions in the presence of a metal soap surfactant: a simple equilibrium site binding model*, J. Colloid Interface Sci. **211**, 252–263 (1999).

[44] T. Hao, *Electrorheological fluids*, Adv. Mater. **13**, 1847–1857 (2001).

[45] G. S. Roberts, R. Sanchez, R. Kemp, T. Wood and P. Bartlett, *Electrostatic charging of nonpolar colloids by reverse micelles*, Langmuir **24**, 6530–6541 (2008).

[46] T. Vissers, A. Imhof, F. Carrique, A. V. Delgado and A. van Blaaderen, *Electrophoresis of concentrated colloidal suspensions in low-polar solvents*, J. Colloid Interface Sci. **361**, 443–455 (2011).

[47] P. G. Smith, Jr., M. N. Patel, J. Kim, T. E. Milner and K. P. Johnston, *Effect of surface hydrophilicity on charging mechanism of colloids in low-permittivity solvents*, J. Phys. Chem. C **111**, 840–848 (2007).

[48] S. K. Sainis, V. Germain, C. O. Mejean and E. R. Dufresne, *Electrostatic interactions of colloidal particles in nonpolar solvents: role of surface chemistry and charge control agents*, Langmuir **24**, 1160–1164 (2008).

[49] M. F. Hsu, E. R. Dufresne and D. A. Weitz, *Charge stabilization in nonpolar solvents*, Langmuir **21**, 4881–4887 (2005).

[50] A. Kitahara, T. Satoh, S. Kawasaki and K. Kon-No, *Specific adsorption of surfactants containing Mn or Co on polymer particles revealed by zeta-potential in cyclohexane*, J. Colloid Interface Sci. **86**, 105–110 (1982).

[51] R. I. Keir, Suparno and J. C. Thomas, *Charging behavior in the silica/aerosol OT/decane system*, Langmuir **18**, 1463–1465 (2002).

[52] F. Beunis, F. Strubbe, K. Neyts and D. Petrov, *Beyond Millikan: the dynamics of charging events on individual colloidal particles*, Phys. Rev. Lett. **108**, 016101 (2012).

[53] F. Strubbe, F. Beunis, M. Marescaux and K. Neyts, *Charging mechanism in colloidal particles leading to a linear relation between charge and size*, Phys. Rev. E **75**, 031405 (2007).

[54] F. Strubbe, F. Beunis, M. Marescaux, B. Verboven and K. Neyts, *Electrokinetics of colloidal particles in nonpolar media containing charged inverse micelles*, Appl. Phys. Lett. **93**, 254106 (2008).

[55] R. Sánchez and P. Bartlett, *Synthesis of charged particles in an ultra-low dielectric solvent*, Soft Matter **7**, 887–890 (2011).

[56] R. Kemp, R. Sanchez, K. J. Mutch and P. Bartlett, *Nanoparticle charge control in nonpolar liquids: insights from small-angle neutron scattering and microelectrophoresis*, Langmuir **26**, 6967–6976 (2010).

[57] G. S. Roberts, T. A. Woods, W. J. Frith and P. Bartlett, *Direct measurement of the effective charge in nonpolar suspensions by optical tracking of single particles*, J. Chem. Phys. **126**, 194503 (2007).

[58] Q. Guo, V. Singh and S. H. Behrens, *Electric charging in nonpolar liquids because of nonionizable surfactants*, Langmuir **26**, 3203–3207 (2010).

[59] Q. Guo, J. Lee, V. Singh and S. H. Behrens, *Surfactant mediated charging of polymer particles in a nonpolar liquid*, J. Colloid Interface Sci. **392**, 83–89 (2013).

[60] S. Poovarodom and J. C. Berg, *Effect of particle and surfactant acid-base properties on charging of colloids in apolar media*, J. Colloid Interface Sci. **346**, 370–377 (2010).

[61] M. Gacek, G. Brooks and J. C. Berg, *Characterization of mineral oxide charging in apolar media*, Langmuir **28**, 3032–3036 (2012).

[62] A. S. Dukhin and P. J. Goetz, *How non-ionic "electrically neutral" surfactants enhance electrical conductivity and ion stability in non-polar liquids*, J. Electroanal. Chem. **588**, 44–50 (2006).

[63] M. Gacek, D. Bergsman, E. Michor and J. C. Berg, *Effects of trace water on charging of silica particles dispersed in a nonpolar medium*, Langmuir **28**, 11633–11638 (2012).

[64] A. Dukhin and P. Goetz, *Evolution of water-in-oil emulsion controlled by droplet-bulk ion exchange: acoustic, electroacoustic, conductivity and image analysis*, Colloids Surf. A **253**, 51–64 (2005).

[65] C. E. Espinosa, Q. Guo, V. Singh and S. H. Behrens, *Particle charging and charge screening in nonpolar dispersions with nonionic surfactants*, Langmuir **26**, 16941–16948 (2010).

[66] G. N. Smith and J. Eastoe, *Controlling colloid charge in nonpolar liquids with surfactants*, Phys. Chem. Chem. Phys. **15**, 424–439 (2013).

[67] R. M. Fuoss, *Ionic association. III. The equilibrium between ion pairs and free ions*, J. Am. Chem. Soc. **80**, 5059–5061 (1958).

[68] J. N. Israelachvili, *Intermolecular and surface forces*, Academic Press, Burlington, 3rd edn. (2011).

[69] W. M. Heston, Jr., E. J. Hennelly and C. P. Smyth, *Dielectric constants, viscosities, densities, refractive indices and dipole moment calculations for some organic halides*, J. Am. Chem. Soc. **72**, 2071–2075 (1950).

[70] R. M. Fuoss, *Dependence of the Walden product on dielectric constant*, Proc. Natl. Acad. Sci. **45**, 807–813 (1959).

[71] J. F. Miller, K. Schätzel and B. Vincent, *The determination of very small electrophoretic mobilities in polar and nonpolar colloidal dispersions using phase analysis light scattering*, J. Colloid Interface Sci. **143**, 532–554 (1991).

[72] F. Strubbe, F. Beunis and K. Neyts, *Detection of elementary charges on colloidal particles*, Phys. Rev. Lett. **100**, 218301 (2008).

[73] M. Medebach and T. Palberg, *Phenomenology of colloidal crystal electrophoresis*, J. Chem. Phys. **119**, 3360–3370 (2003).

[74] M. Medebach, L. Shapran and T. Palberg, *Electrophoretic flow behaviour and mobility of colloidal fluids and crystals*, Colloids Surf. B **56**, 210–219 (2007).

[75] V. Lobaskin, B. Dünweg, M. Medebach, T. Palberg and C. Holm, *Electrophoresis of colloidal dispersions in the low-salt regime*, Phys. Rev. Lett. **98**, 176105 (2007).

[76] S. Poovarodom, S. Poovarodom and J. C. Berg, *Effect of alkyl functionalization on charging of colloidal silica in apolar media*, J. Colloid Interface Sci. **351**, 415–420 (2010).

[77] M. E. Leunissen, J. Zwanikken, R. van Roij, P. M. Chaikin and A. van Blaaderen, *Ion partitioning at the oil-water interface as a source of tunable electrostatic effects in emulsions with colloids*, Phys. Chem. Chem. Phys. **9**, 6405–6414 (2007).

[78] P. Wette, H. J. Schöpe and T. Palberg, *Comparison of colloidal effective charges from different experiments*, J. Chem. Phys. **116**, 10981–10988 (2002).

[79] M. J. Stevens, M. L. Falk and M. O. Robbins, *Interactions between charged spherical macroions*, J. Chem. Phys. **104**, 5209–5219 (1996).

[80] E. Trizac and Y. Levin, *Renormalized jellium model for charge-stabilized colloidal suspensions*, Phys. Rev. E **69**, 031403 (2004).

[81] T. Gisler, S. F. Schulz, M. Borkovec, H. Sticher, P. Schurtenberger, B. D'Aguanno and R. Klein, *Understanding colloidal charge renormalization from surface chemistry: experiment and theory*, J. Chem. Phys. **101**, 9924–9936 (1994).

[82] H. H. von Grünberg, *Chemical charge regulation and charge renormalization in concentration colloidal suspensions*, J. Colloid Interface Sci. **219**, 339–344 (1999).

[83] G. Bosma, C. Pathmamanoharan, E. H. A. de Hoog, W. K. Kegel, A. van Blaaderen and H. N. W. Lekkerkerker, *Preparation of monodisperse, fluorescent PMMA-latex colloids by dispersion polymerization*, J. Colloid Interface Sci. **245**, 292–300 (2002).

[84] M. T. Elsesser and A. D. Hollingsworth, *Revisiting the synthesis of a well-known comb-graft copolymer stabilizer and its application to the dispersion polymerization of poly(methyl methacrylate) in organic media*, Langmuir **26**, 17989–17996 (2010).

[85] L. Antl, J. W. Goodwin, R. D. Hill, R. H. Ottewill, S. M. Owens, S. Papworth and J. A. Waters, *The preparation of poly(methyl methacrylate) latices in non-aqueous media*, Colloids and Surfaces **17**, 67–78 (1986).

[86] C. P. Royall, M. E. Leunissen, A.-P. Hynninen, M. Dijkstra and A. van Blaaderen, *Re-entrant melting and freezing in a model system of charged colloids*, J. Chem. Phys. **124**, 244706 (2006).

[87] T. Vissers, *Oppositely charged colloids out of equilibrium*. PhD thesis, Utrecht University, The Netherlands (2010). A digital version of this thesis is available at http://www.colloid.nl.

[88] J. C. Crocker and D. G. Grier, *Methods of digital video microscopy for colloidal studies*, J. Colloid Interface Sci. **179**, 298–310 (1996).

[89] F. Carrique, F. J. Arroyo and A. V. Delgado, *Electrokinetics of concentrated suspensions of spherical colloidal particles with surface conductance, arbitrary zeta potential, and double-layer thickness in static electric fields*, J. Colloid Interface Sci. **252**, 126–137 (2002).

[90] G. J. Janz and S. S. Danyluk, *Conductances of hydrogen halides in anhydrous polar organic solvents*, Chem. Rev. **60**, 209–234 (1960).

[91] R. J. Sengwa, V. Khatri and S. Sankhla, *Dielectric properties and hydrogen bonding interaction behaviour in binary mixtures of glycerol with amides and amines*, Fluid Phase Equilibria **266**, 54–58 (2008).

[92] C. P. Royall, R. van Roij and A. van Blaaderen, *Extended sedimentation profiles in charged colloids: the gravitational length, entropy, and electrostatics*, J. Phys.: Condens. Matter **17**, 2315–2326 (2005).

[93] B. Zoetekouw, *Phase behaviour of charged colloids. Many-body effects, charge renormalization, and charge regulation*. PhD thesis, Utrecht University, The Netherlands (2006). A digital version of this thesis is available at http://web.science.uu.nl/ITF/cmtscp/theses.htm.

[94] N. Boon, *Electrostatics in ionic solution. Work and energy, charge regulation, and inhomogeneous surfaces*. PhD thesis, Utrecht University, The Netherlands (2012). A digital version of this thesis is available at http://web.science.uu.nl/ITF/cmtscp/theses.htm.

[95] Available at http://www.colloid.nl.

[96] P. Wette, I. Klassen, D. Holland-Moritz, D. M. Herlach, H. J. Schöpe, N. Lorenz, H. Reiber, T. Palberg and S. V. Roth, *Communications: complete description of re-entrant phase behavior in a charge variable colloidal model system*, J. Chem. Phys. **132**, 131102 (2010).

[97] P. Sollich, *Predicting phase equilibria in polydisperse systems*, J. Phys.: Condens. Matter **14**, R79–R117 (2002).

[98] R. McRae and A. D. J. Haymet, *Freezing of polydisperse hard spheres*, J. Chem. Phys. **88**, 1114–1125 (1988).

[99] S.-E. Phan, W. B. Russel, J. Zhu and P. M. Chaikin, *Effects of polydispersity on hard sphere crystals*, J. Chem. Phys. **108**, 9789–9795 (1998).

[100] P. Bartlett and P. B. Warren, *Reentrant melting in polydispersed hard spheres*, Phys. Rev. Lett. **82**, 1979–1982 (1999).

[101] D. A. Kofke and P. G. Bolhuis, *Freezing of polydisperse hard spheres*, Phys. Rev. E **59**, 618–622 (1999).

[102] M. Fasolo and P. Sollich, *Fractionation effects in phase equilibria of polydisperse hard-sphere colloids*, Phys. Rev. E **70**, 041410 (2004).

[103] P. Chaudhuri, S. Karmakar, C. Dasgupta, H. R. Krishnamurthy and A. K. Sood, *Equilibrium glassy phase in a polydisperse hard-sphere system*, Phys. Rev. Lett. **95**, 248301 (2005).

[104] E. Zaccarelli, C. Valeriani, E. Sanz, W. C. K. Poon, M. E. Cates and P. N. Pusey, *Crystallization of hard-sphere glasses*, Phys. Rev. Lett. **103**, 135704 (2009).

[105] P. Sollich and N. B. Wilding, *Crystalline phases of polydisperse spheres*, Phys. Rev. Lett. **104**, 118302 (2010).

[106] N. B. Wilding and P. Sollich, *Phase behavior of polydisperse spheres: simulation strategies and an application to the freezing transition*, J. Chem. Phys. **133**, 224102 (2010).

[107] P. Sollich and N. B. Wilding, *Polydispersity induced solid-solid transitions in model colloids*, Soft Matter **7**, 4472–4484 (2011).

[108] E. Dickinson and R. Parker, *Polydispersity and the fluid-crystalline phase transition*, J. Physique Lett. **46**, L229–L232 (1985).

[109] R. S. Farr and R. D. Groot, *Close packing density of polydisperse hard spheres*, J. Chem. Phys. **131**, 244104 (2009).

[110] R. P. A. Dullens and W. K. Kegel, *Reentrant surface melting of colloidal hard spheres*, Phys. Rev. Lett. **92**, 195702 (2004).

[111] P. Yunker, Z. Zhang and A. G. Yodh, *Observation of the disorder-induced crystal-to-glass transition*, Phys. Rev. Lett. **104**, 015701 (2010).

[112] B. V. R. Tata and A. K. Arora, *Crystalline-to-glass transition in charge polydisperse colloids*, J. Phys.: Condens. Matter **4**, 7699–7708 (1992).

[113] M. Yiannourakou, I. G. Economou and I. A. Bitsanis, *Phase equilibrium of colloidal suspensions with particle size dispersity: a Monte Carlo study*, J. Chem. Phys. **130**, 194902 (2009).

[114] J. Colombo and M. Dijkstra, *Effect of quenched size polydispersity on the fluid-solid transition in charged colloidal suspensions*, J. Chem. Phys. **134**, 154504 (2011).

[115] S. Auer and D. Frenkel, *Suppression of crystal nucleation in polydisperse colloids due to increase of the surface free energy*, Nature **413**, 711–713 (2001).

[116] L. A. Fernández, V. Martín-Mayor and P. Verrocchio, *Phase diagram of a polydisperse soft-spheres model for liquids and colloids*, Phys. Rev. Lett. **98**, 085702 (2007).

[117] M. E. Leunissen and A. van Blaaderen, *Concentrating colloids with electric field gradients. II. Phase transitions and crystal buckling of long-ranged repulsive charged spheres in an electric bottle*, J. Chem. Phys. **128**, 164509 (2008).

[118] M. Raşa and A. P. Philipse, *Evidence for a macroscopic electric field in the sedimentation profiles of charged colloids*, Nature **429**, 857–860 (2004).

[119] P. M. Biesheuvel, *Evidence for charge regulation in the sedimentation of charged colloids*, J. Phys.: Condens. Matter **16**, L499–L504 (2004).

[120] J. W. Merrill, S. K. Sainis and E. R. Dufresne, *Many-body electrostatic forces between colloidal particles at vanishing ionic strength*, Phys. Rev. Lett. **103**, 138301 (2009).

[121] D. El Masri, P. van Oostrum, F. Smallenburg, T. Vissers, A. Imhof, M. Dijkstra and A. van Blaaderen, *Measuring colloidal forces from particle position deviations inside an optical trap*, Soft Matter **7**, 3462–3466 (2011).

[122] L. Berthier and W. Kob, *The Monte Carlo dynamics of a binary Lennard-Jones glass-forming mixture*, J. Phys.: Condens. Matter **19**, 205130 (2007).

[123] E. Sanz and D. Marenduzzo, *Dynamic Monte Carlo versus Brownian dynamics: a comparison for self-diffusion and crystallization in colloidal fluids*, J. Chem. Phys. **132**, 194102 (2010).

[124] S. Jabbari-Farouji and E. Trizac, *Dynamic Monte Carlo simulations of anisotropic colloids*, J. Chem. Phys. **137**, 054107 (2012).

[125] M. Buzzacchi, P. Sollich, N. B. Wilding and M. Müller, *Simulation estimates of cloud points of polydisperse fluids*, Phys. Rev. E **73**, 046110 (2006).

[126] R. M. L. Evans, D. J. Fairhurst and W. C. K. Poon, *Universal law of fractionation for slightly polydisperse systems*, Phys. Rev. Lett. **81**, 1326–1329 (1998).

[127] W. van Megen and S. M. Underwood, *Glass transition in colloidal hard spheres: measurement and mode-coupling-theory analysis of the coherent intermediate scattering function*, Phys. Rev. E **49**, 4206–4220 (1994).

[128] G. Brambilla, D. El Masri, M. Pierno, L. Berthier, L. Cipelletti, G. Petekidis and A. B. Schofield, *Probing the equilibrium dynamics of colloidal hard spheres above the mode-coupling glass transition*, Phys. Rev. Lett. **102**, 085703 (2009).

[129] J. Mattsson, H. M. Wyss, A. Fernandez-Nieves, K. Miyazaki, Z. Hu, D. R. Reichman and D. A. Weitz, *Soft colloids make strong glasses*, Nature **462**, 83–86 (2009).

[130] W. Härtl, H. Versmold and X. Zhang-Heider, *The glass transition of charged polymer colloids*, J. Chem. Phys. **102**, 6613–6618 (1995).

[131] Ch. Beck, W. Härtl and R. Hempelmann, *The glass transition of charged and hard sphere silica colloids*, J. Chem. Phys. **111**, 8209–8213 (1999).

[132] E. Bartsch, V. Frenz and H. Sillescu, *The glass transition of colloidal polystyrene micronetwork spheres – a dynamic light scattering study*, J. Non-Cryst. Solids **172–174**, 88–97 (1994).

[133] E. Bartsch, V. Frenz, J. Baschnagel, W. Schärtl and H. Sillescu, *The glass transition dynamics of polymer network colloids. A mode coupling analysis*, J. Chem. Phys. **106**, 3743–3756 (1997).

[134] E. Bartsch, M. Antonietti, W. Schupp and H. Sillescu, *Dynamic light scattering study of concentrated microgel solutions as mesoscopic model of the glass transition in quasiatomic fluids*, J. Chem. Phys. **97**, 3950–3963 (1992).

[135] G. Szamel and E. Flenner, *Independence of the relaxation of a supercooled fluid from its microscopic dynamics: need for yet another extension of the mode-coupling theory*, Europhys. Lett. **67**, 779–785 (2004).

[136] C. A. Angell, K. L. Ngai, G. B. McKenna, P. F. McMillan and S. W. Martin, *Relaxation in glassforming liquids and amorphous solids*, J. Appl. Phys. **88**, 3113–3157 (2000).

[137] R. Casalini, *The fragility of liquids and colloids and its relation to the softness of the potential*, J. Chem. Phys. **137**, 204904 (2012).

[138] W. Götze, *Recent tests of the mode-coupling theory for glassy dynamics*, J. Phys.: Condens. Matter **11**, A1–A45 (1999).

[139] W. Götze and L. Sjögren, *Relaxation processes in supercooled liquids*, Rep. Prog. Phys. **55**, 241–376 (1992).

[140] W. Kob and H. C. Andersen, *Scaling behavior in the β-relaxation regime of a supercooled Lennard-Jones mixture*, Phys. Rev. Lett. **73**, 1376–1379 (1994).

[141] W. van Megen, T. C. Mortensen, S. R. Williams and J. Müller, *Measurement of the self-intermediate scattering function of suspensions of hard spherical particles near the glass transition*, Phys. Rev. E **58**, 6073–6085 (1998).

[142] C. A. Angell, *Relaxation in liquids, polymers and plastic crystals – strong/fragile patterns and problems*, J. Non-Cryst. Solids **131–133**, 13–31 (1991).

[143] W. Götze, *The scaling functions for the β-relaxation process of supercooled liquids and glasses*, J. Phys.: Condens. Matter **2**, 8485–8498 (1990).

[144] A. H. Marcus, J. Schofield and S. A. Rice, *Experimental observations of non-Gaussian behavior and stringlike cooperative dynamics in concentrated quasi-two-dimensional colloidal liquids*, Phys. Rev. E **60**, 5725–5736 (1999).

[145] W. K. Kegel and A. van Blaaderen, *Direct observation of dynamical heterogeneities in colloidal hard-sphere suspensions*, Science **287**, 290–293 (2000).

[146] E. R. Weeks, J. C. Crocker, A. C. Levitt, A. Schofield and D. A. Weitz, *Three-dimensional direct imaging of structural relaxation near the colloidal glass transition*, Science **287**, 627–631 (2000).

[147] F. Sciortino and P. Tartaglia, *Glassy colloidal systems*, Adv. Phys. **54**, 471–524 (2005).

[148] S. Hachisu and K. Takano, *Pressure of disorder to order transition in monodisperse latex*, Adv. Colloid Interface Sci. **16**, 233–252 (1982).

[149] J. S. van Duijneveldt, J. K. G. Dhont and H. N. W. Lekkerkerker, *Expansion and crystallization of a sediment of charged colloidal spheres*, J. Chem. Phys **99**, 6941–6949 (1993).

[150] D. El Masri, T. Vissers, S. Badaire, J. C. P. Stiefelhagen, H. R. Vutukuri, P. Helfferich, T. H. Zhang, W. K. Kegel, A. Imhof and A. van Blaaderen, *A qualitative confocal microscopy study on a range of colloidal processes by simulating microgravity conditions through slow rotations*, Soft Matter **8**, 6979–6990 (2012).

[151] S. K. Sainis, V. Germain, C. O. Mejean and E. R. Dufresne, *Electrostatic interaction of colloidal particles in nonpolar solvents: Role of surface chemistry and charge control agents*, Langmuir **24**, 1160–1164 (2007).

[152] D. Reinke, H. Stark, H.-H. von Grünberg, A. B. Schofield, G. Maret and U. Gasser, *Noncentral forces in crystals of charged colloids*, Phys. Rev. Lett. **98**, 038301 (2007).

[153] R. van Roij and J.-P. Hansen, *Van der Waals-like instability in suspensions of mutually repelling charged colloids*, Phys. Rev. Lett. **79**, 3082–3085 (1997).

[154] R. van Roij, M. Dijkstra and J.-P. Hansen, *Phase diagram of charge-stabilized colloidal suspensions: van der Waals instability without attractive forces*, Phys. Rev. E **59**, 2010–2025 (1999).

[155] U. Dassanayake, S. Fraden and A. van Blaaderen, *Structure of electrorheological fluids*, J. Chem. Phys. **112**, 3851–3858 (2000).

[156] L. D. Landau and E. M. Lifshitz, *Quantum mechanics*, Pergamon, New York (1965). Translated from Russian by J. B. Sykes and J. S. Bell.

[157] J. L. Finney, *Random packings and the structure of simple liquids I. The geometry of random close packing*, Proc. Roy. Soc. Lond. A **319**, 479–493 (1970).

[158] C. H. Bennett, *Serially deposited amorphous aggregates of hard spheres*, J. Appl. Phys. **43**, 2727–2734 (1972).

[159] J. Jäckle, *Models of the glass transition*, Rep. Prog. Phys. **49**, 171–231 (1986).

[160] S. P. Pan, J. Y. Qin, W. M. Wang and T. K. Gu, *Origin of splitting of the second peak in the pair-distribution function for metallic glasses*, Phys. Rev. B **84**, 092201 (2011).

[161] D. E. Polk, *Dense random packing of hard spheres of two different sizes*, J. Non-Cryst. Solids **11**, 381–394 (1973).

[162] S. Auer and D. Frenkel, *Crystallization of weakly charged colloidal spheres: a numerical study*, J. Phys.: Condens. Matter **14**, 7667–7680 (2002).

[163] N. A. M. Verhaegh, J. S. van Duijneveldt, A. van Blaaderen and H. N. W. Lekkerkerker, *Direct observation of stacking disorder in a colloidal crystal*, J. Chem. Phys. **102**, 1416–1421 (1995).

[164] J. P. Hoogenboom, D. Derks, P. Vergeer and A. van Blaaderen, *Stacking faults in colloidal crystals grown by sedimentation*, J. Chem. Phys. **117**, 11320–11328 (2002).

[165] A.-P. Hynninen and M. Dijkstra, *Phase diagram of dipolar hard and soft spheres: manipulation of colloidal crystal structures by an external field*, Phys. Rev. Lett. **94**, 138303 (2005).

[166] M. E. Leunissen, H. R. Vutukuri and A. van Blaaderen, *Directing colloidal self-assembly with biaxial electric fields*, Adv. Mater. **21**, 3116–3120 (2009).

[167] R. M. Erb, H. S. Son, B. Samanta, V. M. Rotello and B. B. Yellen, *Magnetic assembly of colloidal superstructures with multipole symmetry*, Nature **457**, 999–1002 (2009).

[168] J. C. Williams, *The segregation of particulate materials*, Powder Technol. **15**, 245–251 (1976).

[169] A. Rosato, K. J. Strandburg, F. Prinz and R. H. Swendsen, *Why the Brazil nuts are on top: size segregation of particulate matter by shaking*, Phys. Rev. Lett. **58**, 1038–1040 (1987).

[170] J. Zwanikken and R. van Roij, *The sediment of mixtures of charged colloids: segregation and inhomogeneous electric fields*, Europhys. Lett. **71**, 480–486 (2005).

[171] P. M. Biesheuvel and J. Lyklema, *Sedimentation-diffusion equilibrium of binary mixtures of charged colloids including volume effects*, J. Phys.: Condens. Matter **17**, 6337–6352 (2005).

[172] M. Dijkstra, J. Zwanikken and R. van Roij, *Sedimentation of binary mixtures of like- and oppositely charged colloids: the primitive model or effective pair potentials?*, J. Phys.: Condens. Matter **18**, 825–836 (2006).

[173] A. Cuetos, A.-P. Hynninen, J. Zwanikken, R. van Roij and M. Dijkstra, *Layering in sedimentation of suspensions of charged colloids: simulation and theory*, Phys. Rev. E **73**, 061402 (2006).

[174] R. van Roij, *Defying gravity with entropy and electrostatics: sedimentation of charged colloids*, J. Phys.: Condens. Matter **15**, S3569–S3580 (2003).

[175] T. Biben and J.-P. Hansen, *Sedimentation equilibrium in concentrated charge-stabilized colloidal suspensions*, J. Phys.: Condens. Matter **6**, A345–A349 (1994).

[176] A.-P. Hynninen, R. van Roij and M. Dijkstra, *Sedimentation profiles of charged colloids: entropic lift and charge separation*, Europhys. Lett. **65**, 719–725 (2004).

[177] A. Torres, A. Cuetos, M. Dijkstra and R. van Roij, *Sedimentation of charged colloids: the primitive model and the effective one-component approach*, Phys. Rev. E **75**, 041405 (2007).

[178] L. Belloni, *Yes, pair correlations alone do determine sedimentation profiles of highly charged colloids*, J. Chem. Phys. **123**, 204705 (2005).

[179] M. Raşa, B. H. Erné, B. Zoetekouw, R. van Roij and A. P. Philipse, *Macroscopic electric field and osmotic pressure in ultracentrifugal sedimentation-diffusion equilibria of charged colloids*, J. Phys.: Condens. Matter **17**, 2293–2314 (2005).

[180] E. Allahyarov and H. Löwen, *Nonadditivity in the effective interactions of binary charged colloidal suspensions*, J. Phys.: Condens. Matter **21**, 424117 (2009).

[181] T. Kruppa, T. Neuhaus, R. Messina and H. Löwen, *Soft repulsive mixtures under gravity: Brazil-nut effect, depletion bubbles, boundary layering, nonequilibrium shaking*, J. Chem. Phys. **136**, 134106 (2012).

[182] C. González Serrano, J. J. McDermott and D. Velegol, *Sediments of soft spheres arranged by effective density*, Nature Mater. **10**, 716–721 (2011).

[183] C. P. Royall, J. Dzubiella, M. Schmidt and A. van Blaaderen, *Nonequilibrium sedimentation of colloids on the particle scale*, Phys. Rev. Lett. **98**, 188304 (2007).

[184] E. C. M. Vermolen, *Manipulation of colloidal crystallization*. PhD thesis, Utrecht University, The Netherlands (2008). A digital version of this thesis is available at http://www.colloid.nl.

[185] K. Milinković, J. T. Padding and M. Dijkstra, *Hydrodynamic Rayleigh-Taylor-like instabilities in sedimenting colloidal mixtures*, Soft Matter **7**, 11177–11186 (2011).

Summary

The research described in this thesis focusses on the behaviour of charged colloidal spheres, specifically those with long-range repulsive interactions. The experimental model system we used in Chapters 2, 5 and 6 consisted of sterically stabilised poly(methyl methacrylate) (PMMA) colloids suspended in the low-polar solvent cyclohexyl bromide (CHB). Decomposition of CHB in time generates ions (H^+ and Br^-), which adsorb onto the surface of the particles. Preferential adsorption of H^+ ions gives the particles a net positive charge. The low polarity of the solvent ($\epsilon_r = 7.92$) makes that much lower ionic concentrations can be achieved than for instance in water, resulting in a large Debye screening length (on the order of the particle diameter), which indicates a thick electrical double layer and long-range interactions. The pair interaction in these systems is often described by a hard-core repulsive Yukawa (screened Coulomb) potential. We used this pair potential for the computer simulations in Chapters 3 and 4.

In Chapter 2 we performed microelectrophoresis measurements to determine the surface potential and charge of the PMMA particles in CHB at a volume fraction η of around 0.02. We prepared suspensions of so-called 'locked' and 'unlocked' particles of various diameters. For unlocked particles the steric stabiliser is adsorbed to the surface of the particles, while for locked particles the stabiliser is covalently bonded to the surface. We used confocal microscopy to measure the velocity profiles of the particles as they moved in an electric field, from which the electrophoretic mobility was determined for the different particle species. In our systems the double layers are on the order of the interparticle distance at $\eta \approx 0.02$, which has important consequences for data analysis. To convert the particle mobility to a surface potential and charge we solved the full Poisson-Boltzmann equation in a Kuwabara cell model, which allowed for double-layer overlap. For the locked particles we found that the surface potential was roughly constant for all particle diameters we investigated (1.9 µm $< \sigma <$ 4.4 µm), and that the particle charge was proportional to the square of the diameter. Unlocked particles had a significantly lower surface potential and charge than locked particles. We also performed measurements on mixtures of two particle species of different diameter and charge. Intriguingly, we observed the spontaneous formation of alternating strings, i.e. strings in which the two charged species occurred in an alternating fashion. Electrophoresis measurements showed, however, that the two charged species both carried a positive charge. At this moment, the exact mechanism of the string formation is therefore not yet established.

In Chapter 3 we used Monte Carlo simulations to investigate the effect of size polydispersity on the crystal-fluid transition in systems interacting through a hard-core repulsive Yukawa potential. Size polydispersity was introduced in the system with respect to the hard cores of the particles. Particles with different diameters had the same surface potential, but the charge per particle was not varied with volume fraction or distance. We observed a shift of the crystal-fluid transition of bulk crystals with a fixed log-normal size distribution to higher volume fraction upon increasing the polydispersity. The shift was more pronounced for lower-charged particles ($\beta e\psi_0 \approx 1$, with $\lambda_B/\bar{\sigma} = 0.01$) than for higher-charged particles ($\beta e\psi_0 \approx 2$), and also more pronounced for larger Debye screening lengths. At high polydispersities (≥ 0.13) parts of the higher-charged systems that were initially crystalline became amorphous. The amorphous parts had a higher polydispersity than the crystalline parts, indicating the presence of a terminal polydispersity beyond which the homogeneous crystal phase was no longer stable. The dynamics in the partly crystalline systems was very slow or glassy, i.e. particles moved over a typical distance smaller than their diameter during the length of the simulation.

In Chapter 4 we followed up the previous Monte Carlo simulations and investigated the slow dynamics close to the glass transition in hard-core repulsive Yukawa systems. We studied systems with a contact value of the Yukawa potential $\beta\bar{\epsilon} = 81$, corresponding to a dimensionless surface potential $\beta e\psi_0 \approx 2$, and three different inverse screening lengths $\kappa\bar{\sigma} = 2.5$, 3.3 and 10. To address structural relaxation in the systems we calculated self-intermediate scattering functions (SISFs) for three different values of the wave number q, one of which was close to the first peak of the structure factor. The long-time structural relaxation times τ_α were obtained from stretched exponential fits to the SISFs. In addition, to measure particle diffusion, we calculated mean square displacements (MSDs). From the MSD we determined the long-time self-diffusion coefficient D_L. The obtained values for τ_α at different q, and D_L^{-1}, could be well fitted both by a power law ($\tau_\alpha \propto D_L^{-1} \propto (\eta_c - \eta)^{-\gamma}$), predicted by mode-coupling theory (MCT), and by the Vogel-Fulcher-Tammann (VFT) equation ($\tau_\alpha \propto D_L^{-1} \propto \exp[B\eta/(\eta_0 - \eta)]$). The power-law fit from MCT yielded a glass transition volume fraction η_c that was much lower than the glass transition volume fraction η_0 from the VFT fit. The power-law exponent γ and VFT fit parameter B were larger for longer-range potentials. Furthermore, we found that the fragility of the glass-forming system decreased with increasing range of the potential (larger screening length κ^{-1}), suggesting that the fragility of experimental colloidal systems can be tuned by changing the salt concentration.

In Chapter 5 we studied long-range repulsive glasses formed in suspensions of charged PMMA particles in CHB. Initially, the suspensions had a volume fraction $\eta \approx 0.02$ and a body-centred-cubic-crystalline structure. Glasses were obtained

upon compression of the suspensions by centrifugation to a close-packed amorphous structure ($\eta \approx 0.64$). Subsequent expansion of the sediment in gravity resulted in long-range repulsive glassy structures with volume fractions $\eta = 0.16$–0.64. During several weeks, the sediment expanded. Crystallisation of the glasses was prevented by the presence of small clusters (mostly dumbbells; clustered fraction $f_{\mathrm{cl}} \geq 0.12$). The clusters were formed as the particles were pressed together by centrifugation. We used confocal microscopy to obtain three-dimensional data sets of the system and quantitatively analysed the structure of the glasses. The structure of the glasses was found to be remarkably similar to that of hard-sphere glasses, despite the much longer-range interaction potential. After more than ten weeks the clustered fraction decreased due to spontaneous dissociation of the clusters, and finally bulk crystallisation of the glasses was observed into face-centred-cubic crystals with a volume fraction around 0.22.

In Chapter 6 we experimentally studied the equilibrium sedimentation profiles in binary mixtures of charged PMMA colloids in CHB. We used systems with different combinations of charge and mass ratios. In a well-tuned experimental system we observed the colloidal Brazil-nut effect, an ordering of the particles contrary to what would be expected on the basis of their buoyant mass: in equilibrium the larger (heavier) particles stayed further from the surface onto which the particles sedimented than the smaller (lighter) particles. Our findings are in agreement with results from computer simulations and density-functional theory, predicting for long-range repulsive systems the Brazil-nut effect when the mass-per-charge for the heavier colloids is smaller than the mass-per-charge for the lighter colloids.

Samenvatting

Het onderzoek dat beschreven is in dit proefschrift gaat over het gedrag van geladen colloïdale bollen, met name die met repulsieve langedrachtsinteracties. Het experimentele modelsysteem dat we hebben gebruikt in Hoofdstuk 2, 5 en 6 bestond uit sterisch gestabiliseerde poly(methylmethacrylaat) (PMMA) colloïden, gesuspendeerd in het laagpolaire oplosmiddel cyclohexylbromide (CHB). Decompositie van CHB in de tijd genereert ionen (H^+ en Br^-), die op het oppervlak van de deeltjes adsorberen. Preferentiële adsorptie van H^+ ionen geeft de deeltjes een netto positieve lading. De lage polariteit van het oplosmiddel ($\epsilon_r = 7.92$) zorgt ervoor dat veel lagere ionconcentraties kunnen worden bereikt dan bijvoorbeeld in water. Dit resulteert in een grote Debye afschermingslengte (van dezelfde orde van grootte als de deeltjesdiameter), wat overeenkomt met een dikke dubbellaag en een lange dracht van de interactie. De paarinteractie in deze systemen wordt vaak beschreven met een harde-kern repulsieve Yukawa (of afgeschermde Coulomb) potentiaal. We hebben deze paarpotentiaal gebruikt voor de computersimulaties in Hoofdstuk 3 en 4.

In Hoofdstuk 2 hebben we micro-elektroforesemetingen uitgevoerd om de oppervlaktepotentiaal en lading bepalen van de PMMA-deeltjes in CHB bij een volumefractie η van ongeveer 0.02. We hebben suspensies gemaakt van zogenaamde '*locked*' en '*unlocked*' deeltjes van verschillende diameter. Bij *unlocked* deeltjes is de sterische stabilisator geadsorbeerd op het oppervlak van de deeltjes, terwijl bij *locked* deeltjes de stabilisator covalent aan het oppervlak is gebonden. Met behulp van confocale microscopie hebben we de snelheidsprofielen van de deeltjes gemeten, terwijl zij bewogen in een elektrisch veld. Hieruit hebben we de elektroforetische mobiliteit bepaald voor de verschillende soorten deeltjes. De dubbellagen in onze systemen zijn van dezelfde orde van grootte als de afstand tussen de deeltjes bij $\eta \approx 0.02$, wat belangrijke consequenties heeft voor de analyse van de data. Om de mobiliteit om te zetten in een oppervlaktepotentiaal en lading hebben we de volledige Poisson-Boltzmann vergelijking opgelost in een Kuwabara celmodel, waarbij overlap van de dubbellagen is toegestaan. Voor de *locked* deeltjes vonden we dat de oppervlaktepotentiaal grofweg constant was voor alle deeltjesdiameters die we hebben bestudeerd (1.9 µm $< \sigma <$ 4.4 µm) en dat de lading ongeveer evenredig was met het kwadraat van de diameter. *Unlocked* deeltjes hadden een significant lagere oppervlaktepotentiaal en lading dan *locked* deeltjes. We hebben ook metingen uitgevoerd aan mengsels van twee soorten deeltjes met verschillende diameter en lading. In deze mengsels zagen we spontane vorming van ketens, waarin de twee deeltjes elkaar afwisselden (*alternating strings*). Elektroforesemetingen

wezen echter uit dat de twee soorten geladen deeltjes beide een positieve lading hadden. Het precieze mechanisme van de ketenvorming is daarom op dit moment nog niet bekend.

In Hoofdstuk 3 hebben we Monte Carlo simulaties gebruikt om te onderzoeken wat het effect is van polydispersiteit in grootte op de kristal-vloeistof-overgang in systemen die interageren via een harde-kern Yukawa potentiaal. Polydispersiteit in grootte is geïntroduceerd in het systeem met betrekking tot de harde kernen van de deeltjes. Deeltjes met verschillende diameter hadden dezelfde oppervlaktepotentiaal, maar de lading per deeltje werd niet gevarieerd als functie van de volumefractie of afstand. We vonden een verschuiving van de kristal-vloeistof-overgang van bulkkristallen met een vaste lognormale verdeling naar hogere volumefractie met toenemende polydispersiteit. Deze verschuiving was groter voor lagergeladen deeltjes ($\beta e\psi_0 \approx 1$, met $\lambda_B/\bar{\sigma} = 0.01$) dan voor hogergeladen deeltjes ($\beta e\psi_0 \approx 2$), en ook groter voor grotere Debye lengtes. Bij hoge polydispersiteit (≥ 0.13) werden delen van de hogergeladen systemen die aanvankelijk kristallijn waren, amorf. De amorfe stukken hadden een hogere polydispersiteit dan de kristallijne stukken, wat aangeeft dat er een terminale polydispersiteit bestaat waarboven de homogene kristallijne fase niet langer stabiel is. De dynamica in de deels kristallijne systemen was zeer traag of glasachtig, wat betekent dat de deeltjes zich tijdens de duur van de simulatie verplaatsten over een typische afstand kleiner dan de deeltjesdiameter.

In Hoofdstuk 4 hebben we opnieuw Monte Carlo simulaties gebruikt, ditmaal om de trage dynamica dichtbij de glasovergang te onderzoeken in harde-kern repulsieve Yukawa systemen. We hebben systemen bestudeerd met een contactwaarde van de Yukawa potentiaal $\beta\bar{\epsilon} = 81$, welke overeenkomt met een dimensieloze oppervlaktepotentiaal $\beta e\psi_0 \approx 2$, en drie verschillende inverse Debye lengtes $\kappa\bar{\sigma} = 2.5$, 3.3 en 10. Om de structurele relaxatie te bestuderen hebben we *self-intermediate scattering* functies (SISFs) uitgerekend voor drie verschillende waarden van het golfgetal q, waarvan er één dichtbij de eerste piek van de structuurfactor lag. De langetijd structurele relaxatietijd τ_α werd verkregen uit fits van *stretched exponential* functies aan de SISFs. Ook hebben we, om de deeltjesdiffusie te bepalen, gemiddelde kwadratische verplaatsingen (*mean square displacements*, MSDs) uitgerekend. Uit de MSDs hebben we de langetijdzelfdiffusiecoëfficiënt D_L bepaald. De verkregen waarden voor τ_α bij verschillende q, en D_L^{-1}, konden goed worden gefit met een machtsfunctie ($\tau_\alpha \propto D_L^{-1} \propto (\eta_c - \eta)^{-\gamma}$), die voorspeld wordt door *mode-coupling* theorie, en met de Vogel-Fulcher-Tammann (VFT) vergelijking ($\tau_\alpha \propto D_L^{-1} \propto \exp[B\eta/(\eta_0 - \eta)]$). De machtsfunctiefit van MCT resulteerde in een glasovergangsvolumefractie η_c die veel lager was dan de glasovergangsvolumefractie η_0 van de VFT-fit. De exponent γ machtsfunctie en VFT-fitparameter B waren groter voor potentialen met een langere dracht. Verder vonden we dat de *fragility*

van het glasvormende systeem afnam met toenemende dracht van de potentiaal (grotere Debye lengte κ^{-1}), wat suggereert dat de *fragility* van experimentele colloïdale systemen kan worden aangepast door de zoutconcentratie te veranderen.

In Hoofdstuk 5 hebben we glazen van deeltjes met repulsieve langedrachtsinteracties bestudeerd, die waren gevormd in suspensies van geladen PMMA-deeltjes in CHB. Aanvankelijk hadden de suspensies een volumefractie $\eta \approx 0.02$ en een lichaamsgecentreerde kubische kristallijne structuur. Glazen ontstonden door compressie van de suspensies tot een dichtgepakte amorfe structuur ($\eta \approx 0.64$) door middel van centrifugatie. Daaropvolgende expansie van het sediment tegen de zwaartekracht in resulteerde in glasachtige structuren met repulsieve langedrachtsinteracties met volumefracties $\eta = 0.16$–0.64. Het sediment expandeerde gedurende enkele weken. Kristallisatie van de glazen werd voorkomen door aanwezigheid van kleine clusters (voornamelijk duo's in de vorm van een halter; geclusterde fractie $f_{\mathrm{cl}} \geq 0.12$). De clusters werden gevormd toen de deeltjes samengedrukt werden door centrifugatie. We hebben confocale microscopie gebruikt om driedimensionale datasets van het systeem te verkrijgen. Op basis daarvan hebben we de structuur van de glazen kwantitatief geanalyseerd. De structuur van de glazen bleek opmerkelijk vergelijkbaar met die van glazen van harde bollen, ondanks de veel langere dracht van de interactiepotentiaal. De geclusterde fractie nam na meer dan tien weken af door spontane dissociatie van de clusters, waarna uiteindelijk bulkkristallisatie van de glazen optrad tot vlakgecentreerde kubische kristallen met een volumefractie van ongeveer 0.22.

In Hoofdstuk 6 hebben we de evenwichtssedimentatieprofielen in mengsels van geladen PMMA-colloïden in CHB experimenteel bestudeerd. We hebben systemen gebruikt met verschillende combinaties van ladings- en massaverhoudingen. In een goed afgestemd experimenteel systeem hebben we het colloïdale *Brazil-nut* effect waargenomen, een ordening van de deeltjes tegengesteld aan wat verwacht mag worden op grond van hun effectieve massa: in evenwicht bleven de grotere (zwaardere) deeltjes verder van het oppervlak waar de deeltjes naartoe sedimenteerden dan de kleinere (lichtere) deeltjes. Onze bevindingen zijn in overeenstemming met resultaten van computersimulaties en dichtheidsfunctionaaltheorie, die beide het *Brazil-nut* effect voorspellen voor systemen met repulsieve langedrachtsinteracties waarin de massa-per-lading van de zwaardere colloïden kleiner is dan de massa-per-lading van de lichtere colloïden.

Acknowledgements

Now that you've finished reading this booklet, I take it you must be curious to find out which people, indirectly or directly, have made an important contribution to the research described in it.

First of all, I am indebted to my *promotoren* (thesis advisors) Marjolein Dijkstra and Alfons van Blaaderen. Marjolein, I would like to thank you for your kindness and encouragement. I appreciate your refreshing view on and down-to-earth way of solving problems, both scientific and practical. Alfons, your endless sequence of ideas on what to investigate and how to do so and your extensive knowledge of the literature have been very valuable to me. I enjoyed the numerous and often long discussions we had.

Several people I would like to thank for their help in keeping the lab running smoothly. I thank María Delgado Flores, Thea Pozzi, Marjoke Hoenderdos and Marion Wijburg for secretarial support. I am grateful to Carlos van Kats, Gulşen Heessels-Gürboğa, Peter Helfferich and Judith Wijnhoven for technical support.

I would like to thank the many people who contributed to the research by collaboration, useful discussions or in other ways. Johan Stiefelhagen, for patiently answering the many questions I had on PMMA synthesis and various experimental problems, for synthesising several of the PMMA particles I used, for sharing with me the hypothesis that the charge on the particles could be increased by locking them, and for showing me how to do so. Gulşen Heessels-Gürboğa and Judith Wijnhoven, for synthesising many PMMA particles. Jessi van der Hoeven and Nina Elbers, for collaboration to elucidate the mechanism behind the charge increase upon locking and for their enthusiasm in doing research. Djamel El Masri, who performed the E-field experiments that provided more insight in the mechanism of cluster formation, for collaboration and many discussions. Michiel Hermes, for providing his particle tracking code, self-intermediate scattering function code and the opengl colloidal visualisation program, and for useful discussions. Thijs Besseling, for sharing his version of the opengl program. Teun Vissers, for showing me how to perform the microelectrophoresis measurements and for sharing his particle tracking code and the Poisson-Boltzmann cell model code. Peter Helfferich, for his help with optimising the electrophoresis set-up. Arnout Imhof, for his clear explanations and answers to my questions. René van Roij, Niels Boon and Jeffrey Everts from the Institute of Theoretical Physics, for collaboration on the mechanism of cluster and string formation and the Brazil-nut effect, for their interest in experimental work and helpful discussions. René, I also greatly appreciate your enthusiasm and clear explanations. Ahmet Demìrörs, Bing Liu and

Marlous Kamp, for collaboration on various experiments. No doubt, there are several others who deserve my thanks, for useful discussions, long and short, and for their help in the lab or with theoretical, computational or practical problems. Forgive me for not mentioning all of you by name. I would like to thank you all.

It's been a pleasure to have shared my office with Joost de Graaf and Kristina Milinković for almost the entire duration of my PhD. Joost and Kristina, I would like to thank both of you for being helpful, supportive and considerate, it made for a very enjoyable atmosphere. Joost, I think we've all benefitted from your efforts in keeping the office nice-looking and tidy; thank you especially for bringing in many plants and taking care of them. Your knowledge of English vocabulary and pronunciation has also been a great help to me. Kristina, I appreciate your kindness and practical attitude; both have been most welcome and helpful. I very much enjoyed your intelligent and wonderful dry sense of humour.

Finally, I am grateful to my colleagues from the Soft Condensed Matter group, the Institute of Theoretical Physics and further afield, who contributed to an excellent working environment. Due to the friendly atmosphere, the Soft Condensed Matter group is a nice group to be part of. The work discussions with contributions from simulators, experimentalists and theorists have been useful and interesting. Thank you all for sharing your work and for your help solving problems. Thank you for your company during workshops, schools, conferences, group outings, drinks, Sinterklaas-Christmas celebrations and other dinners, for the baking of cookies and cakes, and for sharing innumerable and often ridiculous coffee-table discussions.

Marjolein

List of publications

This thesis is partly based on the following publications:

- M. N. van der Linden, G. Heessels-Gürboğa, M. Dijkstra and A. van Blaaderen, *Countering sedimentation in microelectrophoresis*, in preparation (Chapter 2).
- M. N. van der Linden, A. van Blaaderen and M. Dijkstra, *Effect of size polydispersity on the crystal-fluid and crystal-glass transition in hard-core repulsive Yukawa systems*, J. Chem. Phys. **138**, 114903 (2013) (Chapter 3).
- M. N. van der Linden, A. van Blaaderen and M. Dijkstra, *Can we tune the fragility of long-range colloidal glasses with salt?*, in preparation (Chapter 4).
- M. N. van der Linden, D. El Masri, M. Dijkstra and A. van Blaaderen, *Expansion of charged colloids after centrifugation: formation and crystallisation of long-range repulsive glasses*, in preparation (Chapter 5).
- M. N. van der Linden, M. Dijkstra and A. van Blaaderen, *Experimental observation of the colloidal Brazil-nut effect in binary suspensions of long-range repulsive charged colloids*, in preparation (Chapter 6).

Also by the author:

- M. N. van der Linden, J. P. K. Doye and A. A. Louis, *Formation of dodecagonal quasicrystals in two-dimensional systems of patchy particles*, J. Chem. Phys. **136**, 054904 (2012).

About the author

Marjolein van der Linden was born on 30 January 1985 in Sliedrecht, the Netherlands. She attended secondary school at the Willem de Zwijger College in Papendrecht, from which she obtained her gymnasium diploma in June 2003. During her final secondary-school year she took part in the Dutch National Chemistry Olympiad, in which she placed first. Subsequently, she participated in the International Chemistry Olympiad in Athens, Greece, as one of four members of the Dutch delegation.

She went on to study Molecular Sciences at Wageningen University for one year and continued to study Chemistry at Leiden University, from which she obtained a BSc degree in Chemistry (cum laude). She then moved to Utrecht and graduated from Utrecht University in August 2008 with an MSc in Chemistry (cum laude). As part of her MSc degree she completed a one-year research project in the Soft Condensed Matter group at Utrecht University on the real-space structure of colloidal hard-sphere glasses in experiments and computer simulations and a five-month research project with Dr. Jonathan Doye and Dr. Ard Louis in the Physical and Theoretical Chemistry Laboratory at Oxford University on the formation of dodecagonal quasicrystals in 2D simulations of patchy particles.

In 2008 she received a Toptalent grant from the Netherlands Organisation for Scientific Research (NWO) for a PhD research project in the Soft Condensed Matter group at Utrecht University with Prof. Alfons van Blaaderen and Prof. Marjolein Dijkstra, which resulted in this thesis.